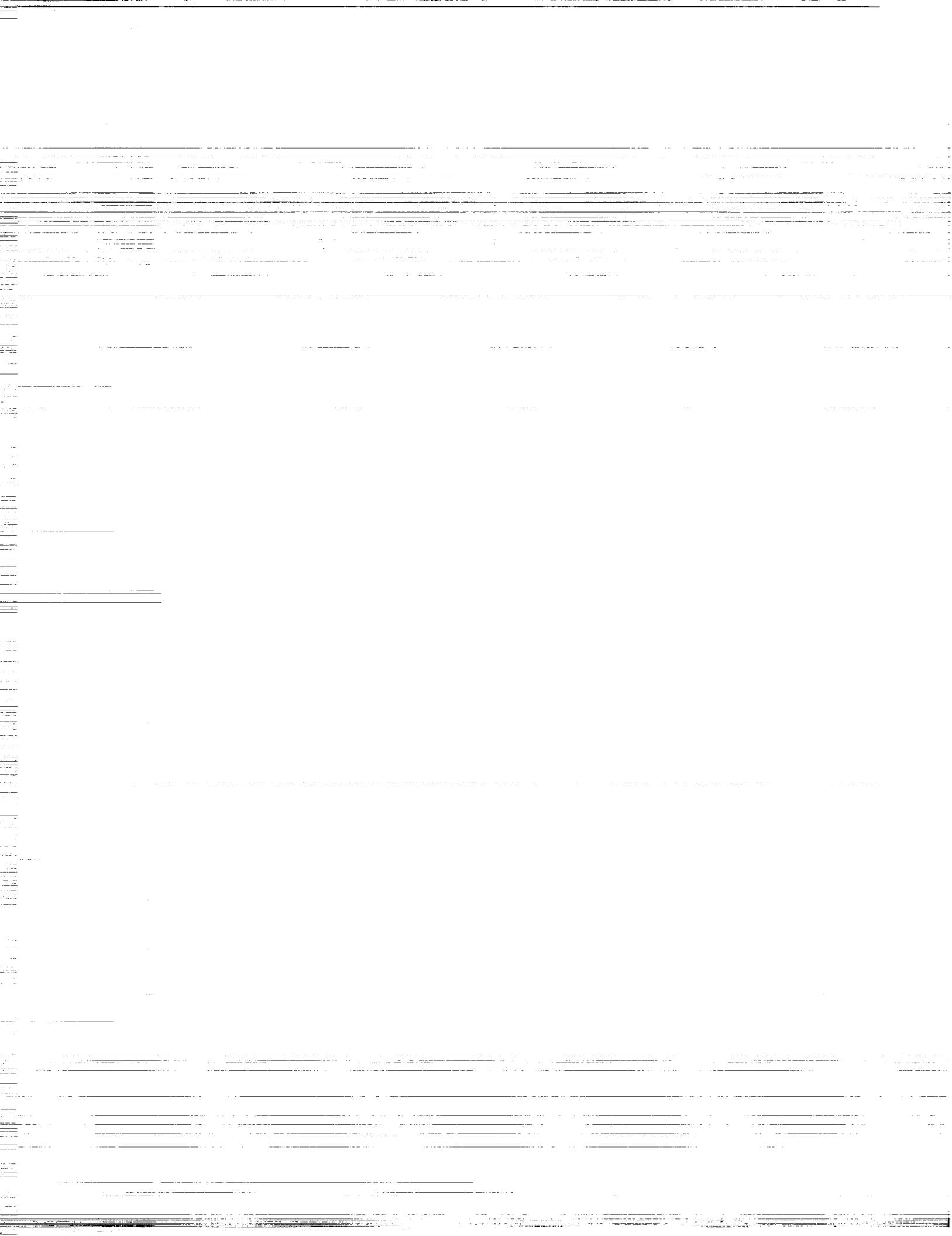


**AN INTEGRATED MODELING STUDY FOR COORDINATED
OBSERVATIONS OF H, O, OH, AND H₂O⁺ EMISSIONS IN THE COMA AND ION
TAIL OF THE COMET HALE-BOPP**

FINAL REPORT

**Atmospheric and Environmental Research, Inc.
131 Hartwell Avenue
Lexington, Massachusetts**



**An Integrated Modeling Study for
Coordinated Observations of H, O,
OH, and H₂O⁺ Emissions in the Coma
and Ion Tail of Comet Hale-Bopp**

William H. Smyth

Atmospheric and Environmental Research, Inc.
131 Hartwell Avenue
Lexington, MA 02421-3126

Final Report for the Period of
November 2, 1998 to November 1, 2001

I. INTRODUCTION

This project has two overall objectives. One objective is to advance our general understanding of both the comet neutral atmosphere and the cometary plasma in the atmosphere and ion tail. The other objective is to obtain specific key information about comet Hale-Bopp that is generally important for Hale-Bopp studies. The primary emphasis in this project is to analyze, in a self-consistent manner, excellent quality high resolution image and line profile observations obtained by the University of Wisconsin for H, O, OH, and H_2O^+ emissions from the inner coma, outer coma, and ion tail of Hale-Bopp.

The information on the spatial and velocity distributions of H_2O neutral and ionized photo-products in the inner coma, outer coma, and in the H_2O^+ ion tail is of substantial and direct importance in the development of an integrated understanding of the complex structure and dynamics of the neutral and plasma species in the atmosphere of Hale-Bopp in particular and comets in general. The H_2O production rate of Hale-Bopp is determined and, together with the other information related to the structure and dynamics of the neutral and plasma atmospheres obtained in this study, provide critical information important for a wide variety of research conducted by other groups.

II. RESEARCH

2.1 Overview

A coordinated and comprehensive multi-wavelength synoptic ground-based observing campaign of coma emissions from comet Hale Bopp was undertaken in 1997 by the University of Wisconsin-Madison and NASA-Goddard. The program involved several instruments, telescopes, and key investigators as summarized in Table 1. The emissions observed in the program were OH 3080 Å (Harris et al. 2001), [O I] 6300 Å (Morgenthaler et al. 2001), H_2O^+ (Anderson 1997/1999), hydrogen Balmer-alpha (Morgenthaler et al. 2002), and NH_2 6330 Å (Glinski et al. 2001) as well as [C I] 9850 Å (Oliversen et al. 2001), CN 3879 Å, C_2 5141 Å, C_3 4062 Å, [C I] 1657 Å, and the UV continuum (Harris et al. 1997/1999). The species of interest here are H, O, OH, and H_2O^+ , which are produced by photodissociation of H_2O , the dominant gas species in the cometary atmosphere, and by various photon and ion reactions in the coma.

The reduction and calibrations of the emission observations were undertaken by different investigators at the University of Wisconsin and NASA-Goddard. During the course of this project, the initial Principal Investigator for the Observing Program, Dr. Frank Scherb, retired, and a new Principal Investigator, Dr. Walter M. Harris, has continued to direct the program of

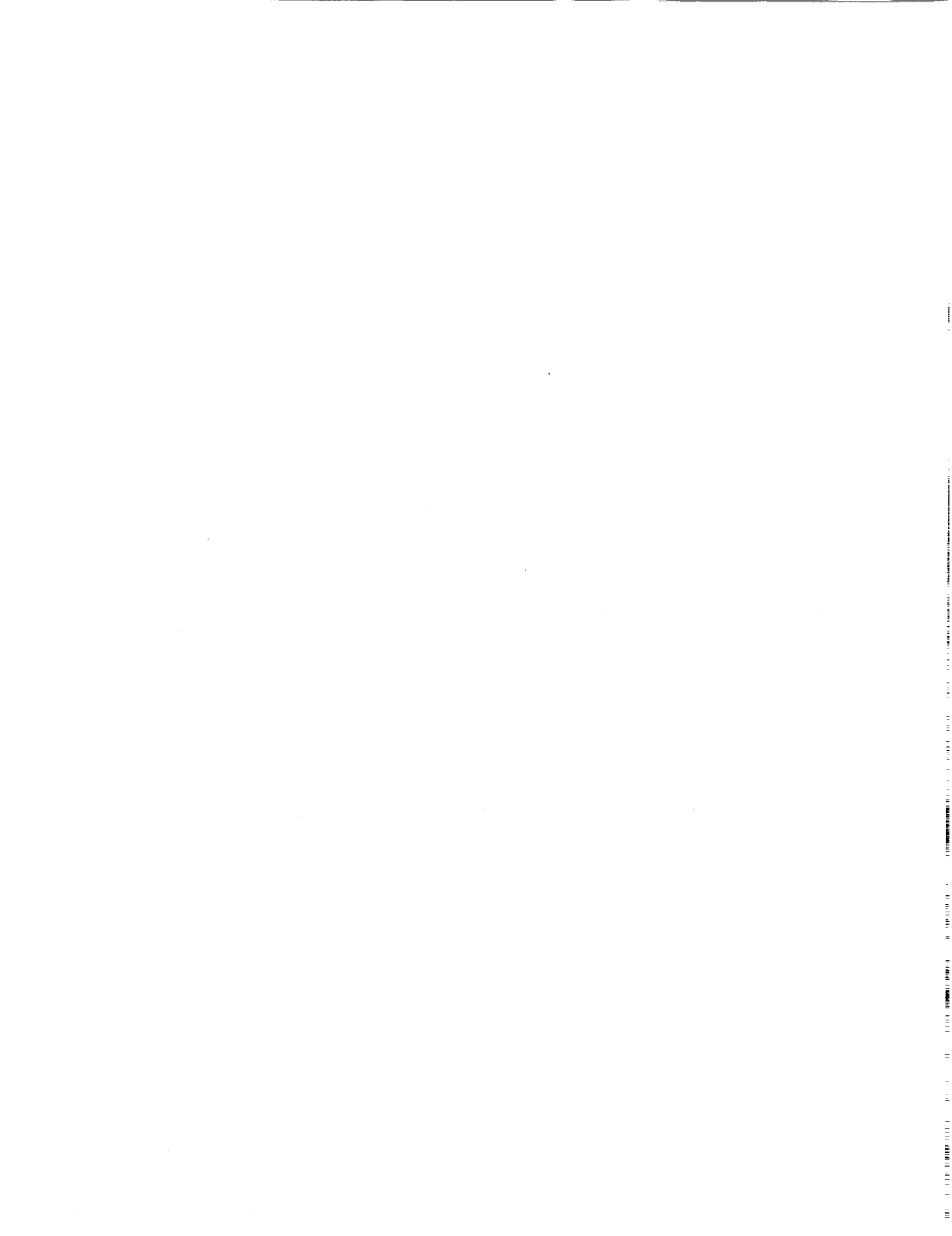
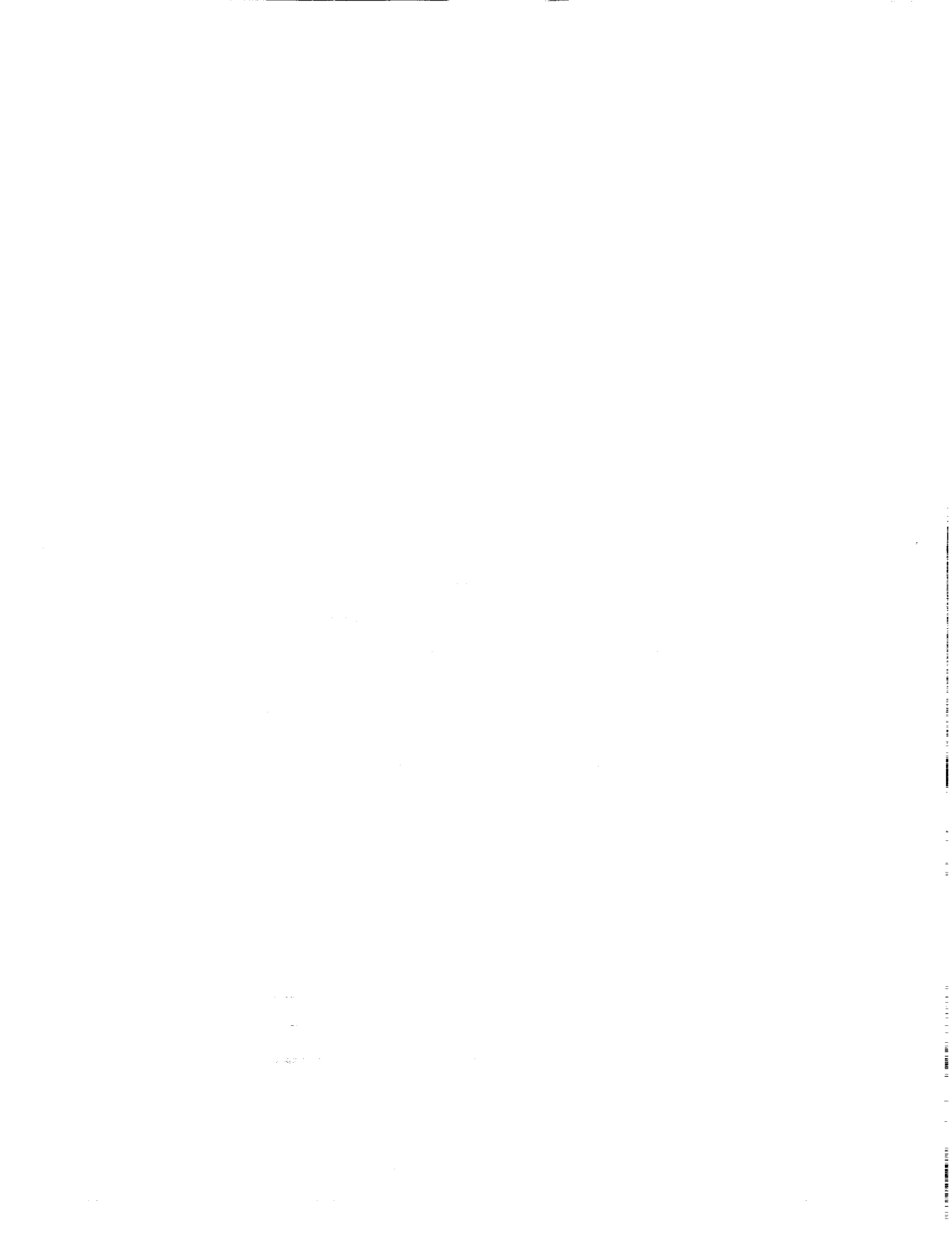


Table 1. Comet Hale-Bopp: Coordinated Synoptic Observations

Observational Program	Instrument & Telescope (FOV/Spatial Resolution)	Key Investigator(s)
Doppler-resolved ($R \sim 1.5 \times 10^4$) Spectra and Images of [OI] 6300 \AA and H_2O^+ Emission Lines	WHAM Dual-etalon 150 mm Fabry-Perot at Kitt Peak (1° field of view)	R.J. Oliverson, F.L. Roesler, F. Scherb
Adjustable Spatial Array of 96 Medium-resolution ($R=1 \times 10^4$) Spectra, over Spectral Interval of 6150-6350 Angstroms (NH_2 , [OI] 6300 \AA , H_2O^+)	Hydra and Densapak (multi-fiber optic echelle spectrograph) at WIYN Telescope (96 adjustable fibers, each fiber Field of view = 3 arcsec)	C.M. Anderson
High Resolution ($R \sim 0.6-1 \times 10^5$) Spectra of [OI] 6300 \AA , $\text{H}\alpha$, NH_2 , [CI] 9850 \AA	Dual-etalon 50 mm Fabry-Pérot at McMath-Pierce Solar Telescope	R.J. Oliverson, F.L. Roesler, F. Scherb
High Spatial Resolution Images of OH, CN, C_2 (5141 \AA), C_3 (4062 \AA), H_2O^+ , and Continuum Emissions from the Coma	Narrow-band Interference Filters/2048x2048 CCD Camera at KPNO Burrell Schmidt Telescope (69 arcmin/2.2 arcsec)	W.M. Harris, S. Limaye, B.E. Mueller
Images of CN, C_2 , (5141 \AA), H_2O^+ and Continuum Blue Emissions from the Coma	Narrow-band Interference Filters at Mt. Wilson 100 in Telescope, Adopt System (AO)	W.M. Harris
Doppler-resolved ($R \sim 1.5 \times 10^4$) Spectra and Images of H_2O^+ Emission Lines from the Coma and Ion Tail	Dual-etalon 150 mm Fabry-Perot at McMath-Pierce Solar Telescope (west aux.)	F. Scherb, F.L. Roesler, R.J. Oliverson

data reduction under a new NASA project. The processes of data reduction and calibration began with the [O I] 6300 \AA data set acquired by several instruments (see Table 1) and encountered a number of unexpected problems that severely delayed its completion. The analysis work in this project was therefore significantly postponed and curtailed, and a two-year no-cost extension was granted to attempt to adjust to this delayed schedule. The data reduction and calibration of the [O I] 6300 \AA data were eventually completed. The analysis of the [O I] 6300 \AA data yielded an unexpected result and is described in a paper by Morgenthaler et al. (2001; in Appendix A). The OH data have subsequently been reduced and preliminarily analyzed at the University of Wisconsin and are described in a paper by Harris et al. (2001; in Appendix B). The H- α data are currently undergoing reduction, and it is anticipated that an H- α paper will be written in 2002. The H_2O^+ data has undergone initial reduction (Andersen et al.

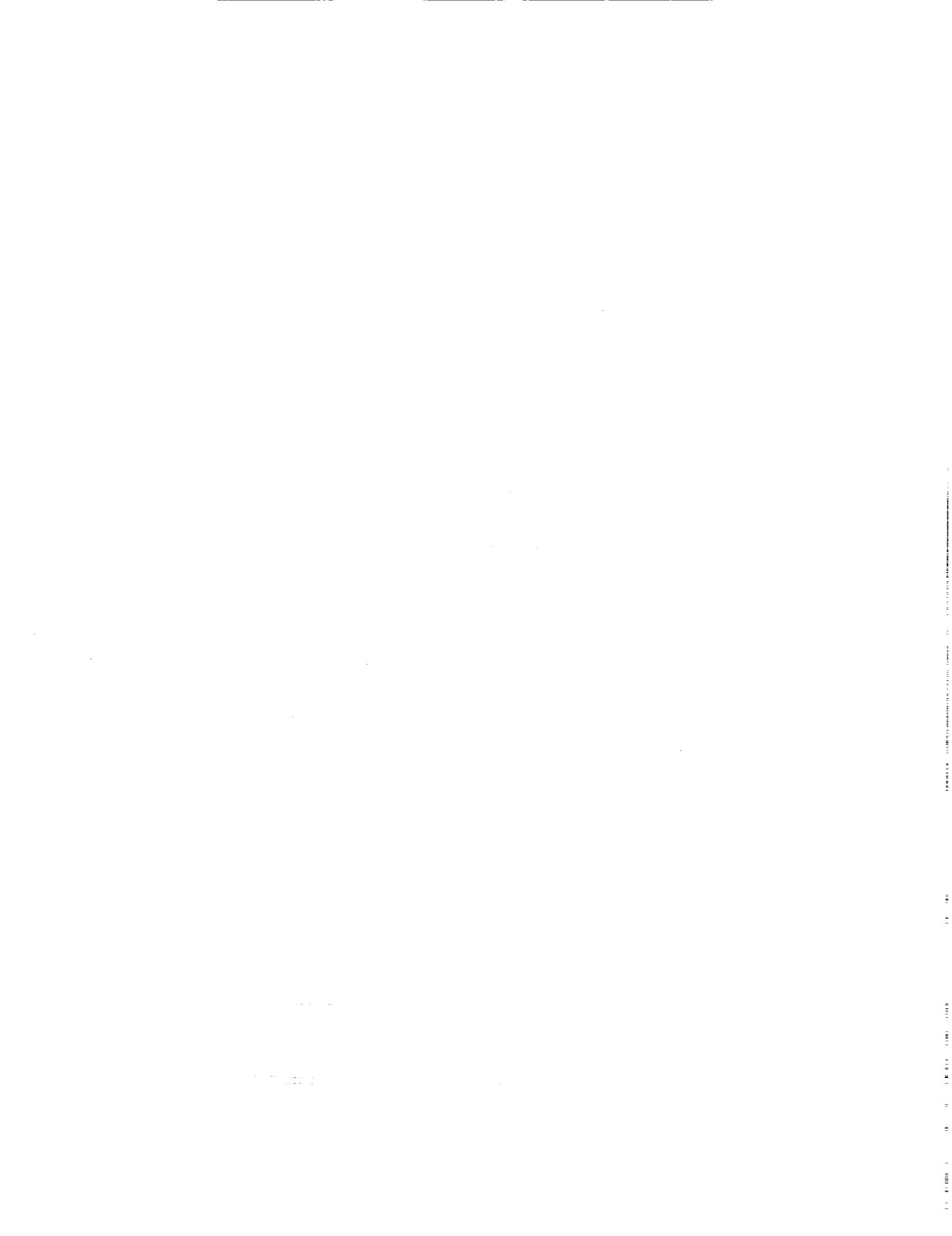


1997/1999) and preliminary MHD analysis (Gombosi et al. 1997/1999) and more recently final reduction, but has not yet progressed to the point of producing a final modeling analysis paper. A brief summary of the investigations for the [O I] 6300 Å, OH, H- α , and H₂O⁺ data sets is given in the following subsections.

2.2 [O I] 6300 Å Observations

Observations of the coma of comet Hale-Bopp in [O I] 6300 Å emissions were acquired between February 22 to April 21, 1997 by four instruments on Kitt Peak (see first three rows of Table 1): the Wisconsin H α Mapper (WHAM), two configurations (densepac and hydra) of the 3.5 m WIYN Telescope multi-object spectrograph (MOS), and a 50 mm dual-etalon Fabry-Perot spectrometer. A detailed description of these observations, their reduction, and their interpretation is given in Appendix A, and only a brief summarized is given here. The spectra and image data for the WHAM observations with its wide 1° field of view centered on the comet nucleus cover an extremely large radial interval $\sim\pm 2 \times 10^6$ km from the comet nucleus. This radial interval includes an area larger than the entire detectable [O I] 6300 Å coma except in the direction of the dust tail, where a tailward asymmetry exist beyond $\sim 3 \times 10^5$ km. About 13% of the total [O I] 6300 Å emission can be attributed to the tailward asymmetry seen in the [O I] image. For the MOS observations, the densepac data cover the spatial range from $\sim 2,000$ to 25,000 km while the hydra data cover the range from $\sim 2,000$ to 4×10^5 km. The 50 mm dual-etalon Fabry-Perot spectrometer has an effective field of view diameter of ~ 4 arc min ($\sim\pm 2-3 \times 10^5$ km). The combination of the MOS and Fabry-Perot data thus covers a very large spatial scale of the coma from $\sim 2,000$ to 1×10^6 km, providing an unusual opportunity to investigate the production of O(¹D) over an unprecedented large radial expanse.

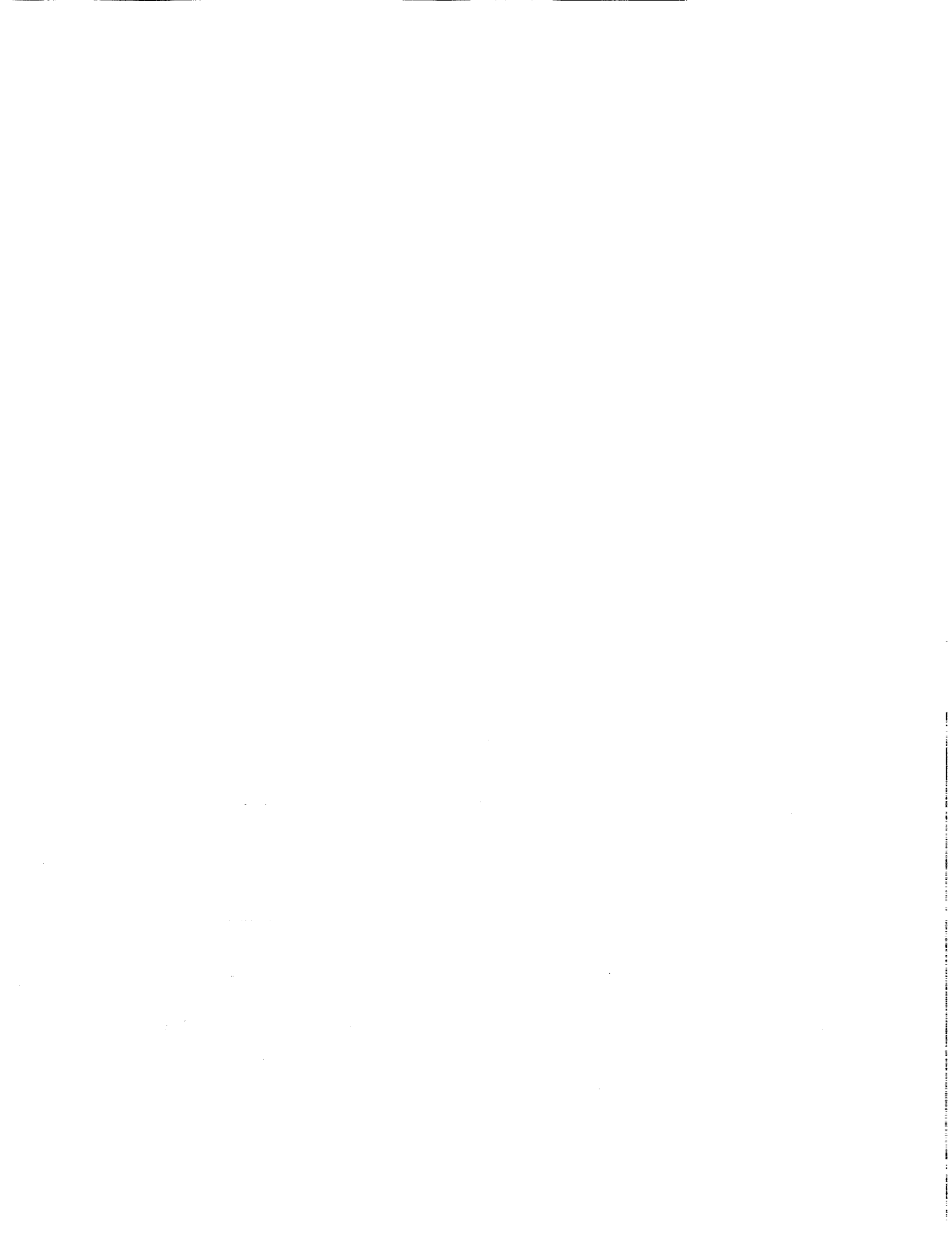
Analysis of the composite [O I] 6300 Å emission data for comet Hale-Bopp indicates a total production rate for atomic oxygen from the complete coma in the range 2.3 to 5.9×10^{30} atoms s⁻¹. Assuming only photochemistry of H₂O and its OH daughter product as the source of [O I] 6300 Å emission and using the standard H₂O and OH photodissociation branching ratios (van Dishoeck and Dalgarno 1984; Huebner et al. 1992), the corresponding production rate of H₂O is determined to be ~ 3 to 4 times larger than other independently derived H₂O production rates of $\sim 1 \times 10^{31}$ molecules s⁻¹. For distances that are restricted within the inner coma (inside of $\sim 1 \times 10^5$ k), where H₂O photodissociation is the dominant source of [O I] 6300 Å emission, the H₂O production rates determined from atomic oxygen [O I] 6300 Å emission data are, however, more consistent with the estimates of $\sim 1 \times 10^{31}$ molecules s⁻¹. This suggest that the excess [O I] 6300 Å emission in the outer coma is either produced by other sources than the photodissociation of the OH daughter product (which dominates in this spatial region) or by other non-H₂O



sources. Estimates based upon the production rates of other oxygen-bearing volatiles (e.g., CO, CO₂), however indicate that at most only ~30 % of the observed excess [O I] 6300 Å emission could be coming from them. It is then likely that the bulk of the excess [O I] 6300 Å emission in the outer coma is coming from the photodissociation of OH, with more favorable branching ratios than the standard values adopted initially. An examination of the branching ratios indicates that perhaps ~60% of the excess [O I] 6300 Å emission in the outer coma might possibly be produced without requiring major modifications to other OH branching ratios or the total OH photodissociation lifetime. Improved laboratory and theoretical photodissociation cross sections for H₂O and OH are therefore needed to better understand the physics of cometary comae.

2.3 OH Observations

Image observations of the coma of comet Hale-Bopp in the OH in 3080 Å emissions were acquired with a narrow-band interference during March 24-29, 1997 and on April 8, 1997 using the 0.9 m Burrell Schmidt Telescope at the Kitt Peak Observatory. A detailed description of the best observations on March 28 and April 8, 1997, their reduction, and preliminary interpretation are given in Appendix B, and only a brief summarized is given here. These observations from Hale Bopp provided a field of view exceeding 10⁷ km, which is sufficient to measure the complete OH coma of the comet. By summing all of the OH emissions over the complete coma, the OH production rate was determined to be $7.9 (\pm 1.2) \times 10^{30}$ and $9. (\pm 1.2) \times 10^{30}$ molecules s⁻¹ on March 28 and April 8, 1997, respectively. For OH produced only from photodissociation of H₂O, these OH production rates correspond to H₂O production rates of $0.931 (\pm 0.14) \times 10^{31}$ and $1.08 (\pm 0.16) \times 10^{31}$ molecules s⁻¹, respectively, for the two dates and are very similar to H₂O production rates obtained by other observers. The paper in Appendix B then presents the radial OH brightness profiles. These profiles exhibit an azimuthal asymmetry beyond cometocentric distances of ~10⁵ km which is more spatially enhanced in the anti-sunward and tailward directions, extending into the region between the dust and ion tails. This is the same location in which the asymmetric enhancement in the [O I] 6300 Å emission was observed, as described in Section 2.2. The remaining part of the paper examines the asymmetric nature of the radial profile using a highly oversimplified and somewhat inappropriate method based upon a constant-outflow-velocity Haser model and speculates as to the reason for this spatial asymmetry. Analysis of these data with a more physical-based model is, however, required to better understand the dynamic outflow and asymmetric radial structure of the OH coma for the large-production-rate comet Hale Bopp. This interesting modeling work, originally to be initiated in this project, was not able to be undertaken because of the very long time delay in the reduction of OH data at the University of Wisconsin-Madison.



2.4 H- α Observations

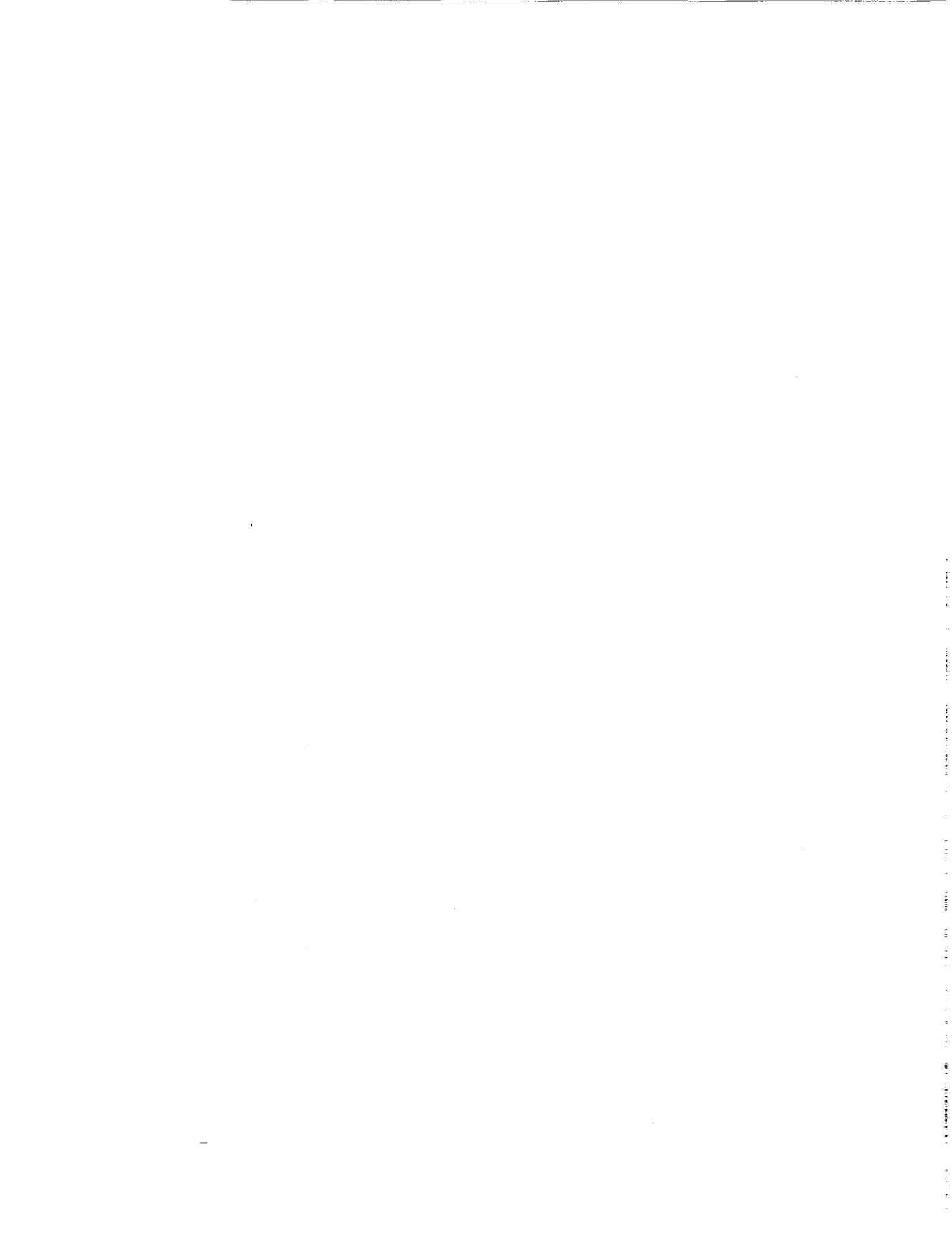
Observations of the coma of comet Hale-Bopp in the H α (6563 Å) emissions were acquired on six nights in 1997 as summarized in Table 2 using the dual-etalon 50 mm Fabry-Pérot at McMath-Pierce Solar Telescope (see Table 1), one of the instruments also used to measure the [O I] 6300 Å emission from the comet coma, as discussed in Section 2.2. The field of view for the observations was 4 arc min in diameter and was centered sunward of the nucleus, as indicated in Table 2. The observations were acquired both before and after perihelion, which was on April 1, 1997. Extraction of the spectra from the Fabry-Perot ring images was complicated by obscuration of the telescope FOV due to Hale-Bopp's low elevation. Using the recently completed Wisconsin H α Mapper (WHAM) survey (<http://www.astro.wisc.edu/wham>),

Table 2. 1997 Observational Parameters for H- α Data for Comet Hale-Bopp

Date	R (AU)	RDOT (km/s)	Δ (AU)	Δ DOT (km/s)	FWHM (Geocorona)	FWHM (Comet)	Comments
February 10	1.2566	-19.56	1.8163	-34.15			Not Good
February 15	1.2017	-18.75	1.7209	-33.09	16.5 (cut off)	17.1	Good 5' Sunward (?)
	1.2017	-18.75	1.7209	-33.09			Not good
March 5	1.0291	-13.85	1.4273	-21.89	7.9	11.8	Very good 5.8' Sunward
April 14	0.9431	7.58	1.4970	24.95	8.5	11.4	Good 5' Sunward
	0.9431	7.58	1.4971	24.95	6	11.	Good 5' Sunward
	0.9431	7.58	1.4972	24.96	6	9.0	Good 5' Sunward
April 15	0.9478	8.13	1.5120	25.57			Not Good
	0.9478	8.14	1.5122	25.57	12.0	13.7	Good 5' Sunward
	0.9479	8.14	1.5123	25.57	8.7	7.1	OK
April 16	0.9525	8.64	1.5264	26.10	15.1	13.3	Good 5' Sunward
	0.9525	8.65	1.5266	26.11	11.7	12.7	Good 5' Sunward
	0.9526	8.65	1.5267	26.12	11.4	13.1	Good 5' Sunward

R is the heliocentric distance of the comet; RDOT is the Sun-comet radial velocity; Δ is the geocentric distance of the comet; Δ DOT is the Earth-comet radial velocity.

the Galactic H- α emission was subtracted from the spectra. In this reduction process, a Voigt profile is fit to the geocoronal H α emission, which was also subtracted. The measured cometary H α line widths of 12-14 km s⁻¹ (FWHM) in Table 2 are insensitive to the spectral extraction technique, whereas the line intensity is relatively more sensitive. Two examples of the reduced spectra for the cometary H α emission are shown in Figure 1 for March 5 (pre-perihelion) and April 16 (post-perihelion).



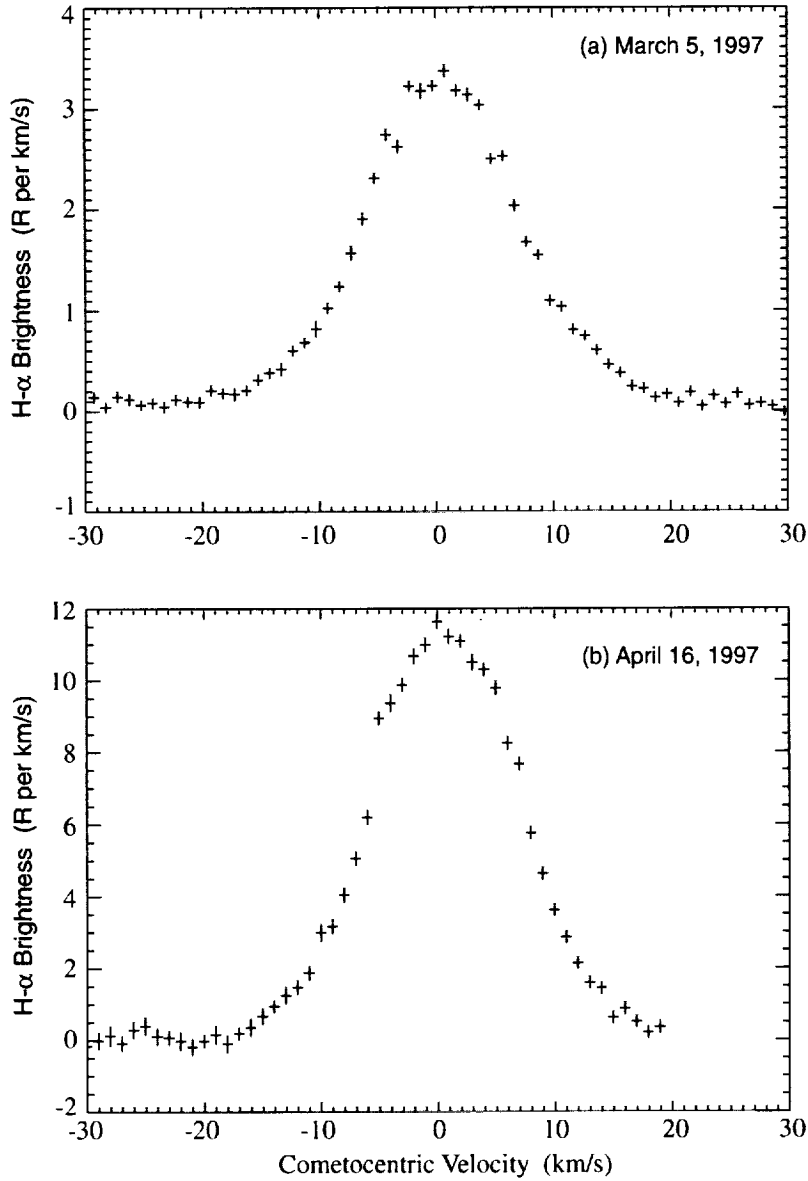
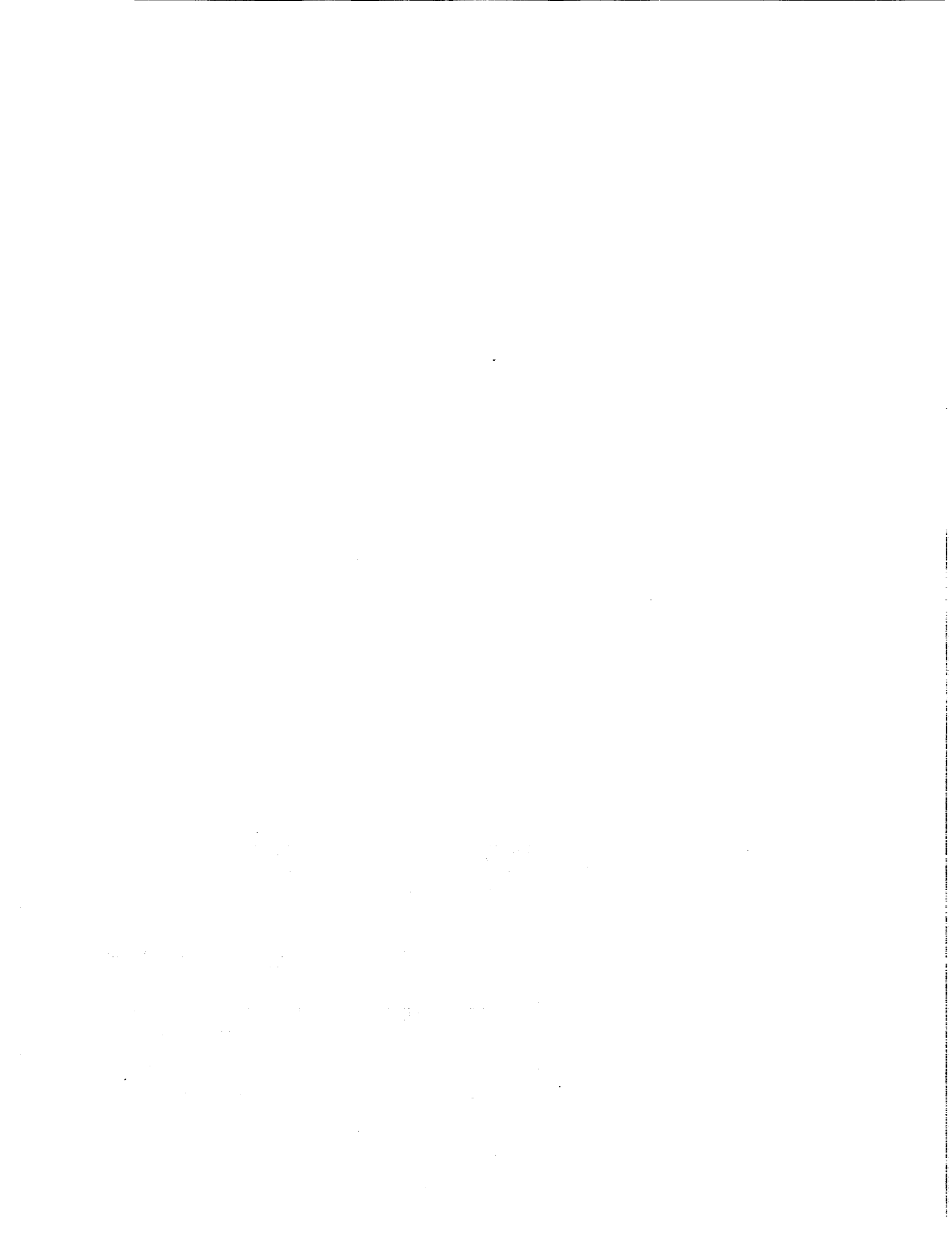


Figure 1. H α Line Profiles for Comet Hale Bopp. Reduced and calibrated line profiles for H α emission from the coma are shown in (a) for March 5, 1997 and in (b) for April 16, 1997. Both galactic and geocoronal emissions have been removed.

The reduction and calibration of the H- α line profiles for Hale Bopp were completed at the University of Wisconsin-Madison at the very end of this project. The data were hence not available for analysis with the Monte Carlo Particle Trajectory Model (MCPTM) at AER. Such an analysis would be parallel to an earlier analysis of the observed H- α line profiles for comet P/Halley (Smyth et al. 1993). Such an analysis would provide an independent method to probe the photodissociative branching ratios (and their related exothermic energy) for H₂O and OH, with

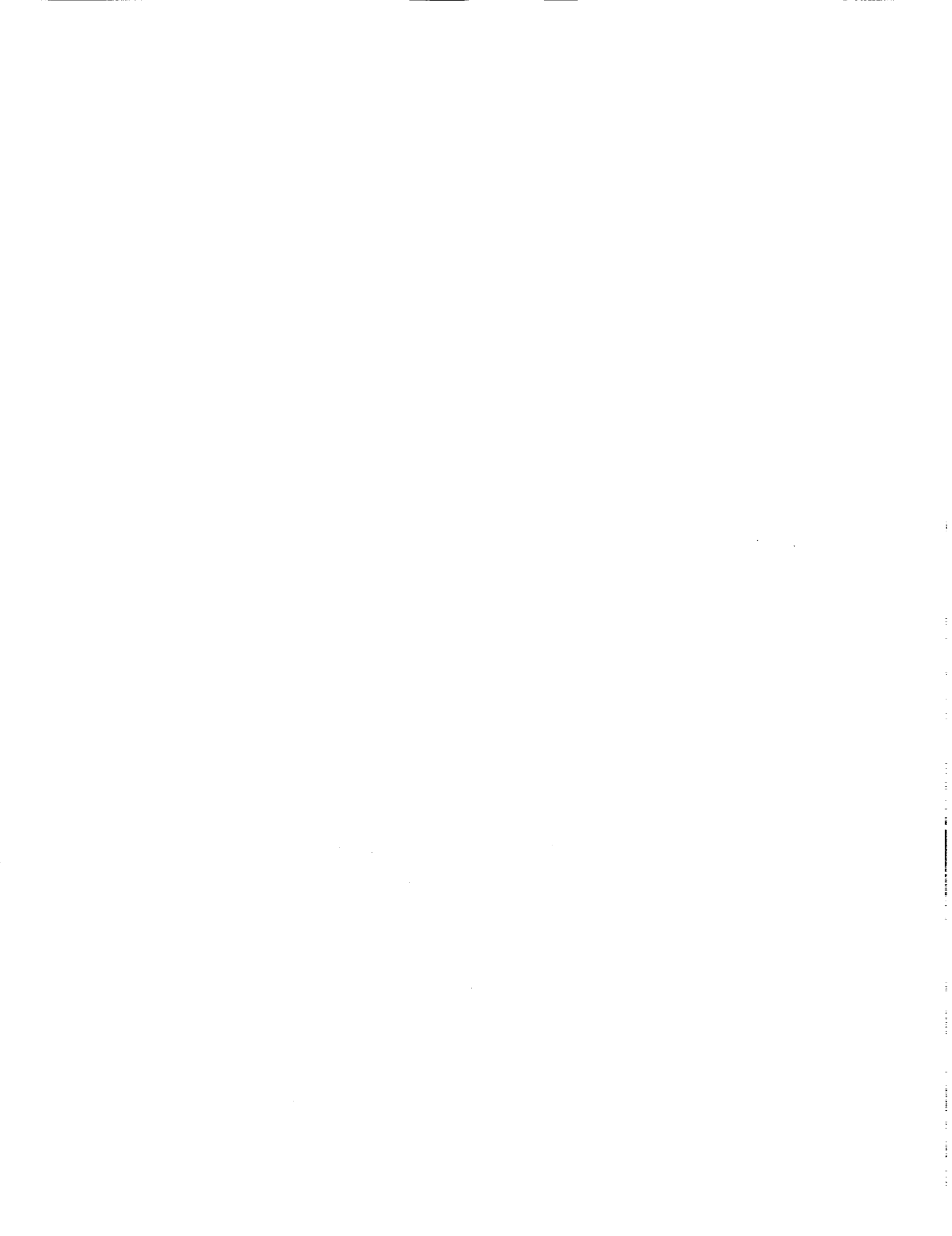


the latter molecule being of particular importance in addressing issues for the enhanced [O I] 6300 Å emission in the coma of Hale Bopp discussed in Section 2.2. The reduced and calibrated H- α line profiles are to be presented (Morgenthaler et al. 2002) for the first time at the Tenereife Meeting for comet Hale Bopp in January 2002.

2.5 H₂O⁺ Observations

Observations of the coma of comet Hale-Bopp in various H₂O⁺ emission lines were acquired using the Hydra and Densapak (multi-fiber optic echelle spectrograph) at WIYN Telescope and also the Dual-etalon 150 mm Fabry-Perot at McMath-Pierce Solar Telescope on the west auxiliary (see Table 1). The Hydra and Densapak data were initially reduced for a preliminary brightness calibration in 1997 (Anderson 1997/1999) and have been more recently reduced, but not yet published, with a final brightness calibration. The Fabry-Perot data have not yet been reduced. The Hydra and Densapak data measured for each fiber-location 19 different H₂O⁺ emission lines within the wavelength range in the vicinity of 6198 Å with 3 or 4 lines being much brighter than others. The velocity and brightness of H₂O⁺ in the coma from $\sim 10^5$ km sunward to $\sim 10^6$ km tailward were determined from the emission line data.

The abundance and velocity of H₂O⁺ as well as other cometary ions (O⁺, OH⁺, H₃O⁺, CO⁺, and S⁺) are determined by cometary ion chemistry in the coma as well as the three-dimensional complex interaction of the solar wind plasma with the coma and cometary plasma. The production of H₂O⁺ is thought to occur primarily through photoionization ($\text{H}_2\text{O} + h\nu \rightarrow \text{H}_2\text{O}^+ + e$) and charge exchange ($\text{H}^+ + \text{H}_2\text{O} \rightarrow \text{H}_2\text{O}^+ + \text{H}$), while the destruction of H₂O⁺ is thought to occur primarily through charge exchange ($\text{H}_2\text{O}^+ + \text{H}_2\text{O} \rightarrow \text{H}_3\text{O}^+ + \text{OH}$) and the electron impact ($\text{H}_2\text{O}^+ + e \rightarrow \text{products}$) reactions. In this project, the Co-Investigator, Dr. M. R. Combi, had the primary responsibility for modeling both the complex interaction of solar wind plasma with the cometary coma cometary and the cometary ion chemistry for H₂O⁺ and for investigating the H₂O⁺ observational data for comet Hale Bopp. The adopted approach was to use the three-dimensional MHD model developed in the last few years under the leadership of Dr. T. I. Gombosi at the Space Physics Research Laboratory of the University of Michigan to solve the coupled continuity, momentum, energy, and magnetic field equations for a single plasma fluid and then use this MHD flow field solution in a coupled continuity equations including cometary ion chemistry for the ion species. The model produces two-dimensional column abundances and average line-of-sight velocities for the observed H₂O⁺ fluorescence band emissions which can be used for comparison/analysis of the observed spatial and spectral distributions of H₂O⁺.



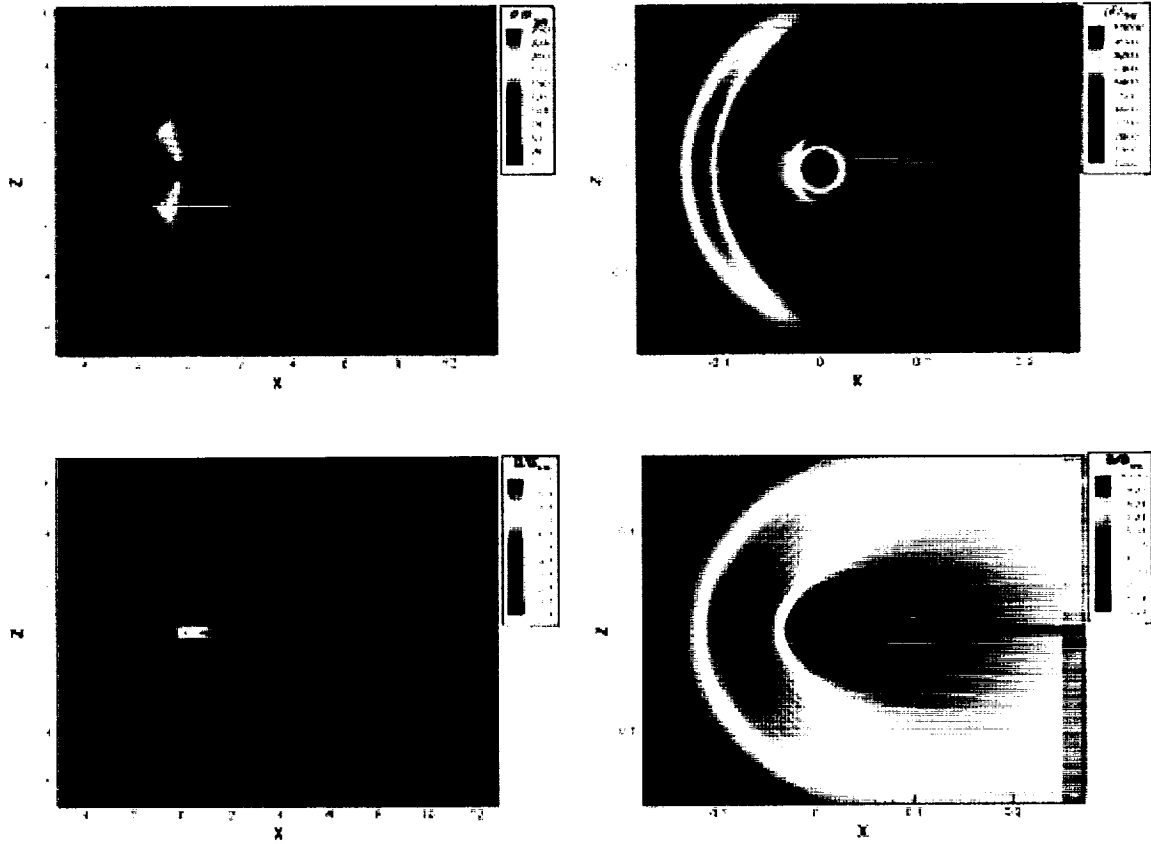
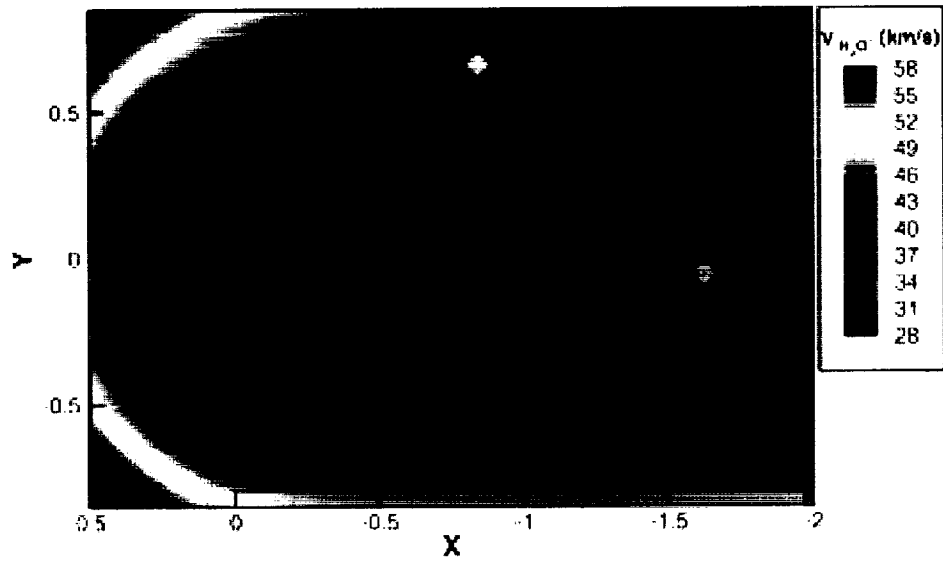


Figure 2. MHD Model Results for Comet Hale-Bopp. The top row shows plots of the plasma pressure (left) and density (right) in normalized units. The bottom row shows plots of the magnetic field in cuts parallel to the IPM with field-line draping, for a large field of view (left) and a close-up field of view (right).

Comparisons of model calculations with Hydra and Densepak measurements of Dr. Christopher Anderson of the University of Wisconsin were presented at the Hale-Bopp conference in Tenerife in 1998. A model description and calculations for Hale-Bopp were published in *Earth, Moon and Planets* (Gombosi et al. 1997/1999). Comparisons of model results with the Hydra observations of the Wisconsin group were also described in a paper in *Earth, Moon and Planets* (Anderson, 1997/1999). A more thorough analysis of the data has been ongoing after the first publications, however uncertainties regarding the absolute brightness calibration of the spectral data have only recently been completely resolved. Figure 2 shows the primary output of the MHD calculations that sets the flow geometry and conditions throughout the interaction region. In running the MHD model, one needs to set the solar wind conditions: density, velocity, temperature, and frozen-in magnetic field magnitude and direction; and the comet coma conditions: production rate, composition and ionization rate. Therefore, some

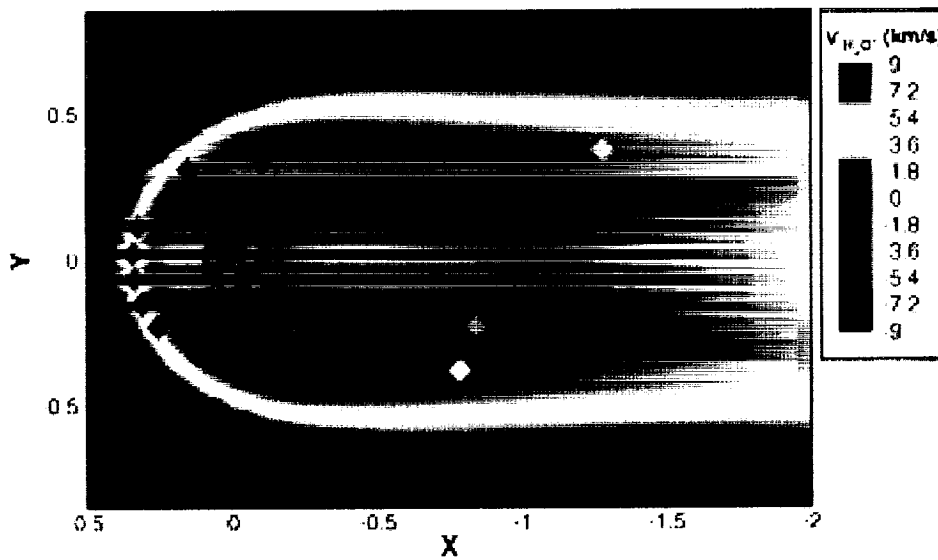


**H₂O⁺ line-of-sight velocities for comet Hale-Bopp
April 21, 1997 (slow solar wind conditions)**



Diamonds indicate measurements made using the Hydrapak instrument. Color contours indicate simulation results.

**H₂O⁺ line-of-sight velocities for comet Hale-Bopp
March 16, 1997 (fast solar wind conditions)**



Diamonds indicate measurements made using the Hydrapak instrument. Color contours indicate simulation results.

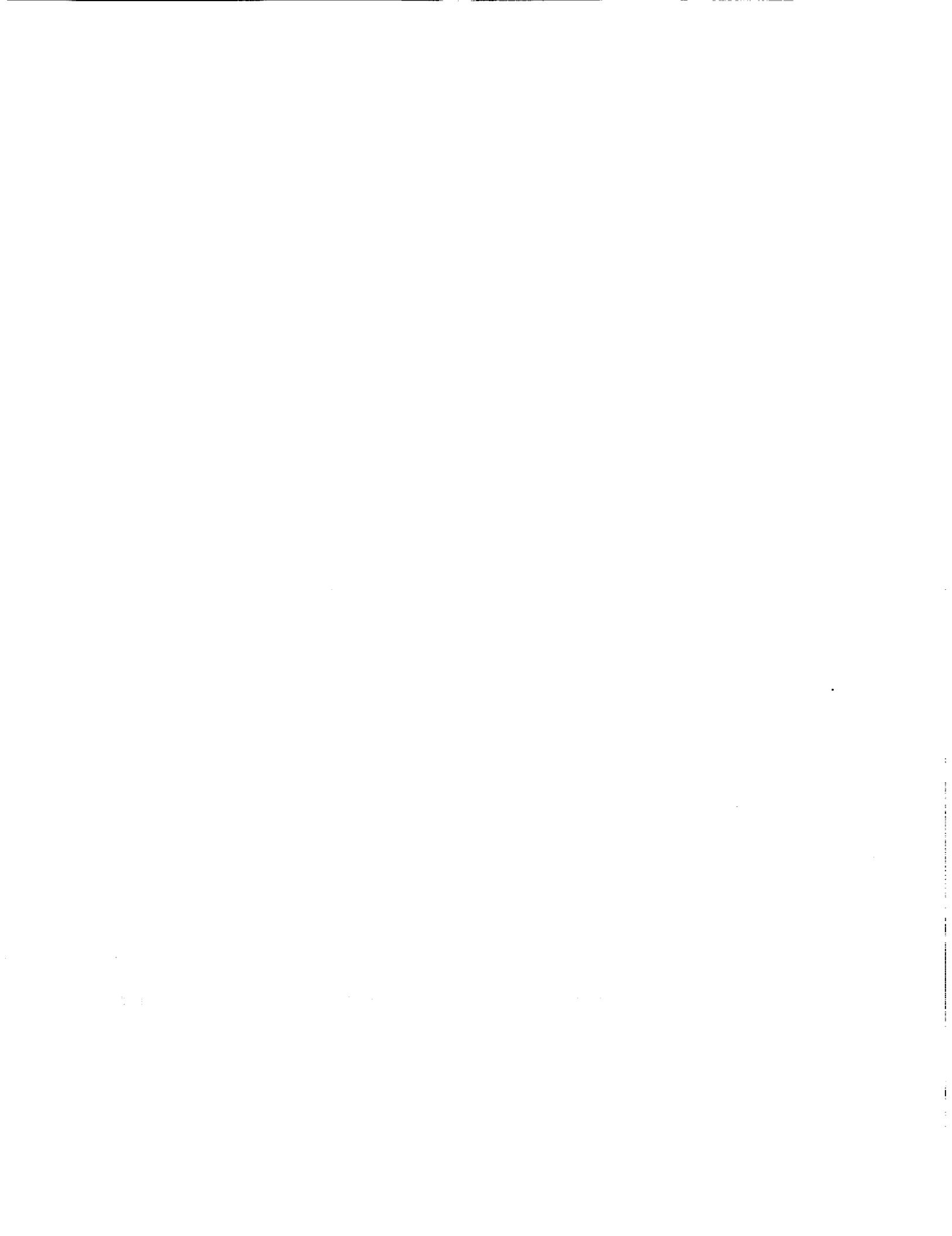
Figure 3. Comparison of MHD/Ion-chemistry calculations with Observations. The model calculation (false color legend) is compared with the densepac and hydra measurements (colored diamonds) for slow (above) and fast(below) solar wind conditions.

adjustment of parameters is necessary to obtain a good overall fit. Figure 3 shows a comparison of an ion-chemistry/MHD calculation with average line-of-sight velocities measured by the densepac and hydra measurements. The field gives the values predicted by the model and the diamonds give the measured values. The above and below figures are measurements made on dates when the comet was in the fast and slow solar wind. Comet Hale-Bopp in early 1997 was particularly noteworthy because of its very high solar ecliptic latitude.



References

- Anderson, C.M. (1997/1999) Fiberopically Multiplexed Medium Resolution Spectroscopy from the WIYN Telescope, H_2O^+ , [O I], and NH_2 , *Earth, Moon and Planet.* 78, 99-104.
- Glinski R.J., E.A. Post, and C.M. Anderson (2001) Fiberoptic Array Spectroscopy of NH_2 in Comet Hale-Bopp: Nature of the Rotational Energy Distributions, *Ap. J.* 550, 1131-1139.
- Harris, W.M., K.H. Nordsieck, F. Scherb, and E.J.Mierkiewicz (1997/1999) UV Photopolarimetric Imaging of C/1995 O1 (Hale-Bopp) with the Wide Field Imaging Survey Polarimeter WISP, *Earth, Moon and Planet.* 78, 161-167.
- Gombosi, T.I., K. Hansen, D.L. DeZeeuw, M.R. Combi, and K.G. Powell (1997/1999) Simulations of Comets: The Plasma Environment of Hale Bopp, *Earth Moon and Planets* 79, 179-202.
- Harris, W.H., F. Scherb, E.M. Mierkiewich, R. Oliverson, and J. Morgenthaler (2001) Production, Outflow Velocity, and Radial Distribution of H_2O and OH in the Coma of Comet C/1995 O1[Hale-Bopp] from Wide Field Imaging of OH, *Ap. J.*, submitted.
- Huebner, W.F., J.J. Keady, and S.P. Lyons (1992) Solar Photon Rates for Planetary Atmospheres and Atmospheric Pollutants, *Ast. & Space Sci.* 195, 1.
- Morgenthaler, J.P., W.H. Harris, F. Scherb, C.M. Andersen, R.J. Oliverson, N.E. Doane, M.R. Combi, M.L. Marconi, and W.H. Smyth (2001) Large Aperture [O I] 6300 Å Photometry of Comet Hale-Bopp: Implications for Photochemistry of OH, *Ap. J.* 563, 451-461.
- Morgenthaler, J.P., W.M. Harris, F.Scherb, Nathaniel E. Doane, and R.J. Oliverson (2002) Velocity Resolved Observations of H-alpha Emission from Comet Hale-Bopp, Paper submitted to the Hale-Bopp Tenerife 2002 Meeting.
- Oliverson R.J., N. Doane, F. Scherb, W.H. Harris, and J.P. Morgenthaler (2001) Measurements of [C I] 9850 Å Emissions from Comet Hale-Bopp, *Ap.J.*, submitted.
- Van Dishoeck, E.F., and A. Dalgarno (1984) The Dissociation of OH and OD in Comets by Solar Radiation, *Icarus* 59, 305-313.



REPORT DOCUMENTATION PAGE

Form Approved
OMB No. 0704-0188

Public reporting burden for this collection of information is estimated to average 1 hour per response, including the time for reviewing instructions, searching existing data sources, gathering and maintaining the data needed, and completing and reviewing the collection of information. Send comments regarding this burden estimate or any other aspect of this collection of information, including suggestions for reducing this burden, to Washington Headquarters Services, Directorate for Information Operations and Reports, 1215 Jefferson Davis Highway, Suite 1204, Arlington, VA 22202-4302, and to the Office of Management and Budget, Paperwork Reduction Project (0704-0188), Washington, DC 20503.

1. AGENCY USE ONLY (Leave blank)		2. REPORT DATE December 14, 2001	3. REPORT TYPE AND DATES COVERED Final: November 2, 1998 to November 1, 2001	
4. TITLE An Integrated Modeling Study for Coordinated Observations of H, O, HO, and H ₂ O ⁺ Emissions In the Coma and Ion Tail of Comet Hale Bopp			5. FUNDING NUMBERS NASW-97020	
6. AUTHORS W. H. Smyth				
7. PERFORMING ORGANIZATION NAME(S) AND ADDRESS(ES) Atmospheric and Environmental Research, Inc. 131 Hartwell Avenue Lexington, MA 02421-3126			8. PERFORMING ORGANIZATION REPORT NUMBER P-718	
9. SPONSORING/MONITORING AGENCY NAME(S) AND ADDRESS(ES) NASA Headquarters Headquarters Contract Division Washington, DC 20546			10. SPONSORING/MONITORING AGENCY REPORT NUMBER	
11. SUPPLEMENTARY NOTES				
12a. DISTRIBUTION/AVAILABILITY STATEMENT			12b. DISTRIBUTION CODE	
13. ABSTRACT (Maximum 200 words) A coordinated and comprehensive multi-wavelength synoptic ground-based observing campaign of coma emissions from comet Hale Bopp was undertaken in 1997 by the University of Wisconsin-Madison and NASA-Goddard. Progress made in the reduction and analysis of observations for cometary [O I] 6300 Å, OH (3080 Å), H-α (6563 Å), and H ₂ O ⁺ emission lines are reported.				
14. SUBJECT TERMS Comet Hale-Bopp, atmosphere, ion tail			15. NUMBER OF PAGES 13 + Appendix A & B	
			16. PRICE CODE	
17. SECURITY CLASSIFICATION OF REPORT Unclassified	18. SECURITY CLASSIFICATION OF THIS PAGE Unclassified	19. SECURITY CLASSIFICATION OF ABSTRACT Unclassified	20. LIMITATION OF ABSTRACT Unlimited	

NSN 7540-01-280-5500

Computer Generated

STANDARD FORM 298 (Rev 2-89)
Prescribed by ANSI Std Z39-18
298-102

Appendix A

Large-Aperture [O I] 6300 Å Photometry of Comet Hal-Bopp: Implications for the
Photochemistry of OH

REPORT DOCUMENTATION PAGE

Form Approved
OMB No. 0704-0188

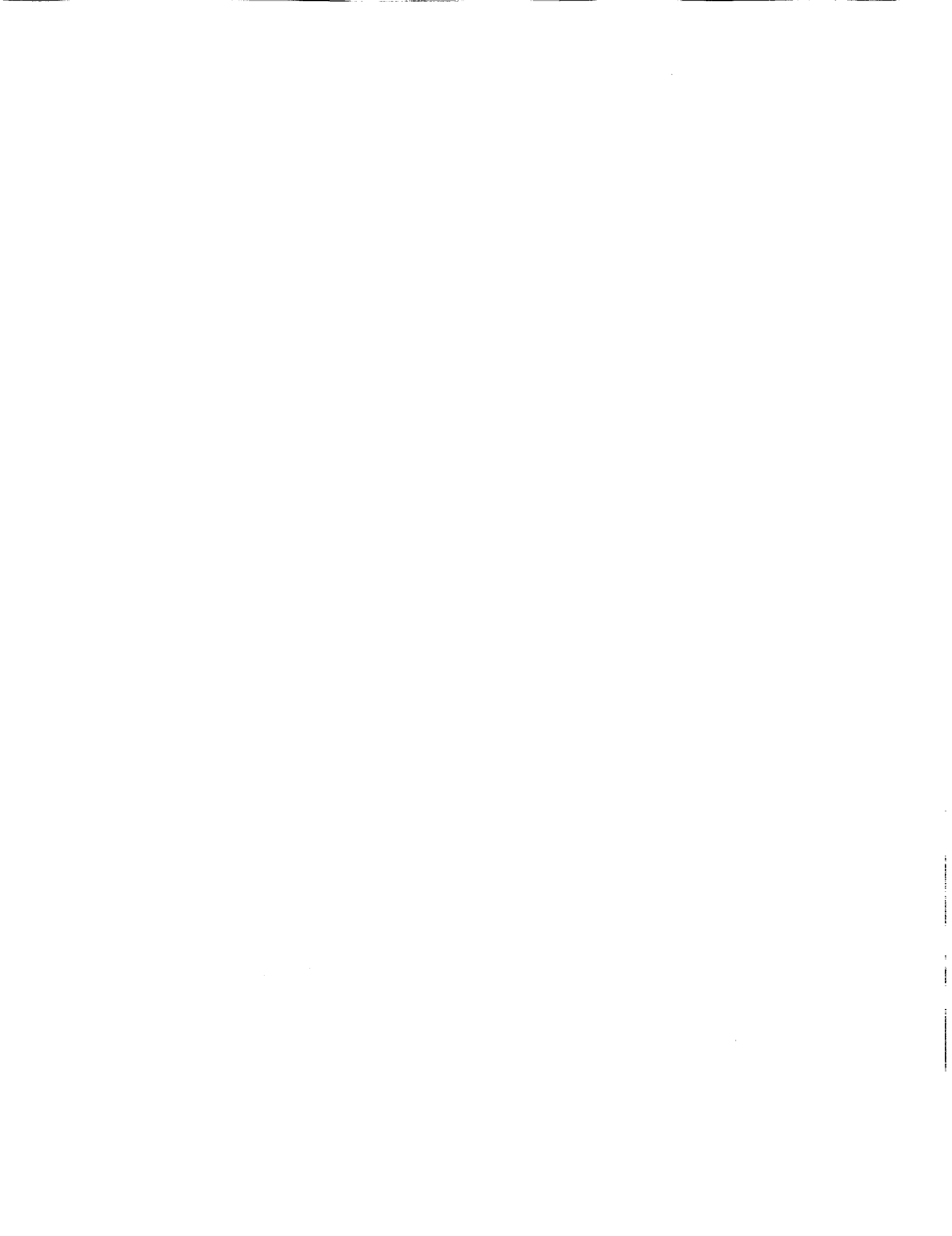
Public reporting burden for this collection of information is estimated to average 1 hour per response, including the time for reviewing instructions, searching existing data sources, gathering and maintaining the data needed, and completing and reviewing the collection of information. Send comments regarding this burden estimate or any other aspect of this collection of information, including suggestions for reducing this burden, to Washington Headquarters Services, Directorate for Information Operations and Reports, 1215 Jefferson Davis Highway, Suite 1204, Arlington, VA 22202-4302, and to the Office of Management and Budget, Paperwork Reduction Project (0704-0188), Washington, DC 20503.

1. AGENCY USE ONLY <i>(Leave blank)</i>	2. REPORT DATE December 14, 2001	3. REPORT TYPE AND DATES COVERED Final: November 2, 1998 to November 1, 2001	
4. TITLE An Integrated Modeling Study for Coordinated Observations of H, O, HO, and H ₂ O ⁺ Emissions In the Coma and Ion Tail of Comet Hale Bopp		5. FUNDING NUMBERS NASW-97020	
6. AUTHORS W. H. Smyth			
7. PERFORMING ORGANIZATION NAME(S) AND ADDRESS(ES) Atmospheric and Environmental Research, Inc. 131 Hartwell Avenue Lexington, MA 02421-3126		8. PERFORMING ORGANIZATION REPORT NUMBER P-718	
9. SPONSORING/MONITORING AGENCY NAME(S) AND ADDRESS(ES) NASA Headquarters Headquarters Contract Division Washington, DC 20546		10. SPONSORING/MONITORING AGENCY REPORT NUMBER	
11. SUPPLEMENTARY NOTES			
12a. DISTRIBUTION/AVAILABILITY STATEMENT		12b. DISTRIBUTION CODE	
13. ABSTRACT <i>(Maximum 200 words)</i> A coordinated and comprehensive multi-wavelength synoptic ground-based observing campaign of coma emissions from comet Hale Bopp was undertaken in 1997 by the University of Wisconsin-Madison and NASA-Goddard. Progress made in the reduction and analysis of observations for cometary [O I] 6300 Å, OH (3080 Å), H-α (6563 Å), and H ₂ O ⁺ emission lines are reported.			
14. SUBJECT TERMS Comet Hale-Bopp, atmosphere, ion tail		15. NUMBER OF PAGES 13 + Appendix A & B	16. PRICE CODE
17. SECURITY CLASSIFICATION OF REPORT Unclassified	18. SECURITY CLASSIFICATION OF THIS PAGE Unclassified	19. SECURITY CLASSIFICATION OF ABSTRACT Unclassified	20. LIMITATION OF ABSTRACT Unlimited



Appendix A

Large-Aperture [O I] 6300 Å Photometry of Comet Hal-Bopp: Implications for the
Photochemistry of OH



LARGE-APERTURE [O I] 6300 Å PHOTOMETRY OF COMET HALE-BOPP: IMPLICATIONS FOR THE PHOTOCHEMISTRY OF OH

JEFFREY P. MORGENTHALER,¹ WALTER M. HARRIS,² FRANK SCHERB,^{1,3} CHRISTOPHER M. ANDERSON,⁴
RONALD J. OLIVERSEN,^{3,5} NATHANIEL E. DOANE,^{3,6,7} MICHAEL R. COMBI,⁸
MAXIMUS L. MARCONI,⁹ AND WILLIAM H. SMYTH¹⁰

Received 2001 April 17; accepted 2001 August 10

ABSTRACT

Large-aperture photometric observations of comet Hale-Bopp (C/1995 O1) in the forbidden red line of neutral oxygen ([O I] 6300 Å) with the 150 mm dual-etalon Fabry-Pérot spectrometer that comprises the Wisconsin H α Mapper and a 50 mm dual-etalon Fabry-Pérot spectrometer at the McMath-Pierce main telescope from 1997 late February to mid April yield a total metastable O(¹D) production rate of $(2.3\text{--}5.9) \times 10^{30} \text{ s}^{-1}$. Applying the standard H₂O and OH photodissociation branching ratios found in Huebner, Keady, & Lyon and van Dishoeck & Dalgarno, we derive a water production rate, $Q(\text{H}_2\text{O})$, of $(2.6\text{--}6.1) \times 10^{31} \text{ s}^{-1}$, which disagrees with $Q(\text{H}_2\text{O}) \approx 1 \times 10^{31} \text{ s}^{-1}$ determined by independent H₂O, OH, and H measurements. Furthermore, our own [O I] 6300 Å observations of the inner coma (< 30,000 km) using the 3.5 m Wisconsin-Indiana-Yale-NOAO telescope Hydra and Densapak multi-object spectrographs yield $Q(\text{H}_2\text{O}) \approx 1 \times 10^{31} \text{ s}^{-1}$. Using our [O I] 6300 Å data, which cover spatial scales ranging from 2,000 to 1×10^6 km, and a complementary set of wide-field ground-based OH images, we can constrain the sources of the apparent excess O(¹D) emission to the outer coma, where photodissociation of OH is assumed to be the dominant O(¹D) production mechanism. From production rates of other oxygen-bearing volatiles (e.g., CO and CO₂), we can account for at most 30% of the observed excess O(¹D) emission. Since even less O(¹D) should be coming from other sources (e.g., electron excitation of neutral O and distributed nonnuclear sources of H₂O), we hypothesize that the bulk of the excess O(¹D) is likely coming from photodissociating OH. Using the experimental OH photodissociation cross section of Nee & Lee at Ly α as a guide in modifying the theoretical OH cross sections of van Dishoeck & Dalgarno, we can account for $\approx 60\%$ of the observed O(¹D) excess without requiring major modifications to the other OH branching ratios or the total OH photodissociation lifetime.

Subject headings: comets: individual (Hale-Bopp 1995 O1, Hyakutake (C/1996 B2)) — instrumentation: spectrographs — molecular processes

1. INTRODUCTION

The release of water from the nucleus and its subsequent photochemical behavior drive much of the physical phenomena in cometary comae when comets approach within ~ 2 AU of the Sun. Thus, one of the first tasks in understanding any cometary system is to determine the water production rate, $Q(\text{H}_2\text{O})$.

Direct infrared emission from water has been detected (e.g., Mumma et al. 1996; Dello Russo et al. 2000), but traditionally, the more easily observed emissions from its daughter products (OH, H, and O) have been the primary means for determining $Q(\text{H}_2\text{O})$. We have observed [O I] 6300 Å emission from comets C/1973 E1 (Kohoutek; Huppler et al. 1975; Scherb 1981), 1P/1982 U1 (Halley;

Magee-Sauer et al. 1988, 1990; Smyth et al. 1993), C/1989 X1 (Austin; Schultz et al. 1992, 1993), C/1996 B2 (Hyakutake; J. P. Morgenthaler et al., in preparation), and C/1995 O1 (Hale-Bopp; this work) using Fabry-Pérot interferometers with resolving powers sufficient to separate the cometary [O I] line from the Earth's [O I] airglow line and nearby cometary NH₂ lines (e.g., Fig. 1). In general, we found good agreement between our results and others. Because [O I] 6300 Å emission is the result of a forbidden transition rather than fluorescence, if all these photons come from O(¹D) created during the photodissociation of H₂O and its daughter OH, $Q(\text{H}_2\text{O})$ can be derived from the O(¹D) production rate, $Q[\text{O}(\sup{1}D)]$, using the expression

$$Q(\text{H}_2\text{O}) = \frac{Q[\text{O}(\sup{1}D)]}{\text{BR1} + (\text{BR2})(\text{BR3})}, \quad (1)$$

where the BR n are the branching ratios of the H₂O photolysis reactions (e.g., Table 1). Using the H₂O + $\nu \rightarrow \text{H}_2$ + O(¹D) and H₂O + $\nu \rightarrow \text{OH} + \text{H}$ branching ratios (BR1 and BR2) found in Huebner, Keady, & Lyon (1992), and the OH + $\nu \rightarrow \text{O}(\sup{1}D) + \text{H}$ branching ratio (BR3) found in van Dishoeck & Dalgarno (1984), we derive $Q(\text{H}_2\text{O})$ values for Hale-Bopp that are a factor of 3–4 higher than those determined by other methods (§ 5.1). There is a wide range of H₂O branching ratio values found in the literature (e.g., Fink & Disanti 1990, BR1 = 0.082, BR2 = 0.89), but the difference between these can account for no more than 10% of the observed excess [O I]. Limiting our analysis to the [O I] 6300 Å data taken in the inner coma (< 30,000 km)

¹ Department of Physics, University of Wisconsin–Madison, Madison, WI 53706; jpmorgen@alum.mit.edu.

² Space Astronomy Laboratory, University of Wisconsin–Madison, Madison, WI 53706.

³ Visiting Astronomer at the National Solar Observatory, operated by the Association of Universities for Research in Astronomy, Inc., under contract to the National Science Foundation.

⁴ Department of Astronomy, University of Wisconsin–Madison, Madison, WI 53706.

⁵ NASA Goddard Space Flight Center, Greenbelt, MD 20771.

⁶ Raytheon ITSS, 4400 Forbes Boulevard, Lanham, MD 20706.

⁷ Now at Department of Astronomy, University of Wisconsin–Madison, Madison, WI 53706.

⁸ Department of Atmospheric, Oceanic, and Space Sciences, University of Michigan, Ann Arbor, MI 48109.

⁹ Fresh Pond Research Institute.

¹⁰ Atmospheric and Environmental Research, Inc.

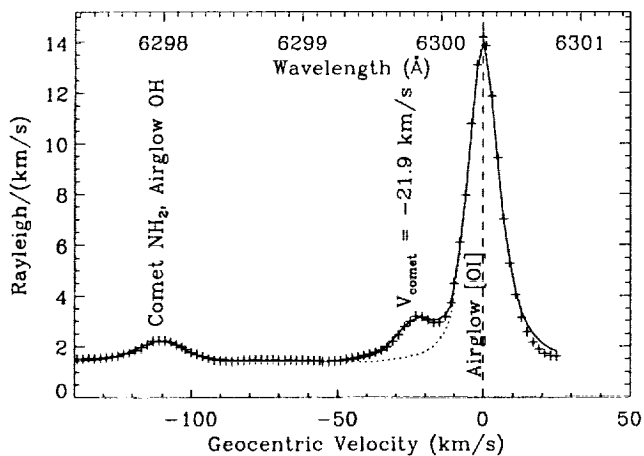


FIG. 1.—WHAM spectrum of Comet Hale-Bopp, from 1997 March 5. In this 30 s exposure, the WHAM emission-line sensitivity is less than 0.1 R. Solid line is a model with three Voigt profiles in emission plus seven Voigts in absorption representing the scattered solar spectrum. The dotted line is the same minus the cometary [O I] emission line. The wavelength of airglow [O I] line is 6300.304 Å.

where photodissociation of H_2O dominates the production of $\text{O}(^1D)$ and using the Huebner et al. (1992) H_2O branching ratios, we find $Q(\text{H}_2\text{O})$ values consistent with others (§ 5.2). Therefore, we consider mechanisms that can produce $\text{O}(^1D)$ at large cometocentric distances, such as photodissociation of CO and CO_2 . In § 6, we show that dissociation of CO and CO_2 can produce no more than $\approx 30\%$ of the observed $\text{O}(^1D)$ and that other sources, such as electron excitation of neutral oxygen or a distributed source of H_2O in the outer coma, are unlikely to contribute significantly. Therefore, we consider the possibility that the widely accepted $\text{OH} + \nu \rightarrow \text{O}(^1D) + \text{H}$ branching ratio of van Dishoeck & Dalgarno (1984) may be incorrect (§ 4).

2. OBSERVATIONS

Observations of comet Hale-Bopp over a wide range of wavelengths were conducted from 1996 August 16 through 1997 April 29. Here we consider [O I] 6300 Å observations between 1997 February 22 and April 21 that were recorded by four instruments on Kitt Peak: the Wisconsin $\text{H}\alpha$ Mapper (WHAM; Tuft 1997), two configurations of the 3.5 m Wisconsin-Indiana-Yale-NOAO (WIYN) telescope multiobject spectrograph (MOS), and a 50 mm dual-etalon

Fabry-Pérot spectrometer coupled to the National Solar Observatory McMath-Pierce main telescope. Table 2 summarizes the capabilities of each instrument and the number of nights each observed Hale-Bopp in [O I]. The combination of MOS and Fabry-Pérot data covers spatial scales ranging from 2000 to 1×10^6 km. Table 3 gives observational details and comet ephemeris data.

The WIYN MOS absolute calibration is based on spectroscopic observations of Vega. The WHAM and 50 mm Fabry-Pérot instrument calibrations are based on the $\text{H}\alpha$ surface brightness of NGC 7000 (the “North America Nebula”; coordinates $\alpha_{2000} = 20^{\text{h}}58^{\text{m}}4^{\text{s}}$, $\delta_{2000} = 44^{\circ}35'43''$). The average surface brightness of NGC 7000 was determined by Scherb (1981) to be 850 ± 50 rayleighs (R) over the central $49'$ of the nebula, where

$$1 \text{ R} = \frac{10^6}{4\pi} \text{ photons s}^{-1} \text{ cm}^{-2} \text{ sr}^{-1}. \quad (2)$$

The Scherb (1981) NGC 7000 calibration has been verified independently by several techniques. Using a comparison blackbody source, Nossal (1994, pp. 208–212) found the $\text{H}\alpha$ surface brightness of NGC 7000 to be 930 ± 80 R over a $49'$ field of view (FOV), which she took to be in agreement with Scherb (1981) because of the potential for systematic error in the estimation of parasitic light contributions in Fabry-Pérot measurements of continuum sources. Furthermore, decades of work on Galactic and geocoronal $\text{H}\alpha$ emissions have been based on the Scherb (1981) NGC 7000 calibration (e.g., Münch & Pitz 1989; Nossal et al. 1993; Reynolds 1997; Bishop et al. 2001).

We estimate the NGC 7000 $\text{H}\alpha$ surface brightness to be ≈ 800 R over the 1° WHAM FOV, rather than 850 R, determined by Scherb (1981) for a $49'$ FOV, because NGC 7000 is slightly peaked at the center of the calibration FOV (Ishida & Kawajiri 1968). By a similar argument, we estimate that the NGC 7000 surface brightness is 900 R over the $4'$ FOV of the 50 mm Fabry-Pérot. The WHAM sensitivity at [O I] 6300 Å was derived from measurements of the relative transmission of the [O I] and $\text{H}\alpha$ order separating filters and calculations of the transmissions of the other WHAM optical elements at [O I] and $\text{H}\alpha$. The resulting sensitivity ratio $T(6300)/T(6563)$ is 0.986 (Reynolds et al. 1998). The ratio of the transmissions of the $\text{H}\alpha$ and [O I] 6300 Å order separating filters used in the 50 mm Fabry-Pérot was 1.4. We estimated the atmospheric extinction at [O I] using WHAM measurements of NGC 7000 at $\text{H}\alpha$,

TABLE 1
PHOTODISSOCIATION BRANCHING RATIOS

Reaction	BR n	Quiet Sun	Active Sun	Reference ^a
$\text{H}_2\text{O} + h\nu \rightarrow \text{H}_2 + \text{O}(^1D)$	BR1	0.050	0.067	H
$\text{H}_2\text{O} + h\nu \rightarrow \text{H} + \text{OH}$	BR2	0.855	0.801	H
$\text{OH} + h\nu \rightarrow \text{H} + \text{O}(^1D)$	BR3	0.094	...	§ 4
$\text{OH} + h\nu \rightarrow \text{H} + \text{O}(^1D)$	BR3'	0.357	...	§ 4
$\text{OH} + h\nu \rightarrow \text{H} + \text{O}(^3P)$	BR4	0.662	0.513	V
$\text{OH} + h\nu \rightarrow \text{H} + \text{O}(^3P)$	BR4'	0.472	...	§ 4
$\text{CO}(X^1\Sigma^+) + h\nu \rightarrow \text{C}(^1D) + \text{O}(^1D)$	BR5	0.046	0.042	H
$\text{CO}(X^1\Sigma^+) + h\nu \rightarrow \text{C}(^1D) + \text{O}(^1D)$	BR5'	0.123	0.123	T
$\text{CO}_2 + h\nu \rightarrow \text{CO}(X^1\Sigma^+) + \text{O}(^1D)$	BR6	0.457	0.391	H

^a H, Huebner et al. 1992; V, van Dishoeck & Dalgarno 1984; § 4, selected values from Table 6 discussed in § 4; T, Tozzi, Feldman, & Festou 1998. The van Dishoeck & Dalgarno OH cross sections have been calculated for a heliocentric velocity of -14 km s^{-1} , appropriate for 1997 early March.

TABLE 2
INSTRUMENT CHARACTERISTICS

Name	Telescope	Bandpass (Å)	R ^a	FOV	Number of Nights
WHAM ^b	WHAM	6297–6301	30000	1°	3
Hydra MOS.....	WIYN	6100–6400	15000	45° ^c	3
Densepak MOS.....	WIYN	6100–6400	15000	28" × 52" ^d	1
50 mm FP ^b	McMath-Pierce	6100–6400	60000	4'	9

^a Resolving power $\lambda/\Delta\lambda$.

^b Dual-etalon Fabry-Pérot interferometer.

^c Ninety-six fibers, each with a 3" FOV arrayed in six concentric rings (see Fig. 3).

^d Hexagonal array of 91 3" fibers on 4" centers.

finding an extinction coefficient $K = 0.085$ mag per air mass.

3. DATA REDUCTION

3.1. WHAM Spectra

Our primary evidence of an unexpectedly high O(¹D) production rate in comet Hale-Bopp comes from WHAM spectroscopic observations. The spectra, one of which is shown in Figure 1, were taken with the 1° WHAM FOV centered on the head of the comet. Over such a wide FOV, the dominant feature is the airglow [O I] emission (~ 100 R).

The WHAM spectra (e.g., Fig. 1) were fit using a program called "Voigt-fit" developed by R. C. Woodward (University of Wisconsin). The program improves on the approximation of the Voigt profile and its derivative in Rybicki & Lightman (1979, p. 291) and Armstrong (1967). The program is capable of convolving an empirically determined instrument profile with a set of arbitrarily specified Voigt functions and up to a second-order continuum function. A nonlinear least-squares fitting algorithm finds the optimal parameters and estimates their statistical errors. We measured the instrument profile with the [O I] airglow

line and used a fit to a McMath-Pierce Fourier transform spectrometer data set from 1997 February 2 to constrain the solar continuum. Using the nominal WHAM [O I] calibration appropriate for diffuse sources, we find the surface brightness in the airglow and cometary [O I] lines listed in the third and fourth columns of Table 4.

Since the comet emission did not uniformly fill the WHAM 1° FOV, it is necessary to take into consideration the variation of WHAM sensitivity with position in the aperture. Figure 2 shows the normalized sensitivity as a function of position as measured with a neon 6304 Å line projected onto a diffusing screen in the instrument calibration apparatus. The instrument is more sensitive in the center than toward the edges of the FOV; thus, for a centrally concentrated source, such as the comet, the effective instrument sensitivity was higher than if the source uniformly filled the entire aperture. We calculate the increment to the instrument sensitivity for each night by multiplying the image in Figure 2 by the normalized comet image from each night (e.g., Fig. 3) and finding the average pixel value of the resulting image. These increments to the instrument sensitivity, shown in the fifth column of Table 4, are applied to the nightly average [O I] surface brightness values given in the sixth column.

TABLE 3
OBSERVATIONS

Date (UT)	Time ^a (UT)	Air Mass ^a	Instrument ^b	R_{helio}^c	Δ^c	Δ^d	P.A. ^e
1997 Feb 22	11:45/15:43	5.31/2.34	W	1.129	1.594	-30.2	326.3
1997 Feb 24	11:26/12:43	7.24/2.62	W	1.110	1.560	-29.1	327.0
1997 Mar 2	11:37/13:08	5.16/2.14	H96	1.055	1.467	-24.4	330.7
1997 Mar 5	11:55/12:58	4.16/2.35	W	1.029	1.427	-21.9	333.4
1997 Mar 9	12:15/12:25	3.49/3.33	FP	0.999	1.383	-17.6	338.2
1997 Mar 10.....	11:41/12:12	5.30/3.66	FP	0.992	1.373	-16.5	338.3
1997 Mar 16.....	12:16/12:58	4.21/2.88	H96	0.956	1.330	-8.42	349.6
1997 Mar 18.....	12:07/13:04	5.04/2.88	D	0.946	1.322	-5.66	353.6
1997 Apr 7.....	03:24/03:50	3.45/4.46	FP	0.920	1.408	19.6	37.8
1997 Apr 8.....	03:30/03:38	3.53/3.68	FP	0.923	1.420	20.5	39.7
1997 Apr 9.....	03:22/03:33	3.23/3.48	FP	0.925	1.431	21.3	42.4
1997 Apr 10.....	03:50/04:00	4.30/4.63	FP	0.928	1.444	21.2	44.1
1997 Apr 13.....	03:23/03:35	3.19/3.59	FP	0.939	1.484	24.3	49.1
1997 Apr 14.....	02:13/03:43	1.93/3.90	FP	0.943	1.497	25.0	51.2
1997 Apr 16.....	02:28/02:40	2.09/2.27	FP	0.952	1.526	26.1	44.1
1997 Apr 21.....	02:41/03:39	2.29/3.72	H96	0.981	1.604	27.9	61.9

^a Begin/end.

^b W = WHAM; H96 = Hydra, 96 fibers; FP = 50 mm Fabry-Pérot; D = Densepak.

^c In units of AU; R_{helio} is the distance between the Sun and the comet, Δ is the distance between the Earth and the comet.

^d In units of km s^{-1} .

^e Position angle of the anti-Sun vector, measured counterclockwise from the north celestial pole in degrees.

TABLE 4
WISCONSIN H α MAPPER COMET HALE-BOPP SURFACE BRIGHTNESS^a

Date (UT)	Time (UT)	Airglow ^b	I_{6300} ^{b,c}	IS ^d	[O I] Average ^{b,e}
1997 Feb 22.....	11:45	191	16.5 \pm 1.9	1.22	13.3 \pm 0.6
1997 Feb 22.....	12:46	129	16.1 \pm 1.0		
1997 Feb 22.....	15:43	172	16.1 \pm 0.6		
1997 Feb 24.....	11:26	97	19.3 \pm 1.8	1.26	15.1 \pm 1.2
1997 Feb 24.....	11:56	135	18.2 \pm 3.2		
1997 Feb 24.....	12:43	124	19.5 \pm 2.4		
1997 Mar 5.....	12:00	124	28.7 \pm 2.3	1.28	22.5 \pm 1.8

- ^a Averaged over a 60' FOV.
^b The $\lambda = 6300$ Å surface brightness in rayleighs.
^c Uncorrected for nonuniform FOV sensitivity; 1 σ errors.
^d Increment due to nonuniform FOV sensitivity.
^e Daily average, corrected for nonuniform FOV sensitivity.

3.2. WHAM Images

Narrowband images of Hale-Bopp in [O I] were recorded on the same nights as the WHAM spectra (Fig. 3). For the purposes of this work, we used the March 5 WHAM image shown in Figure 3 to aid with the reduction of the WHAM and 50 mm Fabry-Pérot spectroscopic data (§§ 3.1 and 3.4) and to construct radial profiles for comparison to the WIYN MOS data (§ 3.3) and model profiles. The profile of the tailward quadrant is plotted separately in Figure 7 as a thin solid line. About 13% of the total [O I] 6300 Å emission can be attributed to the tailward asymmetry seen in the [O I] image. This asymmetry is also seen in the OH image data of Harris et al. (2001) and may be related to the red wing seen in the [O I] spectral data (§ 3.4).

3.3. WIYN MOS

The WIYN MOS recorded up to 96 spectra simultaneously. A detailed description of the WIYN MOS reduction process used for Hale-Bopp can be found in

Anderson (1999) and Glinski & Anderson (2000). As discussed in § 2, the extinction coefficient used to reduce the WHAM data was 0.085 mag per air mass. The WIYN data were reduced using the Kitt Peak standard extinction value of 0.114 mag per air mass. Thus, at a typical comet air mass of 3.6, our WIYN surface brightnesses may be 10% higher than our WHAM values. Given a typical uncertainty of at least 20% in determining extinction corrections at high air masses, we ignore these differences.

The MOS spectra were fitted using IRAF with a flat continuum and Gaussian lines. The airglow and comet lines were resolved on all nights except March 16–18. On March 16 the comet [O I] flux in the fourth ring of Hydra fibers was only a few times the sky background. The flux values in the fifth and sixth rings on March 16 were identical to

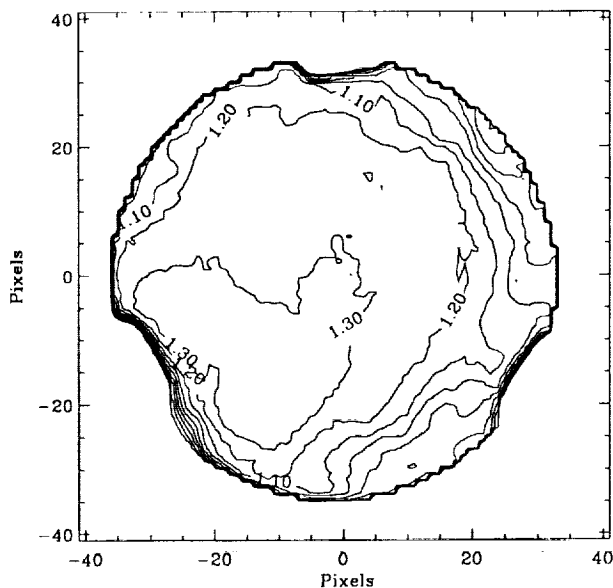


FIG. 2.—Normalized sensitivity of the 1° WHAM Fabry-Pérot FOV. Sensitivity falls off toward the edges as indicated by the contours, which are evenly spaced at intervals of 0.1. The lowest contour plotted is 0.5 and shows the outline of the spacers separating the etalons. Each pixel is 0.8, or $\approx 50,000$ km at $\Delta = 1.4$ AU.

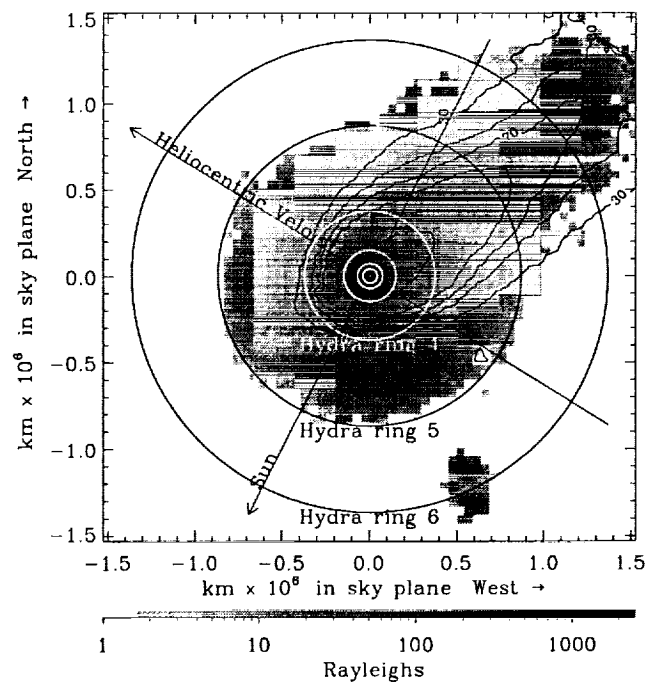


FIG. 3.—Hale-Bopp March 5 image with [O I] emission shown in gray scale, dust in contours, and circles showing positions of the Hydra annuli. The edge of the 1° WHAM FOV can be seen in the dust contours in the upper right-hand corner of the image. The angular radii of the Hydra rings are 0.67', 1.15', 2.4', 6', 14', and 22'.

within statistical errors; thus, their average value was taken to be the sky background and subtracted from the rest of the fibers. For the Densapak observations on March 18, the fibers were arrayed within 30" of the nucleus (30,000 km), and even a large airglow signal of several hundred rayleighs is negligible compared to the comet intensity of greater than 1×10^4 R (see Fig. 8).

3.4. 50 mm Fabry-Pérot

This instrument was operated in a ring-sum mode, similar to that of the WHAM spectral mode, in which the Fabry-Pérot spectral fringe pattern is imaged onto a CCD. The process of extracting spectra obtained with this instrument is described in detail by Oliveresen et al. (2001) and Doane (1999). The extraction process was difficult because the FOV of the McMath-Pierce main telescope was partially occulted by one of the auxiliary telescopes and the main mirror was considerably foreshortened because of Hale-Bopp's high declination. The extracted spectra were fitted with the "Voigt-fit" program described in § 3.1. A particularly good example of these spectra is shown in Figure 4. The extended red wing on the cometary [O I] line is seen in most of the 50 mm Fabry-Pérot spectra, but with a lower signal-to-noise ratio. The red wing is consistent with material flowing in the anti-Sunward direction at 5–10 km s⁻¹.

Like the WHAM, the 50 mm Fabry-Pérot did not have uniform sensitivity over its entire FOV. Instrument sensitivity variation was mapped by stepping the image of a star at regular intervals along the declination and right ascension axes. These data were interpolated using spline functions and normalized to create the image shown in Figure 5. From this we determine the effective FOV diameter to be 4'.

Since we do not have image data for all of the nights that 50 mm Fabry-Pérot data were taken, we use the March 5 WHAM data to estimate the increment to the sensitivity of the 50 mm instrument. Following the WHAM analyses, we multiply Figure 5 by the March 5 WHAM image and calculate the average pixel value of the resulting image. In this way, we find the increment to the 50 mm Fabry-Pérot sensitivity to be 1.5. The third column of Table 5 gives the sensitivity-corrected average [O I] surface brightness values, in rayleighs, over the 50 mm Fabry-Pérot FOV. The

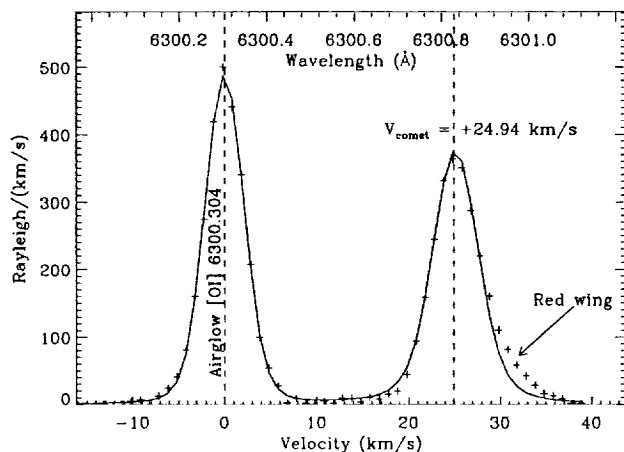


FIG. 4.—The 50 mm Fabry-Pérot spectrum of comet Hale-Bopp on 1997 April 14. The field of view is 200,000 km in radius, centered on the comet head.

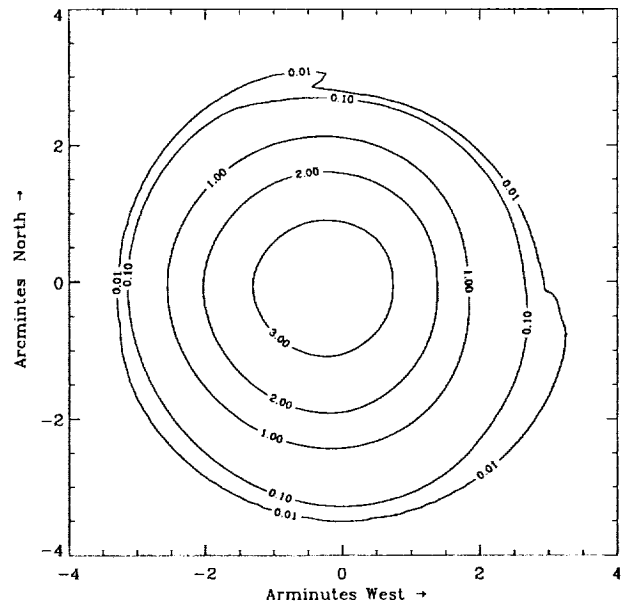


FIG. 5.—The 50 mm Fabry-Pérot field of view sensitivity map. Map is normalized so that average of the nonzero pixel values is 1.

scatter in the data, presumably due to the difficult spectral extraction process, is large (e.g., ~50% on April 7).

4. SOLAR PHOTODISSOCIATION OF H₂O AND OH

According to Keller (1976), Biermann & Trefftz (1964) were the first to discuss the importance of molecular photo-

TABLE 5
50 MILLIMETER FABRY-PÉROT SPECTROMETER
HALE-BOPP SURFACE BRIGHTNESS^a

Date (UT)	Time (UT)	$I_{6300}^{b,c}$
1997 Mar 9	12:20	2751 ± 171
1997 Mar 10	12:05	2417 ± 117
1997 Mar 10	12:12	2514 ± 135
1997 Apr 7	03:35	3896 ± 154
1997 Apr 7	03:40	4793 ± 171
1997 Apr 7	03:46	3663 ± 85
1997 Apr 7	03:50	3094 ± 179
1997 Apr 8	03:30	3416 ± 82
1997 Apr 8	03:34	3127 ± 70
1997 Apr 9	03:22	2977 ± 57
1997 Apr 9	03:27	3273 ± 60
1997 Apr 9	03:30	3275 ± 101
1997 Apr 10	03:50	1624 ± 45
1997 Apr 13	03:23	1543 ± 92
1997 Apr 13	03:30	1593 ± 88
1997 Apr 13	03:35	1857 ± 103
1997 Apr 14	02:19	1935 ± 48
1997 Apr 14	02:25	2257 ± 103
1997 Apr 14	03:38	1809 ± 73
1997 Apr 14	03:43	1654 ± 79
1997 Apr 16	02:28	2870 ± 104
1997 Apr 16	02:34	2554 ± 91
1997 Apr 16	02:40	2414 ± 79

^a Averaged over a 4' FOV.

^b The $\lambda = 6300$ Å surface brightness in rayleighs.

^c Corrected for nonuniform FOV sensitivity.

dissociation as the source of the forbidden [O I] lines at 5577, 6300, and 6364 Å. Collisional excitation into the $O(^1S)$ and $O(^1D)$ states from which these emissions occur is unlikely to be the dominant source because of the low density over most of the volume of most cometary comae. Therefore, Biermann & Treffitz proposed that the excited oxygen was the result of molecular dissociations. The most likely parent molecule was H_2O , which for some time had been assumed to be the major constituent of cometary nuclei (e.g., Delsemme & Swings 1952). Owing to the molecular source of [O I], Biermann & Treffitz correctly predicted that comets would also be bright in $Ly\alpha$. If H_2O was the major parent molecule, bright OH emissions were also implied. Early UV observations of comets confirmed these predictions (e.g., Code, Houck, & Lillie 1970, 1972). Water was unambiguously proven to be the major volatile component of comets by direct detection of water in comet Halley (e.g., Krankowsky et al. 1986; Mumma et al. 1986).

Using the molecular photochemistry known at the time (e.g., Potter & del Duca 1964; Jackson & Donn 1968), Bertaux, Blamont, & Festou (1973) considered several models of the observed $Ly\alpha$ spatial distribution in comets Bennett (C/1969 Y1) and 2P/Encke. They found that a reasonable fit to the data could be obtained using the thermal model of Mendis, Holzer, & Axford (1972) with an effective average H-atom outflow of 8 km s^{-1} . However, rather than a purely thermal distribution, Bertaux et al. preferred to construct a velocity distribution of H-atoms based on excess energies of photodissociations, which produced a similar overall result but which seemed more physically realistic. Bertaux et al. (1973) discuss in detail various excess energy states of H_2O photodissociation. Meier et al. (1976) used a similar velocity distribution to successfully fit comet C/1973 E1 Kohoutek $Ly\alpha$ data. High spectral resolution H α measurements have confirmed the predominance of the 8 km s^{-1} velocity component (e.g., Huppler et al. 1975; Smyth, Marconi, & Combi 1995b). One of the implications of the H-atom velocity distributions used by Bertaux et al. and Meier et al. is that OH photodissociation, which dominates the production of H-atoms in the outer coma, must produce mostly 8 km s^{-1} H-atoms, whereas most of the OH photodissociation reactions known at the time produced H-atoms with excess velocities of greater than 20 km s^{-1} . A predissociation reaction was therefore proposed in which ground state $OH(X^2\Pi)$ is excited to the $A^2\Sigma^+(v' = 2, N' = 1)$ or higher state by a solar photon in the wavelength range 2450–2640 Å and then spontaneously enters a repulsive state such as $^2\Sigma^-$ because of a potential crossing. The predissociation reaction produces $O(^1P)$ and imparts a velocity of 8–9 km s^{-1} to the hydrogen atom (Keller 1976). Schleicher & A'hearn (1982) calculated the heliocentric velocity dependence of OH predissociation in comets, which is caused by the relative shifting of superposition of photoabsorption features with absorption features in the near-UV solar spectrum. They later updated this calculation with improved oscillator strengths and solar spectral fluxes (Schleicher & A'Hearn 1988).

Keller (1976) notes that although the predissociation reaction can account for much of the total OH cross section, it alone is not sufficient to explain the total OH solar photodissociation lifetime. Van Dishoeck, Langhoff, & Dalgarno (1983) and van Dishoeck & Dalgarno (1983, 1984) suggested that far-UV photons in the wavelength range of 1200–1800 Å could also dissociate OH by absorp-

tion into a number of other electronic states, primarily $1^2\Sigma^+$, $1^2\Delta$, $B^2\Sigma^+$, and $2^2\Pi$ – $3^2\Pi$. The last three are dominated by absorption of solar $Ly\alpha$ photons and produce O atoms in the 1D and 1S states. They estimated the photoabsorption cross sections into these excited electronic states, combining them with the solar fluxes for typical solar minimum and maximum cases and the published predissociation rates of Schleicher & A'hearn (1982) to present a complete picture of dissociation of OH in comets. The total yield of $O(^1D)$ atoms is given by the combination of 1D and 1S branches, because O atoms produced in the 1S state first emit the green line at 5577 Å, leaving them in the 1D state, which then emits one of the red lines.

Laboratory measurements of the OH photoabsorption cross section by Nee & Lee (1984) were a factor of 2–3 larger than the values suggested by van Dishoeck & Dalgarno (1984) in the 1400–1800 Å region but up to 10 times larger near $Ly\alpha$. However, Nee & Lee noted there was a 60% uncertainty in their absolute calibration. When combined with the 20% uncertainty in the theoretical cross sections, they concluded that the theory and experiment were actually, but only barely, in formal agreement despite the large difference in the mean absolute values and their impact on estimating dissociation rates and branching ratios for OH in comets.

Huebner et al. (1992) provided total destruction rates and the various branching ratios for OH products for solar minimum and maximum conditions using both the theoretical and experimental sets of cross sections and incorporating the effect of photoionization. Their calculations were not based on the newer version of the OH predissociation rates by Schleicher & A'Hearn (1988). Because of the large calibration uncertainty in the experimental values and the very small value implied for the total OH photodissociation lifetime, which seems contradictory to many OH observations (Budzien, Festou, & Feldman 1994), Huebner et al. assigned a poor quality factor to their experimental version of OH photodestruction but a good one to the theoretical version.

It is clear that the solar $Ly\alpha$ flux is important in any assessment of OH photodissociation but especially for the $O(^1D)$ yield. Daily measures of the solar $Ly\alpha$ flux are available from the *Upper Atmosphere Research Satellite* SOLSTICE instrument throughout the Hale-Bopp apparition (Woods et al. 1996). None of the published calculations for OH destruction and $O(^1D)$ yield include up-to-date numbers for all of the relevant processes, and the question of the absolute value of the far-UV cross section, especially at $Ly\alpha$, still seems unresolved. We construct several scenarios for the modification of the OH photodissociation cross section based on the van Dishoeck & Dalgarno and Nee & Lee cross sections and updated predissociation rates and solar $Ly\alpha$ fluxes. The resulting OH + $v \rightarrow O(^1D)$ branching ratio (BR3), yield of 8 km s^{-1} H atoms (BR4), and OH lifetime (τ_{OH}) are summarized in Table 6 along with existing published values.

The first two rows of Table 6 show the BR3, BR4, and τ_{OH} values calculated by van Dishoeck & Dalgarno (1984) and by Huebner et al. (1992) using the van Dishoeck & Dalgarno (1984) cross sections but a slightly different solar spectrum. In the third row, labeled "VD + S88," we use the absolute cross sections of van Dishoeck & Dalgarno, the updated predissociation calculations of Schleicher & A'Hearn (1988), the OH photoionization rate given in

TABLE 6

QUIET-SUN OH PHOTODISSOCIATION CALCULATIONS

Reference ^a	BR3 ^b	BR4 ^c	τ_{OH}^d
VD	0.048	0.718	120
H/VD	0.094	0.662	134
VD + S88 (BR3)	0.066	0.686	123
VD + S88II	0.300	0.415	123
NL + VD	0.183	0.600	107
NL + VDII (BR3')	0.357	0.472	85
H/NL	0.390	0.453	50

^a VD, using van Dishoeck & Dalgarno 1984 theoretical OH cross sections; H/VD, treatment of VD cross sections by Huebner et al. 1992; VD + S88, VD updated for OH predissociation calculations of Schleicher & A'Hearn 1988 assuming $v_{\text{helio}} = 0 \text{ km s}^{-1}$ (these values are used as BR3 and BR4 in Table 1); VD + S88II, VD + S88 with BR4 at its 1 σ minimum and the resulting extra photons shifted to BR3; NL + VD, Nee & Lee 1984 experimental cross sections divided by 2.5 to match VD total cross section in the 1400–1800 Å region; NL + VDII, same as NL + VD, but NL cross section at Ly α is not scaled (these values are used as BR3' and BR4' in Table 1); H/NL, treatment of NL cross sections in Huebner et al. 1992.

^b OH + $h\nu \rightarrow \text{H} + \text{O}(^1D)$.

^c OH + $h\nu \rightarrow \text{H} + \text{O}(^3P)$.

^d OH lifetime in kiloseconds.

Huebner et al., and a solar Ly α flux of 3.0×10^{11} photons $\text{cm}^{-2} \text{ s}^{-1}$ (see Combi et al. 2000 for individual days throughout the period, corrected for the Sun's hemisphere as seen by the comet). This OH lifetime and yield of 8 km s^{-1} H atoms have been used successfully in a number of analyses of observations of the H coma that are sensitive to the H-atom velocity distribution (e.g., Combi & Smyth 1988; Combi et al. 1998, 2000).

Any calculation based on the complete set of Nee & Lee experimental cross sections produces total OH lifetimes that are too short to be compatible with cometary observations (e.g., last row in Table 6). Using the Nee & Lee cross sections, the greatest dissociation rate comes from the 1400–1800 Å region of the solar spectrum. Under the circumstances, it may be reasonable to consider that the van Dishoeck & Dalgarno (1984) cross section in this region are correct. Thus, for the case shown in row “NL + VD” of Table 6, we divide the experimental cross sections by a factor of 2.5, forcing them to agree with the 1400–1800 Å region in the van Dishoeck & Dalgarno calculation. Because the Nee & Lee cross section is much higher at Ly α , even after dividing by 2.5, the resulting cross section at Ly α is still somewhat higher than the van Dishoeck & Dalgarno value. The next case, row “NL + VDII,” is the same as the previous, except we use the actual Nee & Lee cross section at Ly α . This provides an upper bound to the O(¹D) yield at the expense of making the OH lifetime and yield of 8 km s^{-1} H atoms uncomfortably low. If we use the entire experimental cross section, we would likely obtain a result similar to the experimental version of Huebner et al. (row “H/NL”).

The “NL + VD” case, in which we force agreement of the Nee & Lee cross sections to the van Dishoeck & Dalgarno values in the 1400–1800 Å region, probably represents the smallest values for the OH lifetime and the yield of 8 km s^{-1} H atoms that are consistent with observations and model parameter tolerances for OH and H obser-

vations. A final consideration is to acknowledge that there is, after all, some uncertainty associated with the predissociation lifetime in the near-UV into the A² Σ^+ state (Schleicher & A'Hearn 1988). If that rate is reduced by its 20% uncertainty below its estimated mean value but the total OH lifetime is held fixed at the level set by the second case and all the extra rate is assigned to the Ly α branches (i.e., effectively giving more weight to the large experimental cross sections), the branching ratio for O(¹D) would increase to 0.30, and the yield of 8 km s^{-1} H atoms would decrease to 0.451 (row “VD + S88II” of Table 6). This would also require shifting a third of the population of 8 km s^{-1} H atoms to 20–24 km s^{-1} . Such a shift would be less of a problem, practically, for explaining observations of comet Hale-Bopp alone, because the large collision region implies that many fast H atoms would be collisionally thermalized to lower velocities anyway (Combi et al. 2000). However, there are earlier studies of comets with much smaller collisional regions, namely, Kohoutek (Meier et al. 1976; Combi & Smyth 1988) and Halley (McCoy et al. 1992; Smyth, Combi, & Stewart 1991), which are more sensitive to the presence of lower velocity H atoms, and those are not consistent with such a large reduction in the population of 8 km s^{-1} H atoms.

5. WATER PRODUCTION RATE

5.1. Large-Aperture Photometry

Using the WHAM spectroscopic measurements, we determine the average surface brightness, I_{6300} , of Hale-Bopp in the [O I] 6300 Å line for the dates listed in Table 4 over the WHAM FOV, $\Omega = 2.35 \times 10^{-4}$ sr. The total production rate of O(¹D) photons, $Q[\text{O}(^1D)]$, is then

$$Q[\text{O}(^1D)] = \left(\frac{4}{3}\right)(4\pi \Delta^2 \Omega I_{6300})AC, \quad (3)$$

where the factor of $\frac{4}{3}$ corrects for the emission in the 6364 Å decay path of O(¹D), which is outside of our bandpass, Δ is the distance between the Earth and the comet, and AC is the aperture correction.

As shown in Figure 3, the WHAM FOV was large enough so that AC is negligibly different than 1. For the 50 mm Fabry-Pérot spectrometer instrument, we calculate AC to be 2.25 by multiplying a normalized version of the March 5 WHAM [O I] image by the 50 mm instrument sensitivity map shown in Figure 5 and summing over all the nonzero pixels. In principle, the 50 mm Fabry-Pérot sensitivity and aperture corrections are functions of the water production rate and geocentric distance of Hale-Bopp. However, we ignore these effects since, as shown in Figure 6, over the time span in question, the water production rate of Hale-Bopp was relatively constant and the geocentric distance varied only $\sim 10\%$. The fourth column of the “W” and “FP” rows of Table 7 gives the WHAM and 50 mm Fabry-Pérot $Q[\text{O}(^1D)]$ values derived in this way.

In previous work, we derived $Q(\text{H}_2\text{O})$ assuming all O(¹D) was formed during the photodissociation of H₂O and its daughter OH (e.g., Magee-Sauer et al. 1990; Schultz et al. 1992; Smyth et al. 1995a). In this case, $Q(\text{H}_2\text{O})$ is given by equation (1). The fifth and sixth columns of Table 7 give $Q(\text{H}_2\text{O})$ derived in this way, where the fifth uses BR3 and the sixth uses BR3'. As shown by the open symbols in Figure 6, our $Q(\text{H}_2\text{O})$ values derived with BR3 are, on average, a factor of 3–4 higher than $Q(\text{H}_2\text{O})$ values derived by other methods (e.g., Dello Russo et al. 2000; Colom et al.

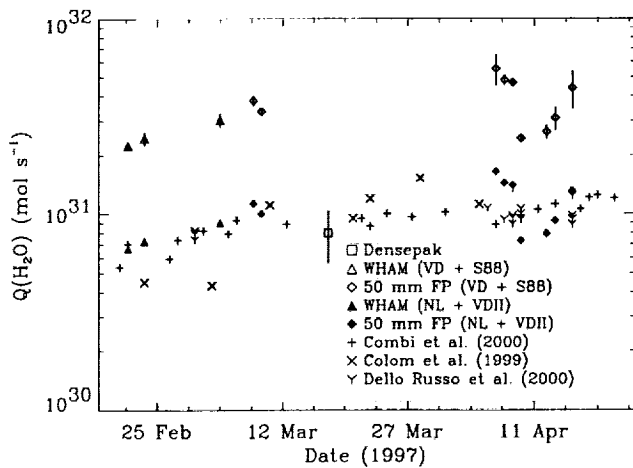


FIG. 6.—The $Q(\text{H}_2\text{O})$ values from various works. Open symbols denote production rates derived with eq. (1), using the modified van Dishoeck & Dalgarno (1984) $\text{OH} \rightarrow \text{O}(^1D)$ branching ratio, BR3 (denoted “VD + S88” in the figure). Filled symbols are the same but with the “NL + VDII” branching ratio (BR3’) discussed in § 4.

1999; Combi et al. 2000). The filled symbols in Figure 6 show that by using BR3’, we find $Q(\text{H}_2\text{O})$ values consistent with others. As discussed in § 4, BR3’ is likely too high, suggesting that another source of $[\text{O I}]$ 6300 Å may be present. After ruling out sources from the inner coma in § 5.2, we will consider possible contributions from the outer coma in § 6.

5.2. Inner Coma

We estimate $Q(\text{H}_2\text{O})$ from the MOS data by fitting a semiempirical model to radial profiles of the data. We start with a two-component Haser (1957) model since, as shown by the upper curve in Figure 7, this model fits the OH 3080

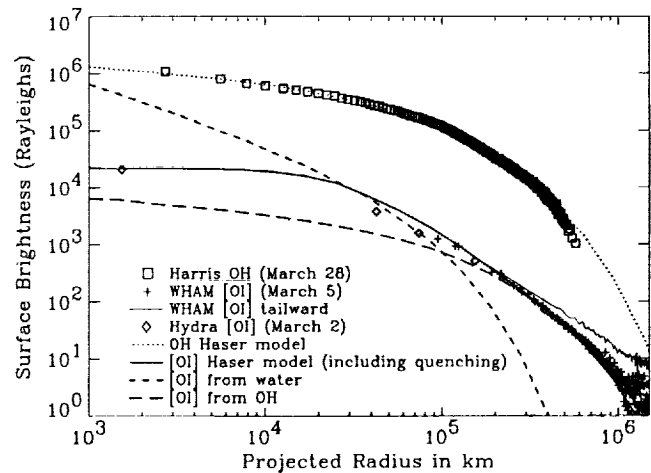


FIG. 7.—Measured and modeled radial profiles of $[\text{O I}]$ 6300 and OH 3080 emission in comet Hale-Bopp on March 2, March 5 ($[\text{O I}]$), and March 28 (OH). The WHAM profile indicated with the plus symbols is created from the three quadrants of Fig. 3 away from the tailward direction; Hydra points are averaged excluding this quadrant. The good agreement between the Hydra and WHAM radial profiles at greater than 1×10^5 km is our strongest evidence of the corroboration between these data sets.

Å data of Harris et al. (2001) over a wide range of spatial scales. Using the same H_2O and OH scale lengths (5.8×10^4 and 3.0×10^5 km, respectively), we can achieve a reasonable fit to our WHAM spatial data from March 5 and the outer two Hydra points from March 2, which cover distances greater than 1×10^5 km (Fig. 7, plus signs and diamonds). Not surprisingly, the production rate for this fit is very high, $Q(\text{H}_2\text{O}) = 50 \times 10^{30} \text{ s}^{-1}$.

For distances inside 1×10^5 km, where H_2O photodissociation is the dominant source of $\text{O}(^1D)$, the Haser model fitted to the outer coma overpredicts the amount of

TABLE 7
COMET HALE-BOPP $Q[\text{O}(^1D)]$ AND $Q(\text{H}_2\text{O})$ VALUES^a

Date (UT)	Instrument ^b	R_{\odot} ^c	$Q[\text{O}(^1D)]$ ^d	$Q(\text{H}_2\text{O})$ ^e	$Q'(\text{H}_2\text{O})$ ^f	Percent Error
1997 Feb 22	W	1.129	2.37	22.4	6.69	4.5 ^g
1997 Feb 24	W	1.110	2.58	24.4	7.28	7.8 ^g
1997 Mar 5	W	1.029	3.21	30.3	9.05	7.9 ^g
1997 Mar 9	FP	0.999	4.02	37.9	11.3	6.2 ^g
1997 Mar 10	FP	0.992	3.55	33.5	10.0	3.6 ^g
1997 Mar 18	D	0.946	...	8	...	30
1997 Apr 7	FP	0.920	5.85	55.2	16.5	18 ^h
1997 Apr 8	FP	0.923	5.12	48.3	14.4	6.2 ^h
1997 Apr 9	FP	0.925	4.97	46.9	14.0	4.5 ^h
1997 Apr 10	FP	0.928	2.59	24.4	7.3	2.7 ^g
1997 Apr 13	FP	0.939	2.80	26.4	7.9	8.3 ^h
1997 Apr 14	FP	0.943	3.28	30.9	9.2	13.4 ^h
1997 Apr 16	FP	0.952	4.65	43.9	13.1	21.7 ^h

^a These $Q(\text{H}_2\text{O})$ values are derived assuming that photodissociation of H_2O and its daughter OH are the only sources of $\text{O}(^1D)$.

^b W = WHAM; H96 = Hydra, 96 fibers; FP = 50 mm Fabry-Pérot; D = Densepak.

^c Hale-Bopp heliocentric distance in units of AU.

^d In units of 10^{30} s^{-1} , large-aperture case.

^e In units of 10^{30} s^{-1} . WHAM and 50 mm Fabry-Pérot results derived with eq. (1) and $\text{OH} \rightarrow \text{O}(^1D)$ branching ratio, BR3, from the “VD + S88” row of Table 6.

^f In units of 10^{30} s^{-1} . WHAM and 50 mm Fabry-Pérot results derived with eq. (1) and $\text{OH} \rightarrow \text{O}(^1D)$ branching ratio, BR3’, from the “NL + VDII” row of Table 6.

^g Formal 1σ errors from curve fit propagated through average.

^h Standard deviation of individual values.

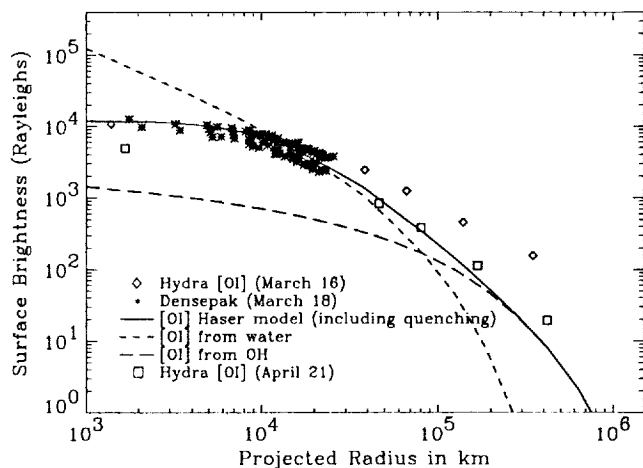


FIG. 8.—Measured and modeled radial profiles of [O I] 6300 emission in comet Hale-Bopp on March 16, March 18 (models indicated in solid and dashed lines), and April 21. Note the good agreement between the March 16 (Hydra) and March 18 (Densepak) data. We infer from this and Fig. 7 good agreement between WHAM and Densepak.

[O I]. Inside 10,000 km, the pure Haser model, shown as the short-dashed line in Figures 7 and 8, is a very poor predictor of the [O I] distribution. The fact that the OH distribution is well fitted in this area suggests that the underlying H₂O and OH populations are still reasonably well approximated by Haser distributions and that some effect is suppressing only the emission of [O I]. One likely candidate for this effect is collisional quenching of the metastable O(¹D) state, thought to be dominated by collisions with H₂O. Using the standard H₂O + O(¹D) → O(³P) quenching rate of $2.3 \times 10^{-10} \text{ cm}^3 \text{ s}^{-1}$ found in Streit et al. (1976), we could not achieve a good fit to the data inside 10,000 km. Another possible effect leading to the underproduction of [O I] in this region is suppressed photodissociation of H₂O due to the large Ly α opacity of Hale-Bopp's inner coma. For the purposes of our empirical model, we did not compute the Ly α opacity; rather, we increased the quenching rate until a good fit was obtained. For an FOV \geq 50,000 km, the total number of photons lost to this exaggerated quenching rate ($8 \times 10^{-10} \text{ cm}^3 \text{ s}^{-1}$) compared to an unquenched Haser model is negligible.

The solid-line fit to the Densepak points in Figure 8 (asterisks) is a two-component Haser model, including exaggerated quenching, with Haser scale lengths identical to those in Figure 7 but $Q(\text{H}_2\text{O}) = 8 \times 10^{30} \text{ s}^{-1}$, which is more consistent with $Q(\text{H}_2\text{O})$ values determined by other methods. Also shown in Figure 8 is Hydra data from March 16 and April 21. These data are consistent with $Q(\text{H}_2\text{O})$ values between those of Densepak and WHAM but are not well fitted by our Haser model; thus, we do not quote specific production rates for the Hydra data.

6. DISCUSSION

In § 5, we show that [O I] 6300 Å emission within $\sim 30,000$ km of the nucleus of comet Hale-Bopp is consistent with independent measurements of $Q(\text{H}_2\text{O})$. However, over the entire coma, we see 3–4 times as much [O I] 6300 Å emission as expected, given the standard model of H₂O and OH photochemistry. Although the greatest surface brightness of [O I] is found in the water-dominated nuclear region, by far the bulk of the [O I] photons come from the

(presumably) OH-dominated outer coma. Assuming the other $Q(\text{H}_2\text{O})$ measurements to be correct, we are led to one or both of the following possibilities: (1) there is a source of O(¹D) in the outer coma that is unknown or has been previously ignored or (2) there is an error in the standard model of OH photochemistry previously undetected by narrower FOV measurements.

To address possibility (1), we consider the contribution of CO and CO₂ to the total amount of O(¹D), since these are the most abundant oxygen-bearing volatiles after H₂O and OH. We find that it is unlikely that these species are providing more than a moderate fraction of the observed O(¹D) excess. Infrared measurements of CO₂ at 2.9 AU imply $Q(\text{CO}_2)/Q(\text{H}_2\text{O}) \approx 20\%$, which is likely an upper limit for $Q(\text{CO}_2)/Q(\text{H}_2\text{O})$ at 1 AU, because of the greater volatility of CO₂ (Crovisier et al. 1997). Weaver, Feldman, & McPhate (1994) measure a CO₂/H₂O ratio in comets P/Halley and 103P/Hartley 2 of 4%. Using the CO₂ → CO + O(¹D) branching ratio listed in Table 1, CO₂ could produce up to $\sim 25\%$ of the observed O(¹D) in comet Hale-Bopp. Radio measurements in early March imply $Q(\text{CO})/Q(\text{H}_2\text{O}) \approx 15\%$ (Biver et al. 1999). Using the larger of the CO → C + O(¹D) branching ratios listed in Table 1, this amount of CO contributes less than 5% of the total observed O(¹D) in comet Hale-Bopp. Thus, CO and CO₂ are unlikely to contribute more than 30% of the total O(¹D) in comet Hale-Bopp.

We also consider the possibility that ground-state oxygen is being excited by collisions with electrons. Evidence for such collisions at distances of up to 160,000 km is found in O I] 1356 Å emission detected by McPhate et al. (1999). However, one would expect that the effect of these collisions would be greater at smaller cometocentric distances, where densities are greater, rather than greater at the large distances, as we observe. Because of the complex dependence of the [O I] 6300 Å distribution on electron density and temperature, a quantitative treatment of this subject is beyond the scope of this work. Therefore, we cannot conclusively rule out this possibility. Also complicated by temperature and density effects are the processes of dissociative recombination and collisional dissociation. However, using our Haser models, ionization cross sections from Huebner et al. (1992), and dissociative recombination rates from Le Teuff, Millar, & Markwick (2000), we estimate that these effects contribute less than 1% of the total number of [O I] 6300 Å photons in comet Hale-Bopp.

Another possible source of O(¹D) in the outer coma is a distributed source of H₂O, perhaps coming from large particles ejected from the nucleus, not seen with other observing techniques. Since there is no evidence of clumps in the OH images of Harris et al. (2001) or other data reported to date, this material would have to be smoothly distributed. If this material is being continuously ejected from the nucleus, it would contribute to the flattening of the O(¹D) profile that we attributed to enhanced quenching in § 5.2. However, it is difficult to explain how this material could affect the O(¹D) distribution without also affecting the OH distribution. Because of the known problem with using the Haser formulation to model the inner coma, we defer to more sophisticated modeling efforts, such as those of Combi, Bos, & Smyth (1993), to conclusively determine the possible magnitude and nature of a distributed H₂O source in comet Hale-Bopp. Similarly, previously unidentified large oxygen-bearing molecules could deliver O(¹D) to the outer coma. However, if this mechanism were to be the primary source

of the excess $O(^1D)$ that we observe, the amount of oxygen delivered by these molecules would have to be on the same order with the amount of oxygen in all the H_2O released by Hale-Bopp.

The arguments above suggest that an unknown or previously ignored source of $O(^1D)$ in the outer coma of Hale-Bopp is probably not responsible for the bulk of the excess observed $[O\ I]$ 6300 Å emission and leave us with the possibility that there is an error in the standard model of OH photochemistry. This being the case, one might expect that the $O(^1D)$ excess would have been detected in previous comets. However, the 1° FOV of WHAM is the largest used to date, able to detect all the $[O\ I]$ emission from the comet. Aperture corrections for the previous, narrower FOV measurements were based on fits of models that used the standard numbers for H_2O and OH photodissociation. As seen in Figure 8, such a treatment would lead to a gross underprediction of the total amount of $O(^1D)$ in a comet if its wide-field $O(^1D)$ distribution were similar to that of Hale-Bopp. Preliminary analysis of data from comet Hyakutake (the only other comet observed with WHAM to date) shows excess $O(^1D)$ emission on days when the FOV was $\sim 1 \times 10^6$ km, but not on days when the FOV was a factor of 10 smaller. However, like Hale-Bopp, Hyakutake was an active comet, and one of the other mechanisms considered above, such as an extended source of H_2O in the outer coma, may be operating. A careful review of all of our past cometary data is planned in order to more fully address this question.

7. CONCLUSION

We have collected $[O\ I]$ 6300 Å data from comet Hale-Bopp with four different instruments: two Fabry-Pérot spectrometers (calibrated against NGC 7000) and two multiobject spectrographs (calibrated against Vega). Overlap in radial profiles of the MOSSs and narrowband images from one of the Fabry-Pérot instruments confirms good agreement between the calibrations. Limiting our analysis to the inner 30,000 km of the coma, where H_2O photodissociation likely dominates the production of

$O(^1D)$, we find a $Q(H_2O)$ value consistent with other observational results. In the outer coma, where $O(^1D)$ production is presumably dominated by OH photodissociation, we find a factor of 3–4 times more $O(^1D)$ than expected from standard OH photochemistry. Using the experimental OH photodissociation cross section of Nee & Lee (1984) at $Ly\alpha$, nearly all the excess $O(^1D)$ emission can be accounted for; however, the resulting yield of 8 km s^{-1} hydrogen atoms is uncomfortably low and the OH lifetime unacceptably short (case H/NL in Table 6). Using the Nee & Lee cross section only at $Ly\alpha$ and the widely accepted OH cross sections of van Dishoeck & Dalgarno (1984) everywhere else, $\sim 60\%$ of the observed $O(^1D)$ excess can be accounted for (case NL + VDII in Table 6). The remaining 30%–40% of the $[O\ I]$ photons may come from photodissociating CO and CO_2 , electron collisional excitation of ground-state oxygen, a distributed source of H_2O , and/or an as yet unknown source of $[O\ I]$ 6300 Å in the outer coma. The NL + VDII case results in a yield of $[O\ I]$ photons and 8 km s^{-1} hydrogen atoms that is consistent with observations, but an OH lifetime of 80,000 s that is somewhat shorter than the accepted solar-quiet value of 120,000 s (e.g., van Dishoeck & Dalgarno 1984; Budzien et al. 1994). Simultaneous spectral and spatial studies of H_2O , OH, $[O\ I]$, and H over a wide range of spatial scales are necessary to better constrain H_2O and OH photochemical constants using comet data. Conversely and perhaps more importantly, improved laboratory and theoretical photodissociation cross sections for H_2O and OH would lead immediately to a better understanding of the physics of cometary comae.

We would like to thank S. Tufte and L. M. Haffner for their help with data acquisition, M. Krok for conducting preliminary analysis on the Hyakutake data as part of her NASA SHARP-plus internship, J. McPhate for providing an electronic copy of Figure 1 of McPhate et al. (1999), and R. Reynolds, F. Roesler, and G. Ballester for valuable discussions. This work has been supported under NSF grant AST 96-15625, NASA grant NAG5-7952, and NASA contract NASW-97020.

REFERENCES

- Anderson, C. M. 1999, *Earth Moon Planets*, 78, 99
 Armstrong, B. H. 1967, *J. Quant. Spectrosc. Radiat. Transfer*, 7, 61
 Bertaux, J. L., Blamont, J. E., & Festou, M. 1973, *A&A*, 25, 415
 Biermann, L., & Trefitz, E. 1964, *Z. Astrophys.*, 59, 1
 Bishop, J., Harlander, J., Nossal, S., & Roesler, F. L. 2001, *J. Atmos. Sol.-Terr. Phys.*, 63, 341
 Biver, N., et al. 1999, *Earth Moon Planets*, 78, 5
 Budzien, S. A., Festou, M. C., & Feldman, P. D. 1994, *Icarus*, 107, 164
 Code, A. D., Houck, T. E., & Lillie, C. F. 1970, *IAU Circ.* 2201
 ———. 1972, in *Scientific Results from the Orbiting Astronomical Observatory (OAO-2)*, ed. A. D. Code (NASA SP-310), 109
 Colom, P., Gérard, E., Crovisier, J., & Bockelée-Morvan, D. 1999, *Earth Moon Planets*, 78, 37
 Combi, M. R., Bos, B., & Smyth, W. 1993, *ApJ*, 408, 668
 Combi, M. R., Brown, M. E., Feldman, P. D., Keller, H. U., Meier, R. R., & Smyth, W. H. 1998, *ApJ*, 494, 816
 Combi, M. R., Reinard, A. A., Bertaux, J., Quémerais, E., & Mäkinen, T. 2000, *Icarus*, 144, 191
 Combi, M. R., & Smyth, W. H. 1988, *ApJ*, 327, 1026
 Crovisier, J., Leech, K., Bockelée-Morvan, D., Brooke, T. Y., Hanner, M. S., Altieri, B., Keller, H. U., & Lellouch, E. 1997, *Science*, 275, 1904
 Dello Russo, N., DiSanti, M. J., Magee-Sauer, K., Novak, R., & Rettig, T. W. 2000, *Icarus*, 143, 324
 Delsemme, A. H., & Swings, P. 1952, *Ann. d'Astrophys.*, 15, 1
 Doane, N. E. 1999, B.S. thesis, Univ. Maryland
 Fink, U., & Disanti, M. A. 1990, *ApJ*, 364, 687
 Glinski, R. J., & Anderson, C. M. 2000, in 24th IAU Meeting, Joint Discussion 1, Vol. 1, *Atomic and Molecular Data for Astrophysics: New Developments, Case Studies and Future Needs* (Manchester: IAU), E69
 Harris, W. M., Morgenthaler, J., Mierkiewicz, E., Scherb, F., Oliverson, R., & Nordsieck, K. 2001, *ApJ*, submitted
 Haser, L. 1957, *Bull. Acad. R. Sci. Liège*, 43, 740
 Huebner, W. F., Keady, J. J., & Lyon, S. P. 1992, *Ap&SS*, 195, 1
 Huppler, D., Reynolds, R. J., Roesler, F. L., Scherb, F., & Trauger, J. 1975, *ApJ*, 202, 276
 Ishida, K., & Kawajiri, N. 1968, *PASJ*, 20, 95
 Jackson, W. M., & Donn, B. 1968, *Icarus*, 8, 270
 Keller, H. U. 1976, *Space Sci. Rev.*, 18, 641
 Krankowsky, D., et al. 1986, *Nature*, 321, 326
 Le Teuff, Y. H., Millar, T. J., & Markwick, A. J. 2000, *A&AS*, 146, 157
 Magee-Sauer, K., Roesler, F. L., Scherb, F., Harlander, J., & Oliverson, R. J. 1988, *Icarus*, 76, 89
 Magee-Sauer, K., Scherb, F., Roesler, F. K., & Harlander, J. 1990, *Icarus*, 84, 154
 McCoy, R. P., Meier, R. R., Keller, H. U., Opal, C. B., & Carruthers, G. R. 1992, *A&A*, 258, 555
 McPhate, J. B., Feldman, P. D., McCandliss, S. R., & Burgh, E. B. 1999, *ApJ*, 521, 920
 Meier, R. R., Opal, C. B., Page, T. L., Carruthers, G. R., & Keller, H. U. 1976, *A&A*, 52, 283
 Mendis, D. A., Holzer, T. E., & Axford, W. I. 1972, *Ap&SS*, 15, 313
 Mumma, M. J., DiSanti, M. A., Dello Russo, N., Fomenkova, M., Magee-Sauer, K., Kaminski, C. D., & Xie, D. X. 1996, *Science*, 272, 1310
 Mumma, M. J., Weaver, H. A., Larson, H. P., Williams, M., & Davis, D. S. 1986, *Science*, 232, 1523
 Münch, G., & Pitz, E. 1989, in *IAU Symp. 139, The Galactic and Extragalactic Background Radiation*, ed. S. Bowyer & C. Leinert (Dordrecht: Kluwer), 193

- Nee, J. B., & Lee, L. C. 1984, *J. Chem. Phys.*, 81, 31
- Nossal, S. 1994, Ph.D. thesis, Univ. Wisconsin-Madison
- Nossal, S., Reynolds, R. J., Roesler, F. L., Scherb, F., & Harlander, J. 1993, *J. Geophys. Res.*, 98, 3669
- Oliversen, R. J., Doane, N. E., Scherb, F., Harris, W. M., & Morgenthaler, J. P. 2001, *ApJ*, submitted
- Potter, A. E., & del Duca, B. 1964, *Icarus*, 3, 103
- Reynolds, R. J. 1997, *Science*, 277, 1446
- Reynolds, R. J., Hausen, N. R., Tufte, S. L., & Haffner, L. M. 1998, *ApJ*, 494, L99
- Rybicki, G. B., & Lightman, A. P. 1979, *Radiative Processes in Astrophysics* (New York: Wiley)
- Scherb, F. 1981, *ApJ*, 243, 644
- Schleicher, D. G., & A'hearn, M. F. 1982, *ApJ*, 258, 864
- . 1988, *ApJ*, 331, 1058
- Schultz, D., Li, G. S. H., Scherb, F., & Roesler, F. L. 1992, *Icarus*, 96, 190
- . 1993, *Icarus*, 101, 95
- Smyth, W. H., Combi, M. R., Roesler, F. L., & Scherb, F. 1995a, *ApJ*, 440, 349
- Smyth, W. H., Combi, M. R., & Stewart, A. I. F. 1991, *Science*, 253, 1008
- Smyth, W. H., Marconi, M. L., & Combi, M. R. 1995b, *Icarus*, 113, 119
- Smyth, W. H., Marconi, M. L., Scherb, F., & Roesler, F. 1993, *ApJ*, 413, 756
- Streit, G. E., Howard, C. J., Schmeltekopf, A. L., Davidson, J. A., & Schiff, H. I. 1976, *J. Chem. Phys.*, 65, 4761
- Tozzi, G. P., Feldman, P. D., & Festou, M. C. 1998, *A&A*, 330, 753
- Tufte, S. L. 1997, Ph.D. thesis, Univ. Wisconsin-Madison
- van Dishoeck, E. F., & Dalgarno, A. 1983, *J. Chem. Phys.*, 79, 873
- . 1984, *Icarus*, 59, 305
- van Dishoeck, E. F., Langhoff, S. R., & Dalgarno, A. 1983, *J. Chem. Phys.*, 78, 4552
- Weaver, H. A., Feldman, P. D., & McPhate, J. B. 1994, *ApJ*, 422, 374
- Woods, T. N., et al. 1996, *J. Geophys. Res.*, 101, 9541

Appendix B

Production, Outflow Velocity, and Radial Distribution of H₂O and OH in the Coma of Comet
C/1995 O1 [Hale-Bopp] from Wide Field Imaging of OH



Production, outflow velocity, and radial distribution of H₂O and OH in the coma of comet C/1995 O1 [Hale-Bopp] from wide field imaging of OH.

Walter M. Harris¹, Frank Scherb¹, Edwin Mierkiewicz¹, Ronald Oliverson², and Jeffrey Morgenthaler¹.

¹ University of Wisconsin-Madison; 1150 University Ave. Madison, WI 53706; 608-265-3436

² Goddard Space Flight Center

Abstract:

Observations of OH are a useful proxy of the water production rate ($Q_{\text{H}_2\text{O}}$) and outflow velocity (V_{out}) in comets. We use wide field images taken on 03/28/1997 and 04/08/1997 that capture the entire scale length of the OH coma of comet C/1995O1 (Hale-Bopp) to obtain $Q_{\text{H}_2\text{O}}$ from the model-independent method of aperture summation. We also extract the radial brightness profile of OH 3080 Å out to cometocentric distances of up to 10^6 km using an adaptive ring summation algorithm. Radial profiles are obtained as azimuthal averages and in quadrants covering different position angles relative to the comet-Sun line. These profiles are fit using both fixed and variable velocity 2-component spherical expansion models to determine V_{OH} with increasing distance from the nucleus. The OH coma of Hale-Bopp was more spatially extended than in previous comets, and this extension is best matched by a variable acceleration of H₂O and OH that acted across the entire coma, but was strongest within $1-2 \times 10^4$ km from the nucleus. This acceleration led to V_{OH} at 10^6 km that was 2-3 times greater than that obtained from a 1P/Halley-type comet at 1 AU, a result that is consistent with gas-kinetic models, extrapolation from previous observations of OH in comets with $Q_{\text{H}_2\text{O}} > 10^{29} \text{ s}^{-1}$, and radio measurements of the outer coma Hale-Bopp OH velocity profile. When the coma is broken down by quadrant, we find an azimuthal asymmetry in the radial distribution that is characterized by an increase in the spatial extent of OH in the region between the orbit-trailing and anti-sunward directions. Model fits to this area and comparison with radio OH measurements suggest greater acceleration in this region, with V_{OH} up to 1.5 times greater at 10^6 km radial distance than elsewhere in the coma.

1.0 Introduction:

The study of conditions in comet comae must necessarily begin with an understanding of water. As the dominant volatile component liberated from comet nuclei, the production rate, source geometry, temperature, outflow characteristics, solar wind interaction, and photochemical evolution of water sets the stage for much of the activity in the coma. Water has no visible or UV emission lines and is thus difficult to measure directly. While direct observations of cometary water are now performed over small fields of view in the IR (Dello Russo et al. 2000), historically, the most effective methods for deriving the characteristics of water over the entire coma have been from studies of its daughter products, H, O, and OH. The distribution and/or brightness of each daughter species may be used to derive water production, provided specific knowledge of an appropriate set of physical characteristics (e.g. formation rate, lifetime, outflow velocity, radial distribution, etc.) is available. The ancillary parameters will vary depending on the daughter species studied and are known to differing degrees of accuracy that depend on the solar radiation field, heliocentric velocity, and the total gas production from the comet. The interpretation of water production and evolution from a single measurement or species will therefore vary with the degree of uncertainty in the underlying assumptions (Schleicher, Millis, & Birch 1998). Fortunately the different aspects of water production are complementary and greatly improved convergence is obtained from coordinated observations (Combi et al. 2000).

This paper contains a detailed examination of the production rate, radial distribution, and velocity structure of OH in C/1995 O1 (Hale-Bopp) from wide-field images taken during a 2 week period bracketing its perihelion passage. Hale-Bopp was a unique object in the modern astronomical era, one that provided our best opportunity to date to study the physical properties of water production and evolution, and the effects of collisional processes in the coma at the extreme end of the gas production scale of comets. Because of the high level of Hale-Bopp's activity we could overcome several magnitudes of atmospheric attenuation and extract the radial distribution of OH out to distances $>10^6$ km from the nucleus. Over such a field of view (FOV), we imaged the entire scale length of OH, and could thus derive $Q_{\text{H}_2\text{O}}$ using only the $\text{H}_2\text{O} \rightarrow \text{OH}$ branching ratio, rather than relying on models of coma dynamics. The outer portion of the radial distribution is most sensitive to the outflow properties of OH, and so we fit the radial profiles with two types of spherical expansion models to determine the first order velocity structure of the coma as an azimuthal average and over position angle (PA) sectors relative to the comet-sun line. The model fits show evidence of acceleration over most of the coma that breaks down in regions characterized by a strong velocity gradient within a few $\times 10^4$ km of the nucleus and a slower process acting over greater distances. These results compare favorably with conclusions

derived from more detailed gas-kinetic models (Combi et al. 1997) and other complementary observations of OH (Colom et al. 1997; Woods, Feldman, & Rottman 2000) and other coma volatiles (Biver et al. 1997). We also report on the presence of an extended OH radial distribution in the trailing sectors of the coma that has also been seen in observations of metastable O (1D) (Morgenthaler et al. in press) and we provide a discussion of some possible mechanisms that could produce it.

2.0 Techniques for using OH as a Proxy for Q_{H_2O} and $V_{OH}(r)$:

OH is a good candidate for deriving Q_{H_2O} and other dynamical properties of the coma. It has only one significant formation pathway (H_2O), whereas the other water byproducts, O and H, may be both daughters *and* grand-daughters of H_2O , in addition to having multiple parents (in particular O may come in significant quantities from CO and CO_2). O and H emissions have other complicating characteristics, such as collisional quenching of O (1D) (Schultz et al. 1993) and Hydrogen's complex velocity structure (Smyth et al. 1993), large scale length, and interactions with solar wind and radiation field. By contrast, $\sim 90\%$ of OH is formed directly from H_2O into the $X^2 \text{ II}$ ground state (Budzien, Festou, & Feldman 1994; Van Dishoeck & Dalgarno 1984), which results in the brightest, highest contrast resonance fluorescence emission that is accessible from ground-based telescopes. The OH scale length against photodestruction is much shorter than for O or H (Huebner, Keady, & Lyon 1992), and it may thus be imaged in its entirety.

The OH life cycle in the comet follows three primary steps beginning with the photo-destruction of H_2O , followed by a radial expansion away from the nucleus, and ending with its dissociation or ionization. This chemical pathway ($H_2O \rightarrow OH \rightarrow O + H, OH^+$) has been studied extensively both theoretically and observationally (Budzien, et al. 1994; Schleicher & A'Hearn 1988; Van Dishoeck & Dalgarno 1984), and, while recent observations of O(1D) suggest that the dissociation branching ratios of OH to its daughters may need to be reviewed (Morgenthaler, et al. in press), the overall lifetime, state structure, and fluorescence efficiency of OH appear to be relatively well understood as functions of solar flux and heliocentric velocity. Because these various parameters all contain information about the evolution of water in the coma, to the extent that they are known, it is possible to invert the OH distribution to a map of water production either by fitting outflow models to the observed radial distribution or by adding all of the photons from the OH coma.

2.1 Q_{H_2O} from Aperture Summation:

If the angular extent of the coma is smaller than a telescope FOV, and the signal level of OH is great enough to overcome atmospheric extinction, one may sum all the photons in the

FOV and determine Q_{OH} (and thus Q_{H_2O}) with knowledge of only the g-factor, the lifetime against OH photo-dissociation, and the branching ratio from H_2O . With this technique Q_{H_2O} is derived from

$$1) Q_{OH} = N_{OH} \Omega \Delta^2 / \tau_{OH},$$

where Ω is the solid angle of the FOV, Δ is the geocentric distance, τ_{OH} is the photochemical lifetime of OH, and N_{OH} is the average column density over the field of view. The column density comes from the total signal in the aperture

$$2) N_{OH} = 10^6 I_{OH} / g,$$

where I_{OH} is the field-averaged brightness in rayleighs and the fluorescence efficiency, g , is adjusted for heliocentric Doppler shifts across the Solar Fraunhofer spectrum at 3080 Å (Schleicher & A'Hearn 1988). The conversion to Q_{H_2O} (Table 1) is made by dividing Q_{OH} by BR_{OH} , the branching ratio of water dissociation to OH (Table 2).

The principle advantage of aperture summation for the determination of Q_{H_2O} is that it does not require any specific knowledge of the structure of the coma, and is therefore not dependent on models of the radial distribution. Its primary disadvantage is that it provides only Q_{H_2O} , without any understanding of the characteristics of the coma.

2.2 Outflow Velocity:

Maps of the OH velocity and spatial distribution can be directly tied to the gas production and outflow characteristics of the coma as function of radial distance. The radial extent and velocity distribution depends on a combination of factors including Q_{H_2O} , solar UV radiation intensity, heliocentric velocity/distance, and collisional effects. When the field of view of a measurement is smaller than the radial extent of the OH coma, knowledge of the velocity is also required to invert the OH brightness distribution to Q_{H_2O} (Cochran & Schleicher 1993), because velocity and production are directly proportional in a spherically expanding flow.

The OH velocity distribution is the result of a convolution between the outflow characteristics of the parent H_2O molecules, the effect of any subsequent collisions of OH with coma constituents, and the excess energy of formation, which contributes a random velocity vector with a magnitude of 1.05 km/sec (Huebner, et al. 1992). The spatial extent of the OH coma is defined by the velocity distribution, the dimensions of the source region, the heliocentric distance of the comet, and the solar UV intensity. In most comets the velocity distribution of OH in the coma not known directly, and must be determined by fitting models to the radial shape of the coma or by assuming a uniform outflow velocity with a dependence on heliocentric distance (R_h) given by

$$3) V_{\text{OH}} = 0.85 R_{\text{h}}^{-2}$$

(Budzien, et al. 1994). Aside from the few *in situ* measurements (Lammerzahl et al. 1987) that serve as a basis for the above equation, wide-field, aperture-averaged measurements of the line profile of radio OH emissions (Bockelée-Morvan, Crovisier, & Gerard 1990; Colom, et al. 1997) are the only direct means we have for observing V_{OH} . Radio measurements generally validate the standard relation in an average sense for comets with $Q_{\text{H}_2\text{O}} < 10^{29} \text{ s}^{-1}$, but obtain higher velocities for more active comets (Bockelée-Morvan, et al. 1990). A major limitation of using radio OH line profiles for V_{OH} is that the emissions are strongly quenched (Schloerb 1988). The effect of this is to bias the extracted velocity to the outer coma, masking structure in the velocity distribution with cometocentric distance. This is not a concern for comets with a mostly ballistic coma, but it is a serious problem in active ($Q_{\text{H}_2\text{O}} > 10^{30} \text{ s}^{-1}$) comets like Hale-Bopp, where photolytic heating (see section 2.3 below) acts to raise the temperature of the gas and increase the bulk outflow velocity with increasing distance from the nucleus. In the absence of any physical data on the velocity distribution, the OH radial distribution must be blindly matched with models that track the evolution of water in the coma (Combi & Smyth 1988a; Combi & Smyth 1988b; Hodges 1990).

Fitting velocities to the OH radial distribution while assuming the lifetime-related parameters are known is a primary method for determining V_{OH} . This can be done in a variety of ways, ranging from variable width aperture photometry (Colom, et al. 1997; Schleicher, et al. 1998) to sophisticated hydrodynamic (Crifo 1995) or Monte-Carlo simulations (e.g. Hodges 1990; Combi and Smyth 1988a,b). The extent to which these techniques produce unique results is determined by the accuracy with which $Q_{\text{H}_2\text{O}}$ is known and the radial distance out to which the OH brightness has been measured. It is the outermost regions of the coma that are most sensitive to V_{OH} (Cochran & Schleicher 1993). When distances less than the OH scale length are sampled, spherical expansion models will produce a ‘family’ of velocity fits that are all of equal quality, but indicate different values of $Q_{\text{H}_2\text{O}}$. The range of acceptable velocities and hence the convergence of model fits of V_{OH} improves with the increasing radial extent of the sampled profile. A combination of radial maps of the OH distribution and wide field summations of the OH velocity profile (Colom, et al. 1997) further constrain the outer coma velocity and indicate the extent and magnitude of acceleration in the inner coma.

2.3 The Collision Zone:

Hale-Bopp is an extreme example of a comet where collisional acceleration acts across a spatially resolved region of the coma, affecting the interpretation of both OH radial profiles and outer coma velocity measurements. Where collisions dominate, the characteristics of the flow

will be modified toward a thermalized average of *all* species (parent, daughter, ion, electron, dust, etc.) that are present. Energy input will come from daughter velocity excesses resulting from photo-dissociation (dominated by fast H atoms) and ionization as the gasses traverse the collision zone, a process that is similar to photolytic heating in planetary upper atmospheres. It is possible to estimate the size of the collision zone by adopting the simplifying assumption of a spherically symmetric expanding coma with negligible dust mass loading. From this a simple formula (Whipple & Huebner 1976) for the collision zone radius (r_c) is

$$4) \quad r_c = \sigma Q_{\text{TOT}} / 4 \pi V,$$

where σ is the mean molecular cross section for ballistic collisions, Q_{TOT} is the total gas production rate of the comet (dominated by H_2O), and V is the mean outflow velocity of the background gas. The transition from a thermalized distribution to ballistic flow is a gradual, extending over distances greater than r_c . Models of the 1P/Halley velocity structure (Hodges 1990) showed that, while the flow was largely ballistic by 6×10^4 km from the nucleus, there was residual collisional heating out to $> 2 \times 10^5$ km.

The relevance of equation 4 depends on the amount of gas production. For weak to moderately active comets at 1 AU with $Q_{\text{H}_2\text{O}} \leq 10^{29} \text{ s}^{-1}$, $V_{\text{H}_2\text{O}} = 0.87 \text{ km-s}^{-1}$ (Budzien et al., 1994), and $\sigma \sim 3 \times 10^{-15} \text{ cm}^2$, the size of the collision zone is of order 1000 km or less at 1 AU. This is smaller than the scale lengths of most coma species and limits the effect of photolytic heating in the coma. Such a collision zone will also be unresolved for most observations, which means that any acceleration that occurs within it will be detectable only as an increase in the uniform bulk flow that becomes larger along with the gas production rate.

For very active comets with $Q_{\text{H}_2\text{O}} \geq 10^{30} \text{ s}^{-1}$, the collision sphere will be resolvable and begin to approach the dimensions of the scale lengths of H_2O and OH, which means that a significant fraction of all water photochemistry will occur in a collisionally thick medium. Both models (Combi, et al. 1997; Combi & Smyth 1988b; Hodges 1990) and observations (Bockelée-Morvan et al., 1990) show that this results in a significantly hotter coma that flows more rapidly away from the nucleus. Several estimates of $Q_{\text{H}_2\text{O}}$ obtained using different methods (Colom, et al. 1997; Combi, et al. 2000; Woods, et al. 2000) converge to values near 10^{31} s^{-1} for Hale-Bopp at perihelion, which corresponds to $r_c > 3 \times 10^5$ km, assuming $V \sim 1 \text{ km s}^{-1}$. This distance exceeds the scale length of water and several other coma species (both parent and daughter) at 1 AU, and the resulting increase in energy deposition modifies the magnitude and the spatial evolution of the outflow velocity, the excess velocity distributions of the daughter species, and the temperature of the gas.

3.0 Observations of OH:

The OH observations of Hale-Bopp were taken using the Burrell Schmidt Telescope, which was operated in 1997 by the Kitt Peak National Observatory (KPNO) and Case Western Reserve University. The Burrell is a 0.9 m Schmidt Cassegrain with a UBK7 corrector that provides system sensitivity down to 3050 Å. For Hale-Bopp the telescope was fitted with a KPNO SITE 2048 x 2048 CCD camera covering a 78.9' FOV. Observations of OH were obtained as part of two runs (March 24-29; April 8) that bracketed perihelion. The Burrell FOV exceeded 10^7 km for Hale-Bopp over this period, a radial extent roughly two orders of magnitude greater than the OH scale length in a Halley-class or weaker comet. The images were taken using the OH filter of the Hale-Bopp comet library (Farnham, Schleicher, & A'Hearn 2000) in single binning mode. The observations are summarized in Table 1.

3.1 Calibration and Correction for Atmospheric Attenuation:

Atmospheric attenuation was the most serious calibration issue for OH 3080 Å imaging (Farnham, et al. 2000). The already strong function of OH opacity to airmass was exacerbated by the low elevation of Hale-Bopp on most nights during this period. The comet began each night at its maximum elevation, which, over our time frame, ranged between 30° and 21° or 2-3.5 airmasses (Table 1), and set within 4 hours. OH images were taken on each night, but the most useful data were obtained on March 28 and April 8, 1997, when setup, acquisition and focus were procedurally perfect, and where OH was the immediate priority for observation. The data from April 8 is of higher quality due mainly to the smaller airmass. There were no standard stars bright enough at 3080 Å to be detected in the FOV of the comet images, so we obtained a series of observations of α Aur cover the same range of elevation angles to use as a flux standard. The stellar images were calibrated with IUE spectra at 3100 Å and used to derive a relationship between airmass and attenuation. We interpolated between the images to the corrections at the comet elevations, and assign a conservative ~15% accuracy in comet OH intensities.

3.2. Q_{H_2O} From Aperture Summation:

In the full-aperture summation extraction, the flat-fielded, bias and dark subtracted images were converted to a series of concentric variable diameter apertures centered on the comet nucleus. The total flux was co-added until increasing the area of the aperture failed to improve the signal to noise of I_{OH} and a comparison with the ring summing results indicated that the scale length had been reached. The total ADU were converted to rayleighs, and from then to N_{OH} and Q_{H_2O} using equations 1 and 2 above.

3.3. Ring Summation and the OH Radial Brightness Distribution:

Extraction of the OH spatial distribution was performed using a dynamic ring summing algorithm that operated by extracting all pixels over a range of radial distance and position angle, filtering for salt and pepper noise, and then coadding to obtain an average. Radial profiles of OH distribution were constructed by coadding annuli centered on the nucleus, with the annulus width in pixels set to the smallest value that maintained $s/n > 4$, up to a maximum of 75 pixels or 1.75×10^5 km. Full azimuthal coma averages and sub-arcs 90° and 30° in extent were extracted using this method. The ADU/ring averages were again converted to rayleighs based on the α Aur calibration.

4.0 Results:

4.1 Q_{H_2O} from Aperture Summation of I_{OH} :

Following the conversion of ADU to rayleighs, we obtain $Q_{OH} = 7.9 (\pm 1.2) \times 10^{30} \text{ s}^{-1}$ on 03/28 and $9.17 (\pm 1.4) \times 10^{30} \text{ s}^{-1}$ on 04/08 using the aperture summation method. With $BR_{OH} = 0.86$ (Table 2, (Huebner, et al. 1992)), this corresponds to $Q_{H_2O} = 9.31 (\pm 1.4) \times 10^{30} \text{ s}^{-1}$ and $10.8 (\pm 1.6) \times 10^{30} \text{ s}^{-1}$ on the two dates respectively (Table 1). These values compare favorably with other measurements of Q_{OH} made over the same period using a similar technique (Woods, et al. 2000).

4.2 Ring Summation Azimuthal Average:

The coma-averaged OH surface brightness distributions show evidence of substantial acceleration both from the spatial extent of the emission and the profile gradient inside 10^4 km. Figure 1 compares the measured OH radial profile on 8 April with a simple 2-component Haser simulation based on the 0.89 km/s spherical outflow derived from 1P/Halley and other comets at a heliocentric distance of 1 AU (Budzien, et al. 1994; Lammerzahl, et al. 1987). It is possible to scale the model to fit the observed profile out to a distance of $\sim 1-2 \times 10^5$ km and derive a water production rate of $Q_{H_2O} \sim 6 \times 10^{30} \text{ s}^{-1}$. However, the model fails on larger spatial scales as the scaled fit falls off while the OH distribution continues outward. Indeed, there is no scale factor that will allow a Halley-like flow to describe the outer regions of Hale-Bopp's OH coma, nor one that will match the inner coma radial distribution and provide Q_{OH} equivalent to that obtained from aperture summation in the same image. A higher outflow velocity is required to fit the extended part of the profile (see below), and, since $Q_{H_2O} \propto v/e^{(-r/v)}$, a higher production rate is indicated as well.

4.3 Ring Summation by Quadrant:

To look for azimuthal structure and asymmetries in gas production and radial extent of the emission we divided the coma into four 90° sectors of position angle (PA). We chose quadrant dimensions approximately centered on the comet-Sun line to allow comparison of day vs. night side gas production. The PA of the anti-Sun vectors on March 28 and April 8 are given in table 1. Due to the favorable viewing geometry near perihelion, the PA of the orbital velocity vector was well separated from the anti-Sun vector, which meant that the dust tail and anti-tail directions could also be isolated into separate quadrants, giving us four distinct coma environments for comparison.

The individual quadrants show significant differences in the spatial extent of the emission and shape of the profiles. This is consistent with a sun-comet angle/orbital phase dependence in the acceleration (Figure 2a,b). Moving radially outward in the sunward and anti-tail (orbit leading) quadrants, the OH surface brightnesses are greater than in the anti-sun and tailward (orbit trailing) quadrants out to $\sim 10^5$ km from the nucleus. Beyond this point the leading quadrant profiles begin to steepen and become progressively weaker relative to the trailing direction, with the profile in the sunward direction always the least spatially extended. The magnitude of the difference in spatial extension varied between the observations, however the leading/trailing profile asymmetry was a consistent feature on both dates studied, and does not appear related to the effects of short term $Q_{\text{H}_2\text{O}}$ variability. Assuming a uniform gas source distribution, the differences between the quadrant radial distributions are indicative of less acceleration occurring in the leading quadrants.

To get at the detailed structure of the spatial extension in the trailing direction we divided these quadrants into 30° sub-sector profiles. The sub-sectors show that the majority of the spatial extension can be isolated to an $\sim 60^\circ$ PA range centered slightly anti-sunward of the dust tail and extending into the region between the dust and ion tails (Figure 2c,d). The enhancements themselves were not tightly confined, but extended into the adjacent sub-sectors with the amount of extension diminishing away from the peak back to the levels seen in the leading quadrants. The most extended sub-sectors appear to contribute most of the extended emission in the quadrants where they are present, and, more significantly, appear to dominate the spatial extent of the azimuthally averaged radial profile. While the position angle of the peak in extension does vary slightly between these dates, the basic morphology of the spatial asymmetry extension and its effect on adjacent sub-sectors did not. The location and extension of the enhanced regions are also consistent with a similar feature reported in wide field O (^1D) images taken three weeks prior to our observations (Morgenthaler, et al. in press).

5.0 Coma Simulation Techniques:

The azimuthally averaged and sector OH radial distributions were fit using different forms of a 2-component Haser model (Haser 1957; Krishna Swamy 1997). We employ the Haser approach over the typically more accurate vectorial model (Festou 1981a), because the latter assumes a daughter product velocity distribution resulting from photodissociation in the purely ballistic case, a condition that did not hold over most of the scale length of the H₂O parent in Hale-Bopp. Spherical expansion models are not physically accurate. They do not address extended source (icy grain) regions, azimuthal asymmetries, or temporal variations in gas production, but they nevertheless have proven useful for estimating outflow velocities and gas production rates when applied outside of the collisionally thick coma. They are also computationally simple, which lets us quickly sample a broad range of input parameters to fit data. Our limited aims in using such models here are to determine that acceleration is occurring over a significant extent of the coma of Hale-Bopp, to compare our results with more sophisticated models and other observations, and to define the range of initial and final outflow velocities and production rates that describe the observed OH distribution.

We use two types of outflow approximations. In the first case, both $V_{\text{H}_2\text{O}}$ and V_{OH} are held fixed throughout the coma, but may vary independently of one another. In the second, we simulate collisional mixing and acceleration by forcing $V_{\text{H}_2\text{O}} = V_{\text{OH}}$ while allowing the combined flow to increase with cometocentric distance. The other physical parameters that describe H₂O/OH photochemistry and fluorescence, including g-factors and lifetimes (Table 2), are set to the appropriate solar cycle, heliocentric distance, and Swings effect values found in the literature (Budzien, et al. 1994; Schleicher & A'Hearn 1988). Each velocity simulation consists of the different runs of the model over three different spatial scales in the coma, $r < 10^5$ km, $10^5 \leq r < 10^6$, and the full profile out to 10^6 km. The model profiles are then fit to the data to obtain a point by point least squares difference that is then co-added for each of three sub-sections. An overall fit quality index for each case is derived from the product of the three summed differences. By merging the fits on different spatial scales we were able to screen out velocity combinations that fit large regions of the profile very well, but were obviously wrong at the extremes. This was particularly important for the profile at large radial distances.

5.1 The Fixed Model:

We use the classical form of a fixed velocity 2-component Haser model (Krishna Swamy 1997) where the parent and daughter velocities are fixed as a function of radial distance, but may be different from one another with restriction that $V_{\text{OH}} \geq V_{\text{H}_2\text{O}}$. For weaker comets, V_{OH} is roughly equal to $V_{\text{H}_2\text{O}}$, differing only by the convolution of V_{OH} with the 1.05 km-s⁻¹ excess velocity of H₂O dissociation (e.g. Festou, 1981a). The usefulness of the fixed model is that

when V_{OH} and V_{H_2O} differ by more than the excess velocity, it indicates the presence of acceleration in the coma, with the magnitude of the velocity ratio indicating the steepness of the velocity gradient. On the negative side, when there is acceleration over a spatially resolvable area of the coma, the fixed velocity flow model is an unphysical approximation of conditions, because it treats the velocity gradient only as a difference between V_{OH} and V_{H_2O} . Such a condition exaggerates the difference in initial and final velocities, since collisions will drive both H_2O and OH to a single radial velocity throughout the inner coma, while the model must assume that H_2O is always slow and OH is always fast. This requirement leads to contradictory model requirements, and errors in the fit. V_{H_2O} must be small to offset the high V_{OH} in the inner coma, but this prevents H_2O from reaching the outer coma where it can produce OH . With a minimal source of outer coma H_2O , the model responds by increasing Q_{H_2O} and V_{OH} to make up the difference.

This model was used for a range of velocities from 0.25 to 5.0 km-s⁻¹ to obtain sets of local minima of fit index vs. V_{OH} for a given V_{H_2O} in both the coma averaged case and the four quadrants. The full set of minima values were further winnowed by stepping through V_{H_2O} to find lowest fit indices over all of velocity space. A comparison with Q_{OH} implied by the model vs. aperture summation was used as an external validity check, but not as a fitting criterion. The best runs all match the observed profiles closely (Figure 3a), including the spatially extended sectors (Table 3). The utility of measuring the distribution out to a large radial distance is reflected in the convergence of the results. The fit families of the velocity and production rates vary only within 10%, which is better than our photometric accuracy. However, despite the quality of the fits, our results underscore the limitations of using a fixed model for an accelerating coma. The most obvious manifestation of this is the failure of the model to provide Q_{H_2O} consistent with aperture summation or an outer coma V_{OH} similar to those directly measured by Colom et al., (1997). The calibrated fits to the spherically averaged brightness profiles yield $Q_{H_2O} \sim 30\text{-}50\%$ higher than from the aperture method or other estimates (Combi, et al. 2000; Woods, et al. 2000), and $V_{OH} \sim 50\text{-}100\%$ higher than in direct measurements by Colom et al. (1997). In the case of the more extended trailing sectors, these differences become even more exaggerated.

We take the fact that the best matches to the data were invariably those with a substantial velocity difference between V_{OH} and V_{H_2O} as evidence for significant acceleration in the coma. Figure 4 shows the relationship between V_{OH} and V_{H_2O} . We note that even when a uniform ($V_{OH} = V_{H_2O}$) outflow can be fit to the full radial profile, it does not match the shape very well. Indeed, the best uniform outflow cases produce higher fit indices than the minima for all other velocity ratios and are more than 100x larger than the best mixed velocity ($V_{OH} \neq V_{H_2O}$) case.

The clear inference from this is that acceleration was occurring over a large region of the coma of Hale-Bopp rather than in a small, unresolved area near the nucleus. Furthermore, if we assume a uniform flow and thus take the weighted average velocity (V_{AV}) of the combined parent-daughter distribution in the model fits as

$$4) \quad V_{AV} = (N_{OH} * V_{OH} + N_{H_2O} * V_{H_2O}) / (N_{OH} + N_{H_2O}),$$

where N_{OH} and N_{H_2O} are the column densities of these species, we obtain radial velocity profiles showing a strong inner coma velocity gradient that diminishes beyond the water scale length and is similar to theoretical predictions.

5.2 Simulations of Variable Velocity Expansion:

An improvement in the physical accuracy of the model profiles may be achieved by adopting a single parent-daughter velocity that changes with cometocentric distance; i.e. an accelerating flow. Accelerating spherical expansion models (Hu 1990) are typically avoided, because the acceleration regions of most comets are confined to the unresolved extreme inner coma, and because the Haser approach offers no insight into the nature of the acceleration or how to address it. To avoid taking an entirely ad hoc approach to this problem, we draw from the basic elements of the more detailed 1-D dusty-gas simulations of Combi et al. (1997) as a starting point for developing a simple variable velocity spherical expansion model. Their approach has the coma effectively breaking down into two acceleration regions. Close to the nucleus, fast H atoms formed by H_2O and OH dissociation are re-thermalized into the bulk flow. This leads to a substantial acceleration out to the cometocentric distance where H collisionally decouples from the background gas, a location that is defined by the total gas production rate and heliocentric distance. Past this point the primary sources of acceleration are a diminishing collisional component and a passive filtering of the thermal distribution where the slower OH molecules are photodissociated closer to the nucleus than the faster ones, thus leaving a progressively higher velocity remnant with increasing distance. The collisional and passive acceleration zones are approximated in our simulations with different linear velocity gradients on either side of a contact radius. $V_{OH} = V_{H_2O}$ at all locations in this model, with the initial velocity, velocity gradients, and the location of the H contact radius serving as input variables. We don't include the excess velocity of OH formation from H_2O in our calculations because it is a non-radial velocity component, we have no information on how the excess is affected by collisions, and because the actual outflow velocity of Hale-Bopp was considerably higher than 1.05 km/sec.

The accelerating model produces fit indices 10 times smaller than those obtained from the fixed model and better agreement with both the aperture summation Q_{OH} derivation and direct measurements of V_{OH} . A point-by-point least squares fit analysis shows the improvement

in fit is due primarily the quality of the match in the outermost part of the radial profile, which is where the shape is most sensitive to the presence of acceleration in the outer coma. Our best results are for a substantial change in velocity across a relatively small region within $\sim 1-2 \times 10^4$ km of the nucleus, followed by a much shallower gradient at larger distances (Table 3; Figure 3b). These fits consistently indicate an initial velocity ($\sim 1.0 \text{ km-s}^{-1}$) that is quite close to the measured range of less active comets at the same heliocentric distance (Budzien, et al. 1994) and inner coma velocity dispersion measurements (Biver, et al. 1997). Acceleration in the model continues throughout the coma, such that the outflow velocity eventually reaches a larger value ($2.3-2.6 \text{ km-s}^{-1}$) similar to other outer coma measurements (Colom, et al. 1997).

Inverting the model profiles to production rates results in a range of $Q_{\text{H}_2\text{O}} = 0.8-1.0 \times 10^{31} \text{ s}^{-1}$ for both dates, which are much closer to the results of aperture summation. The derived $Q_{\text{H}_2\text{O}}$ for the quadrants is also more uniform with PA in this model output than in the fixed case, which we expect if the H_2O velocity is allowed to change and acceleration can occur beyond the edge of the H_2O scale length.

The model results by quadrant again show that the leading hemisphere is less accelerated than the trailing one, with the most spatially extended sectors being fit by a larger outflow velocity at 10^6 km than those in the leading hemisphere. The largest velocity gradients in the coma average and trailing hemisphere are found inside the collision sphere, although most of the acceleration occurs in the outer coma, where the velocity gradient is significantly smaller, but occurs over a substantially greater distance. On 28 March, the leading sectors of the coma were fit best by an acceleration profile that had no gradient inside the collision zone. Whether this is an artifact of the model or indicative of a physical mechanism such as dust mass loading (Colom, et al. 1997) is not clear from our simple treatment.

6.0 Comparisons of the Model Velocity Distribution with Other Data and Models:

6.1 Radio Outflow Velocity Measurements:

We compared the results of our models with the aperture summed radio measurements of Colom et al., (1997) and Biver et al. (1997) by computing a number density weighted, line-of-sight integrated velocity at each radial distance from the nucleus, weighting them by the area of their ring, and then co-adding all of the rings to obtain an average outflow velocity. The main caveat to this approach is that our simple model produces line of sight velocities assuming pure radial expansion without vectorial or thermal dispersion in the velocity distribution. However, the trapezoid method (Bockelée-Morvan, et al. 1990) used in the reduction of the radial data isolates only the radial velocity component, which is the equivalent of our model velocities. The comparison with the divergent fields of view of the radio measurements serves a check on the

model and the assumed OH quenching characteristics.

6.2.1 Inner Coma Velocities:

Biver et al. (1997) provide velocities over different regions of the inner coma, but they do not specifically measure OH. Indeed they can't, since virtually all of it would be quenched at such small distances from the nucleus (Schloerb 1988; Schloerb et al. 1997). Instead, they use several different species including HCN, CO, H₂S, CH₃OH, CS, and H₂CO to derive the expansion velocity over the 1-5 x 10⁴ km half-power width of their beam. Given the extent of the collision sphere, and clear evidence for acceleration across the inner coma, it is reasonable to assume that the outflow at any given point over this region is the same for all gas species. On the other hand, each constituent of the coma will have different radial characteristics depending on its scale length, whether it is a parent or a daughter species, or whether it has an extended source distribution. A substantial variation in aperture averaged V_{outflow} will be obtained from the different species, with most of the difference due *only* to the spatial distribution of the sources. The extent to which Biver et al. (1997) was able to account for this in their measurements is unclear, but it must have been a significant effect given the spread of scale lengths for the species they measured. For our purposes, we ran a variable velocity simulation for the best fit case of acceleration parameters for the OH radial distribution, using a species with a scale length equal to that of HCN (Huebner, et al. 1992) and assuming a nucleus-centered source. Using figure 2 of Biver et al., we find an HCN outflow velocity of 1.4 ± 0.1 km/s for the period surrounding perihelion. Our model value of $V_{\text{H}_2\text{O}} = 1.2 \pm 0.15$ km/s is within the relative uncertainties of the different results.

6.2.2 Intermediate Distances:

Colom et al. (1997) directly measured the velocity of OH over a much larger area with an asymmetric (3.5' x 19'; 200000 x 110000 km) beam and obtained an average outflow velocity of 2.2 km/s. We are able to compare our model with this result, with the primary caveat that we must also address the effect of quenching in the radio measurements. Schloerb et al. (1997) computed the OH quenching radius (R_Q) for Hale-Bopp to be 5×10^5 . Since only OH molecules at distances $\geq R_Q$ are detectable in radio observations, Colom et al. (1997) therefore measured a velocity average that was strongly biased to the outer coma. This will result in a higher coma averaged velocity in the radio relative to our unquenched model fit, with the size of the difference indicative of the magnitude of the acceleration and the spatial extent over which it occurs in the undetected areas of the coma. For example, a collision zone confined to the immediate vicinity of the nucleus will result in only a minimal difference between a quenched velocity and an unquenched one. Thus, the difference in our modeled area averaged outflow of

1.7 km/s when compared to their radio measurement of 2.2 km/s implies a broad acceleration region in Hale-Bopp. We can carry the comparison further by incorporating quenching effects in our model such that we restrict the contributing OH emission to a shell surrounding the nucleus with an inner radius equal to R_Q . Averaging only the velocities in this extended region of the coma results in a simulated average velocity of 2.3 km-s^{-1} , which is closer still to the measured value of Colom et. al. (1997).

6.3 Comparison with Observational and Theoretical Predictions:

Very little data exists on the characteristics of comets with $Q_{\text{H}_2\text{O}} \sim 10^{31} \text{ s}^{-1}$, and most of the predictions are merely an extension of the behavior of weaker comets to this scale. In this sense Hale-Bopp is in a class of its own with respect to coma dynamics and provides the best opportunity to date to test the accuracy of these predictions. When $Q_{\text{H}_2\text{O}} > 10^{31} \text{ s}^{-1}$, the collision sphere radius exceeds the scale length of water at 1 AU, opacity effects become significant, and other processes, such as parent/daughter/granddaughter collisions, chemistry (e.g. Komitov, 1989) and ion-neutral interactions, may begin to emerge. Bockelée-Morvan et al. (1990) have compiled the most extensive listing of $Q_{\text{H}_2\text{O}}$ vs. $V_{\text{H}_2\text{O}}$ in active ($Q_{\text{H}_2\text{O}} > 10^{29} \text{ s}^{-1}$) comets, and their data shows clear evidence of an upturn in the outflow velocity for active comets. Hale-Bopp is a clear validation that this trend continues with increasing activity, though perhaps not to the extent implied by those weaker comets. Cochran and Schleicher (1993) took the Bockelée-Morvan results a step further by fitting them to a power law modification of the standard Q-V relationship

$$5) \quad V_{\text{OH}} = 0.85 r_h^{-2} \times (Q/10^{30})^{0.5},$$

which, as no more than a fit to points on a graph, is a somewhat ad hoc result. From their equation we can obtain a value of $V_{\text{H}_2\text{O}} \sim 3.25 \text{ km-s}^{-1}$ for a comet with $Q_{\text{H}_2\text{O}} = 10^{31} \text{ s}^{-1}$ and $R_h = 0.91 \text{ AU}$. This is substantially higher than we obtain from the variable velocity model and was observed aperture average velocity (Colom, et al. 1997).

Physical models of collisionally dense comas that include extensive regions of dust/gas interactions and substantial opacity corrections (Combi, et al. 1997; Crifo 1995) may also be extended to the necessary activity scale. We compare our data and simulation results with those of Combi et al. (1997), who used a 1-D spherical hybrid kinetic/dusty gas-hydrodynamic calculation to describe the thermal and velocity characteristics of the outflow with cometocentric distance from the nucleus for Hale-Bopp at different heliocentric distances. The results of our simulations generally agree with the dusty gas predictions, although we expect as much in the case of the variable velocity case, since it was based on the parameters of the Combi et al. (1997) model. However it is also true of the fixed model, where the best fits were for cases with large

differences between the initial and final velocities of the bulk flow, with the average velocity increasing rapidly near the nucleus and more slowly in the outer coma. The notable exceptions to this are the sectors with spatially extended OH emission, which are fit on every spatial scale by significantly *higher* acceleration than the Combi et al. (1997) model indicates at 1 AU.

7.0 Potential Sources of the Extended Emissions:

The OH enhancement in the sector between the anti-Sun and orbit-trailing directions could have one source or several mechanisms acting together to produce it. Some of these are unlikely or can be easily shown to be inadequate. For example, the magnitude of radiation pressure on OH is only enough to accelerate the gas by ~ 0.01 km/s over our field of view. We looked closely at four mechanisms that could produce an apparent enhancement including dust contamination from the tail, distributed gas production from icy grains, dust mass loading in the leading hemisphere, and an ion-neutral interaction.

7.1 Dust Contamination:

While OH emission dominates over continuum in the regions near the nucleus, dust contamination may be significant in the outer parts of the coma where the OH brightness is lower. If improperly accounted for, the dust scattering of solar continuum could produce a false region of enhancement. This effect is most important where the dust is concentrated along the tail and extending back toward the antisunward vector, which is also where the extended OH emission regions are observed. To check this, we made a direct comparison of the radial shape and brightness of the dust over the same angular regions from a visible continuum image obtained on the same night as the April 08 OH data. The image was taken using the Blue Continuum ($4446 \pm 31 \text{ \AA}$) filter of the Hale-Bopp filter library, covering the same field of view. After correcting for instrument sensitivity, atmospheric attenuation, and the brightness of the solar flux at 3100 \AA vs 4450 \AA , a radial dust profile was extracted over the sub-sector corresponding to the greatest radial enhancement of OH. In direct comparison (figure 6), the dust and OH radial distributions differ on two levels that allow us to eliminate dust as the source of the trailing extension. The shape of the dust profile is significantly shallower with radial distance than OH, while its brightness is only $\sim 2\text{-}10\%$ that of OH, out to distances $>10^6$ km.

7.2 Grain Evaporation:

While we can demonstrate that scattered solar continuum from dust does not contribute significantly to the OH radial distribution, the dust lane does cover the area of the enhancement and could thus still affect the OH radial distribution through outgassing from grains in the tail. We cannot possibly to completely exclude this process as a contributor; however it would have

several effects on coma structure that make it an unlikely source of the increased spatial extent of OH. The distribution of evaporative grains would need to be approximately uniform throughout the tail sectors to produce the smooth radial shape seen in the OH data. The source of evaporating grains would have to have been continuous over a period of more than a month to account for the persistence of the feature in OH and O (1D) images (Morgenthaler, et al. in press). Finally, any OH produced beyond 2×10^5 km would be in the ballistic coma, and thus not accelerated beyond the convolution of grain motion and the 1.05 km/s excess formation velocity. Because the distribution of OH is dominated by the extended sectors beyond 5×10^5 km, such a velocity admixture would be reflected in the aperture summation measurements of Colom et al. (1997) as an average velocity reduction that is not observed.

7.3 Dust Mass Loading:

Several studies of the Hale-Bopp coma have concluded that dust grain production was largely confined to the sunlit hemisphere of the nucleus (Rauer et al. 1997; Weaver et al. 1997), while gas production was more uniformly distributed (Samarasinha, Mueller, & Belton 1997). In the inner coma, where photolytic heating is most effective in accelerating the neutrals, the local dust grain population absorbs collisional energy, thus impeding the acceleration and gas heating. The spatial extent and efficiency of the dust loading process in Hale-Bopp was examined by Combi et al. (1997), who looked at the effect on outflow for different cases of an active sector on the nucleus with various dust grain-size distributions. While the magnitude of the interaction is highly dependent on unknown elements of the dust grain-size, their models did show significant mass loading retardation of the flow in the dusty areas. This could explain certain aspects of the spatial structure seen in OH, particularly the fact that the sunward quadrant was consistently less extended than the others. However, the magnitude of the effect in the Combi et al. model is significantly less than is observed between the leading and trailing hemispheres in OH. Moreover, this process fails to predict a focused acceleration in the dust free zone, but rather a focused deceleration in the sunward direction.

7.4 Ion-Neutral Coupling:

Photo-ionization and solar wind mass loading provide a considerable source of energy input to the trailing hemisphere of the coma that could be tapped to produce a vectored acceleration in the neutral component in a manner similar to that observed in planetary ionospheres. Newly formed ions in the inner coma are picked up by the magnetized solar wind and accelerated toward the solar wind flow direction, away from the component of the comet orbital velocity that is perpendicular to the comet-Sun line. The magnitude of the solar wind-derived acceleration will depend on the density, velocity, and field strength in the local wind,

while the orbital component will increase as the comet approaches the Sun, reaching a maximum at perihelion when the motion of the comet is greatest and directed exactly perpendicular to the comet-Sun line. The accelerating ions will mass load the solar wind, but may also in turn be mass loaded by interactions with inner coma neutrals. The strength of such an ion-neutral coupling would depend on several factors including the density of the neutral coma, which is driven by $Q_{\text{H}_2\text{O}}$, the ion velocity, and the different charged particle scattering cross sections of the molecular species. Detailed modeling of the ion-neutral interaction will be needed to sort out the effect, if any, of this mechanism on neutral outflow.

The possibility of an ion-neutral interaction is supported by the large gas production rate of Hale-Bopp and by observations of the inner coma ion distribution that suggest the presence of substantial mass loading of comet ions (Anderson 1997). These data show smooth acceleration of H_2O^+ at 0.161 m s^{-2} on March 16, 1997 and 0.197 m s^{-2} on April 21, 1997 out to $> 2 \times 10^6 \text{ km}$ from the nucleus. This acceleration is 3-10x smaller than was derived for Halley in 1986 (Scherb et al., 1990). Anderson (1997) attributes this retardation to solar wind mass loading by the substantial population of comet ions. Without direct measurements of the solar wind itself, it is not possible to distinguish between coupling to the solar wind and interaction with coma neutrals; both will produce the same effect.

8.0 Summary:

We have derived $Q_{\text{H}_2\text{O}}$ from wide FOV images of OH emission from Hale-Bopp using aperture summation and $V_{\text{OH}}(r)$ from fixed and variable velocity spherical expansion models that assume an unresolved H_2O source region. The resulting integrated OH brightness and $Q_{\text{H}_2\text{O}}$ are consistent with other observations taken near perihelion, while model fits to the radial distribution of OH show a significant enhancement in the cometocentric extent of the emission relative to weaker comets. The fixed model results show conclusively that acceleration occurred over a substantial region of the coma; however, our best results are obtained with the more physically realistic variable velocity simulation, which indicates changing acceleration with cometocentric distance characterized by a steep velocity gradient inside a collision zone and a broad region of acceleration over the rest of the coma. These results confirm the extrapolated predictions of coma structure for very active comets that are based on a combination of models (Combi & Smyth 1988b) and observations (Bockelée-Morvan, et al. 1990; Schleicher, et al. 1998). When compared to published radio measurements of V_{OH} and $Q_{\text{H}_2\text{O}}$ (Biver, et al. 1997; Colom, et al. 1997), our models match coma averages over fields of 10^4 km and $2 \times 10^5 \text{ km}$.

When the coma is broken down into quadrants, a significant asymmetry in the OH radial distribution emerges in the shape of the profiles on all scales within the coma. The OH brightness distributions in the trailing hemisphere are generally shallow compared to the leading

hemisphere in the inner coma, but cross over at intermediate distances to become brighter and more spatially extended. This behavior was a common characteristic of each observation and is similar to an azimuthal asymmetry observed in O(¹D) by Morgenthaler, et al. (in press). Detailed study of the spatial extension shows it to be primarily focused into a 60° range of PA between the dust tail and the anti-sunward direction. Model fits for these regions suggest that greater acceleration occurred in these regions than elsewhere in the coma. We discuss several possible sources for the enhancement including a wider trailing hemispheric collision region, icy grain outgassing in the dust tail, reduced dust mass loading in the trailing hemisphere, and a vectored ion-neutral interaction with the solar wind and comet ions. Additional modeling is required to distinguish among those processes that cannot be discounted as a contributing factor.

References:

- Anderson, C. M. 1997, *Earth Moon and Planets*, 78, 99
- Biver, N., et al. 1997, *Earth Moon and Planets*, 78, 5
- Bockelée-Morvan, D., Crovisier, J., & Gerard, E. 1990, *Astronomy and Astrophysics*, 238, 382
- Budzien, S. A., Festou, M. C., & Feldman, P. D. 1994, *Icarus*, 107, 164
- Cochran, A. L., & Schleicher, D. G. 1993, *Icarus*, 105, 235
- Colom, P., Gerard, E., Crovisier, J., Bockelée-Morvan, D., Biver, N., & Rauer, H. 1997, *Earth Moon and Planets*, 78, 37
- Combi, M. R., Kabin, K., DeZeeuw, D. L., Gombosi, T. I., & Powell, K. G. 1997, *Earth Moon and Planets*, 79, 275
- Combi, M. R., Reinard, A. A., Bertaux, J.-L., Quemerais, E., & Mäkinen, T. 2000, *Icarus*, 144, 191
- Combi, M. R., & Smyth, W. H. 1988a, *Astrophysical Journal*, 327, 1044
- . 1988b, *Astrophysical Journal*, 327, 1026
- Crifo, J. F. 1995, *Astrophysical Journal*, 445, 470
- Dello Russo, N., Mumma, M. J., DiSanti, M. A., Magee-Sauer, K., Novak, R., & Rettig, T. W. 2000, *Icarus*, 143, 324
- Farnham, T. L., Schleicher, D. G., & A'Hearn, M. F. 2000, *Icarus*, 147, 180
- Festou, M. C. 1981a, *Astronomy and Astrophysics*, 95, 69
- Haser, L. 1957, *Bulletin de la Societe Royale des Sciences de Liege*, 43, 740
- Hodges, R. R. 1990, *Icarus*, 83, 410
- Hu, H.-Y. 1990, Ph.D. Dissertation, University of Arizona
- Huebner, W. F., Keady, J. J., & Lyon, S. P. 1992, *Astrophysics and Space Science*, 195, 7
- Krishna Swamy, K. S. 1997, *Physics of comets*
- Lammerzahl, P., et al. 1987, *Astronomy and Astrophysics*, 187, 169
- Morgenthaler, J. P., et al. in press, in *Astrophysical Journal*
- Rauer, H., et al. 1997, *Science*, 275, 1909
- Samarasinha, N. H., Mueller, B. E. A., & Belton, M. J. S. 1997, *Earth Moon and Planets*, 77, 189
- Schleicher, D. G., & A'Hearn, M. F. 1988, *Astrophysical Journal*, 331, 1058
- Schleicher, D. G., Millis, R. L., & Birch, P. V. 1998, *Icarus*, 132, 397
- Schloerb, F. P. 1988, *Astrophysical Journal*, 332, 524
- Schloerb, F. P., Devries, C. H., Lovell, A. J., Irvine, W. M., Senay, M., & Wootten, H. A. 1997, *Earth Moon and Planets*, 78, 45
- Schultz, D., Li, G. S. H., Scherb, F., & Roesler, F. L. 1993, *Icarus*, 101, 95
- Smyth, W. H., Marconi, M. L., Scherb, F., & Roesler, F. L. 1993, *Astrophysical Journal*, 413, 756
- Van Dishoeck, E. F., & Dalgarno, A. 1984, in *Icarus*, 305
- Weaver, H. A., et al. 1997, *Science*, 275, 1900
- Whipple, F. L., & Huebner, W. F. 1976, *Annual Review of Astronomy and Astrophysics*, 14, 143
- Woods, T. N., Feldman, P. D., & Rottman, G. J. 2000, *Icarus*, 144, 182

Figure Captions

Figure 1. The spherically averaged radial surface brightness distribution of OH on 08 April, 1997 is compared with the best fit of a model for a uniform 0.89 km-s^{-1} outflow derived from the velocity-heliocentric distance relationship of Budzien et al., 1994. The model fits the profile out to a radial distance of $2 \times 10^5 \text{ km}$, but begins to fall below the data beyond this point, due to collisional acceleration in the inner coma. Production rate estimates based on this fit yield $Q_{\text{H}_2\text{O}} = 6 \times 10^{30} \text{ s}^{-1}$, which is $\sim 30\%$ less than those obtained from other methods (e.g. Combi et al., 2000, Colom et al., 1997).

Figure 2. Quadrant profiles are compared for each of the two nights. In A) and B) the four 90° sectors covering the anti-sun, sunward, anti-tail, and tailward directions are compared directly. While significant differences in the degree of symmetry in the coma is obvious between the nights, there is a general trend of the anti-sun and anti-tail profiles being shallow compared with the others inside of 10^5 km and then crossing over to become more extended beyond this point. In C) and D), the most radially extended quadrants of the coma are broken down into 30° sub-sectors of position angle and then compared with the anti-tailward sector. Each sub-sector is considerably more radially extended than the sunward profile, and are also responsible for most of the enhancement in the spherically averaged profile.

Figure 3. Sample model fits are shown for the spherically averaged OH radial distribution on 08 April, 1997 using the fixed velocity (a) and variable velocity (b) models. The parameters of the model outputs are shown in each case. Both models indicate the presence of acceleration over much of the coma, with the variable case providing a much closer match to $Q_{\text{H}_2\text{O}}$ and $V_{\text{OH}}(r)$ values obtained from other measurements.

Figure 4. The statistics of fit index vs. two tests of convergence for all cases in the fixed velocity model. In a), the product of the OH and H_2O velocities are shown. The convergence onto a narrow range in the cases of close fits is consistent with the two velocities tracking each other inversely in the model. In b) the ratio of the velocities reveals the degree of acceleration in the inner coma. The minimum of the distribution changes between the quadrants with the largest values occurring for the radially extended sectors. Also evident here is the overall low quality of uniform, or close to uniform, single velocity outflow, which is a value of 1 here. The fit indices for this case are ~ 2 orders of magnitude larger.

Figure 5. The radial profile of the most extended sub-sector of the OH coma is compared here with the scaled residual dust continuum in the same sector. As can be seen here the contribution of the dust to the radial shape observed in the OH is not large enough to significantly affect the basic characteristic of the extension relative to the other sectors.

Tables:

Table 1. OH Observations of Hale-Bopp at the Burrell Schmidt.

Obs. Date/Time	r^1	Δ^2	PA_R^3	PA_V^4	FOV (km)	Airmass	$Q_{H_2O}(10^{30} s^{-1})^5$
03/28/97 02:31:58	0.917	1.327	15.6	285	4.646×10^6	2.98-3.22	9.31 ± 1.4
04/08/97 02:52:14	0.920	1.418	39.8	308	4.965×10^6	2.55-2.74	10.8 ± 1.6

¹ Heliocentric distance in AU.

² Geocentric distance in AU.

³ Position Angle of the Sun-Comet extended radius vector.

⁴ Position Angle of the Comet Velocity Vector.

⁵ Production rate derived from aperture summation.

Table 2. The Orbit and Solar Cycle specific photochemical parameters of OH production and fluorescence at 1 AU.

Physical Parameters of H ₂ O Photochemistry and OH Fluorescence	
H ₂ O Dissociation Branching Ratio	86% ⁽¹⁾
Dissociation Rate of H ₂ O	$1.043 \times 10^{-5} s^{-1}$ ⁽²⁾
Dissociation Rate of OH	$7.491 \times 10^{-6} s^{-1}$ ⁽²⁾
OH Fluorescence g-factor	$4.54 \times 10^{-5} s^{-1}$ ⁽³⁾

⁽¹⁾ Huebner, Keady, and Lyon, 1992

⁽²⁾ Schleicher and A'Hearn, 1988

⁽³⁾ Budzien et al., 1994

Table 3. At top the results of the fixed velocity simulation fits are shown as a coma average and by quadrant for both nights.

Fixed Velocity Model:						
Obs. Date	PA	$V_{\text{H}_2\text{O}}$	V_{OH}	$Q^{31}\text{H}_2\text{O} (\times 10^{31} \text{ s}^{-1})$	Sector	
03/28/97	0-360°	0.52 (± 0.07)	3.25 (± 0.30)	1.44 (± 0.09)	Average	
	210-	0.56 (± 0.12)	2.35 (± 0.35)	1.30 (± 0.10)	Anti-Tail	
	120-	0.60 (± 0.16)	2.35 (± 0.35)	1.40 (± 0.09)	Sunward	
	30-120°	0.60 (± 0.08)	4.65 (± 0.55)	1.72 (± 0.11)	Tailward	
	300-30°	0.48 (± 0.04)	3.80 (± 0.50)	1.31 (± 0.12)	Anti-Sun	
04/08/97	0-360°	0.53 (± 0.07)	3.20 (± 0.30)	1.30 (± 0.05)	Coma Average	
	270-0°	0.56 (± 0.04)	2.65 (± 0.25)	1.19 (± 0.05)	Anti-Tail	
	180-	0.44 (± 0.16)	2.60 (± 0.50)	1.09 (± 0.10)	Sunward	
	90-180°	0.52 (± 0.08)	2.95 (± 0.35)	1.28 (± 0.06)	Tailward	
	0-90°	0.68 (± 0.08)	4.00 (± 0.30)	1.51 (± 0.06)	Anti-Sun	
Variable Velocity Model:						
03/28/97						
Sector	V_{O}	V_{C}	V_{E}	$dV_{\text{C}} (10^5 \text{ s}^{-1})$	$dV_{\text{F}} (10^5 \text{ s}^{-1})$	$Q_{\text{H}_2\text{O}}$
0-360°	0.94 \pm 0.26	1.07 \pm 0.07	2.64 \pm 0.02	1.25 \pm 1.25	0.20 \pm 0.01	9.70 \pm 0.55
30-120°	0.88 \pm 0.10	0.88 \pm 0.10	1.78 \pm 0.25	0.0	0.15 \pm 0.06	8.95 \pm 1.10
120-210°	0.94 \pm 0.10	0.94 \pm 0.10	1.74 \pm 0.25	0.0	0.14 \pm 0.05	9.80 \pm 0.77
210-300°	1.05 \pm 0.30	1.36 \pm 0.15	2.10 \pm 0.20	3.1 \pm 2.0	0.11 \pm 0.04	11.5 \pm 1.1
300-30°	1.02 \pm 0.33	1.21 \pm 0.13	2.22 \pm 0.32	1.9 \pm 1.5	0.14 \pm 0.07	8.85 \pm 0.55
04/08/97						
0-360°	0.94 \pm 0.10	1.14 \pm 0.22	2.52 \pm 0.25	2.0 \pm 1.8	0.24 \pm 0.07	9.30 \pm 0.60
0-90°	0.90 \pm 0.10	1.04 \pm 0.10	2.24 \pm 0.50	1.4 \pm 1.3	0.21 \pm 0.10	9.13 \pm 0.31
90-180°	0.88 \pm 0.17	0.94 \pm 0.12	2.50 \pm 0.50	0.6 \pm 0.5	0.27 \pm 0.08	8.70 \pm 0.59
180-270°	1.02 \pm 0.30	1.16 \pm 0.16	2.65 \pm 0.35	1.2 \pm 1.0	0.23 \pm 0.08	10.1 \pm 0.9
270-360°	1.05 \pm 0.35	1.43 \pm 0.20	2.70 \pm 0.24	3.8 \pm 3.0	0.19 \pm 0.05	11.1 \pm 1.0

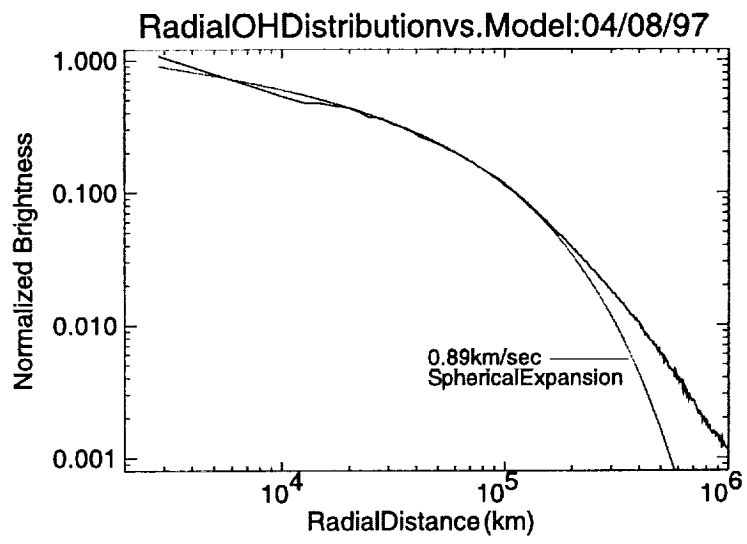


Figure 1

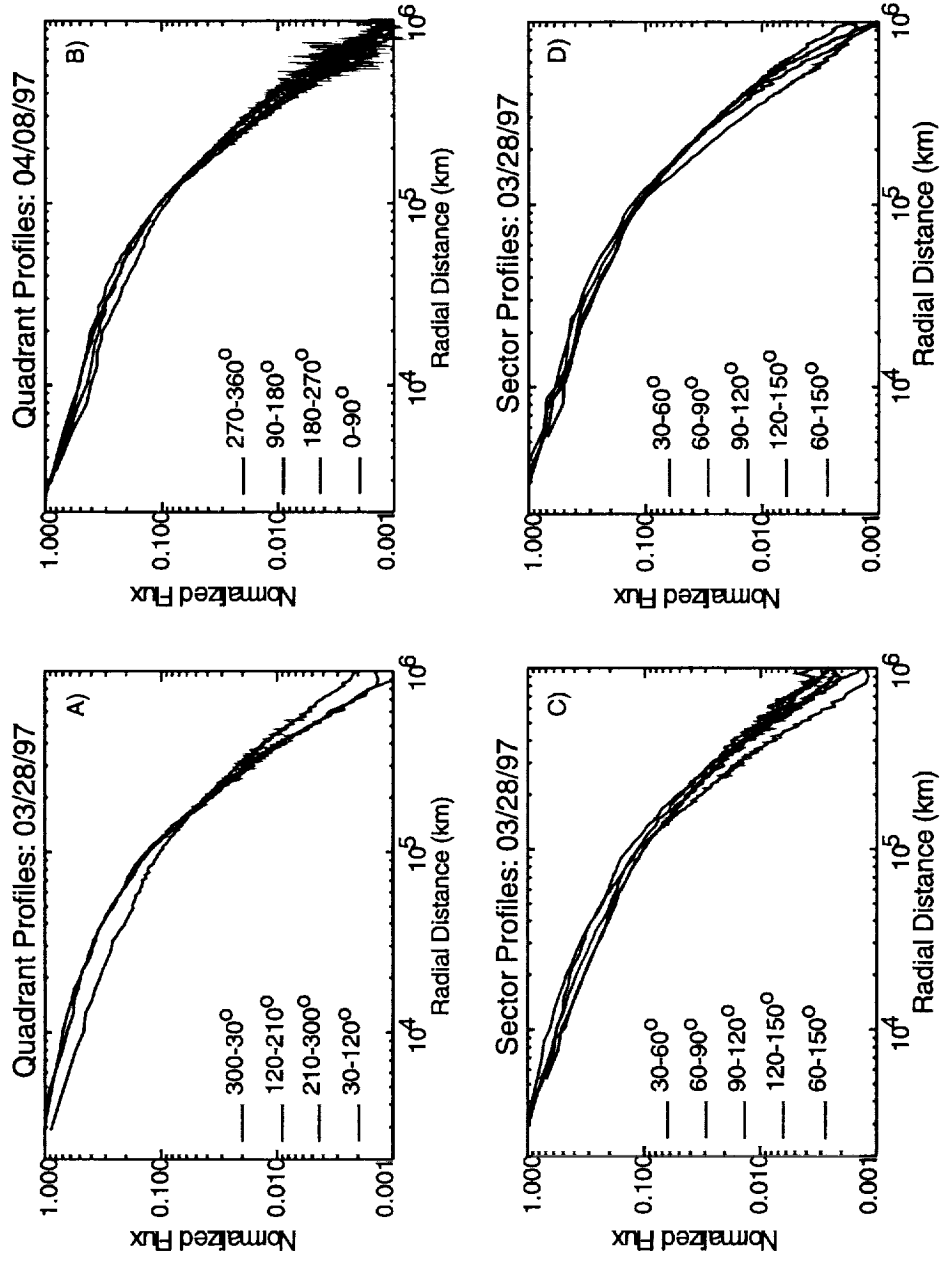


Figure 2

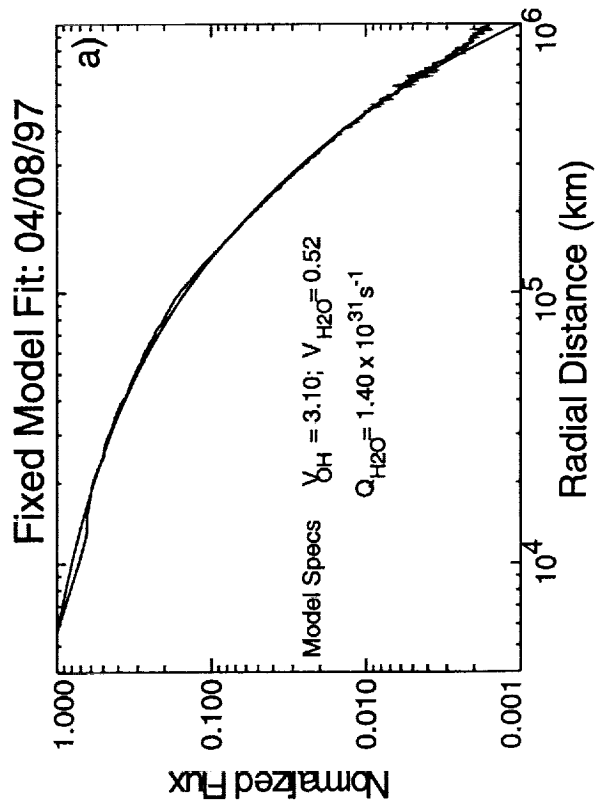
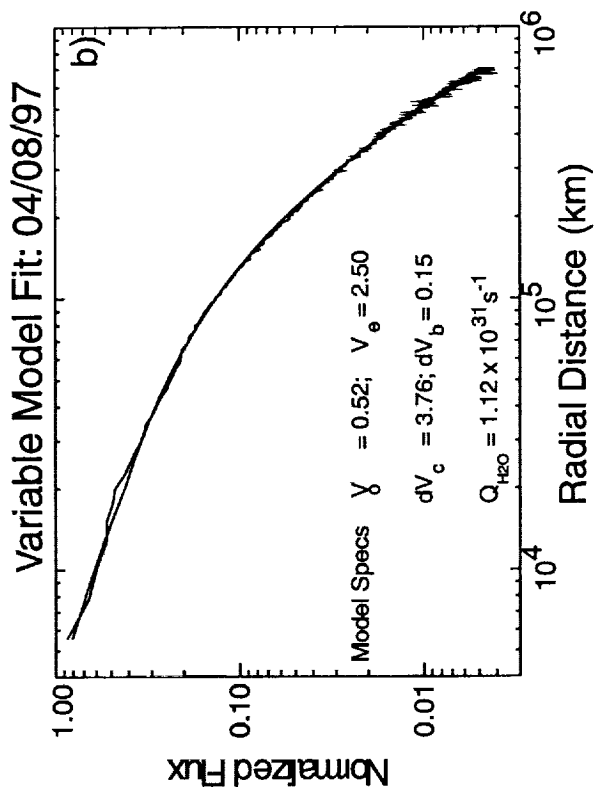


Figure 3

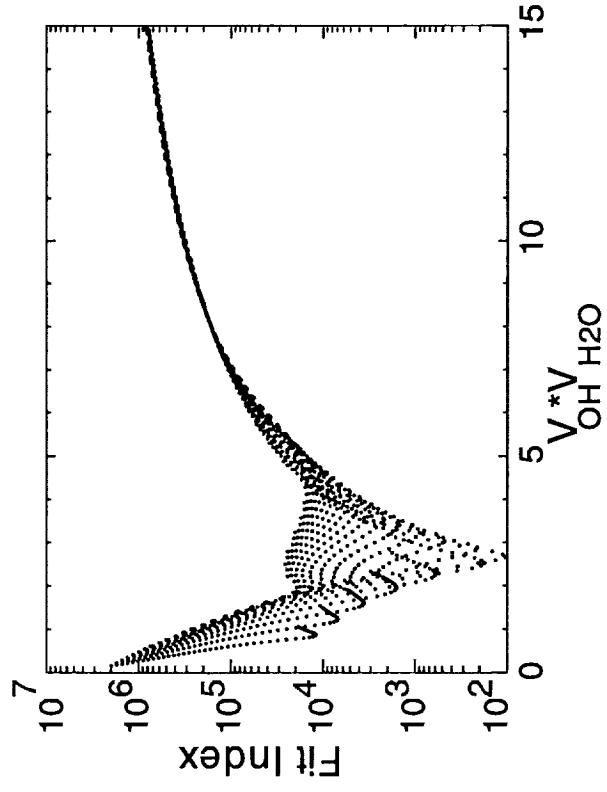
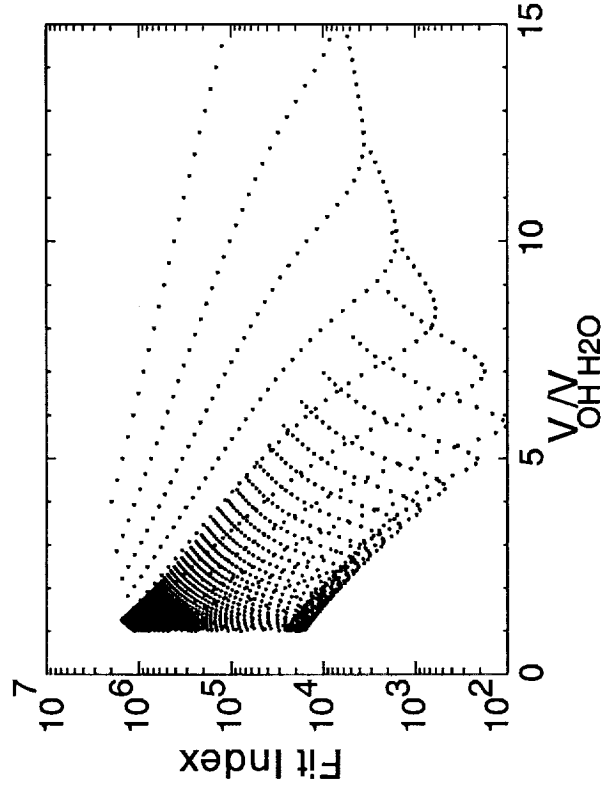


Figure 4

OHRadialProfile vs.ContinuumContribution

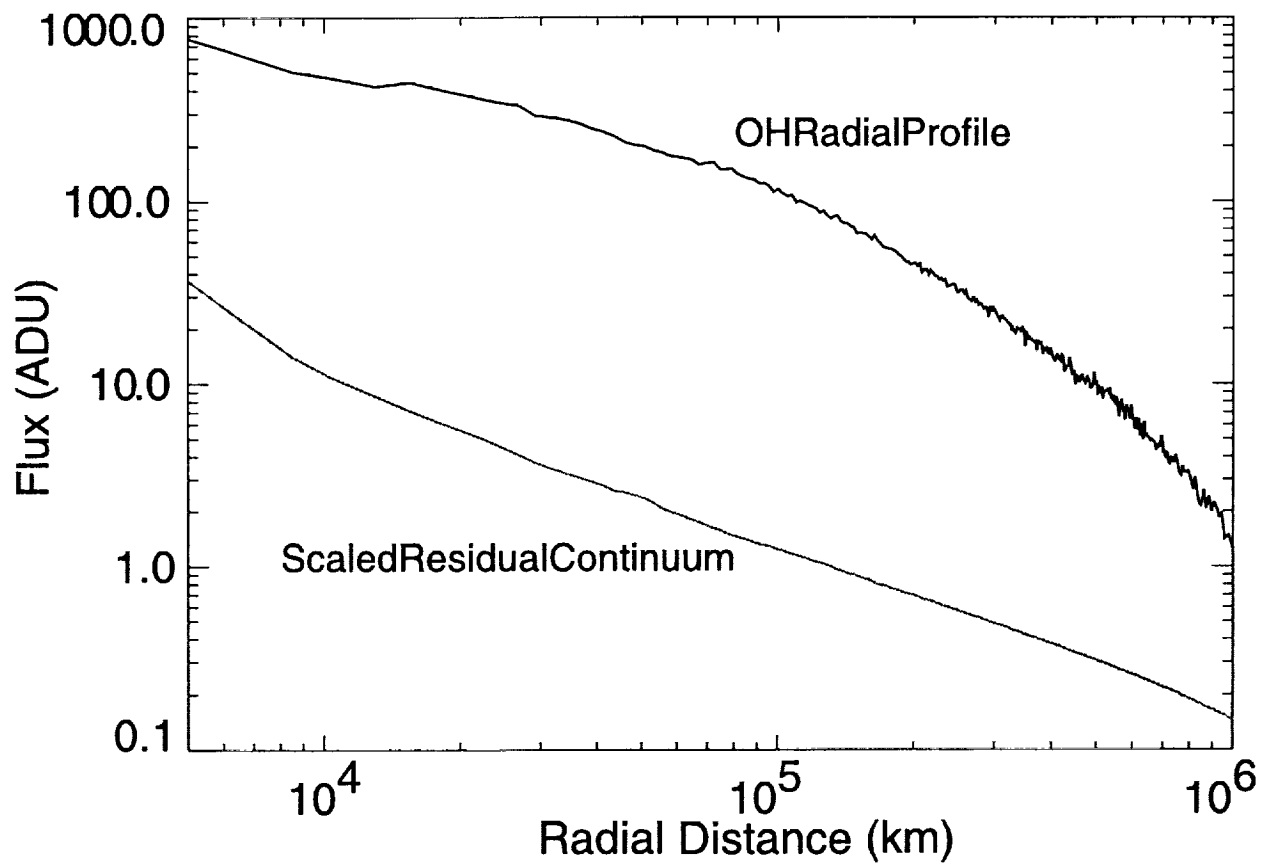


Figure 5